UNIVERSITY OF ROCHESTER
LABORATORY FOR LASER ENERGETICS

Volume 154
January–March 2018
DOE/NA/1944-1397

LLE Review

Quarterly Report

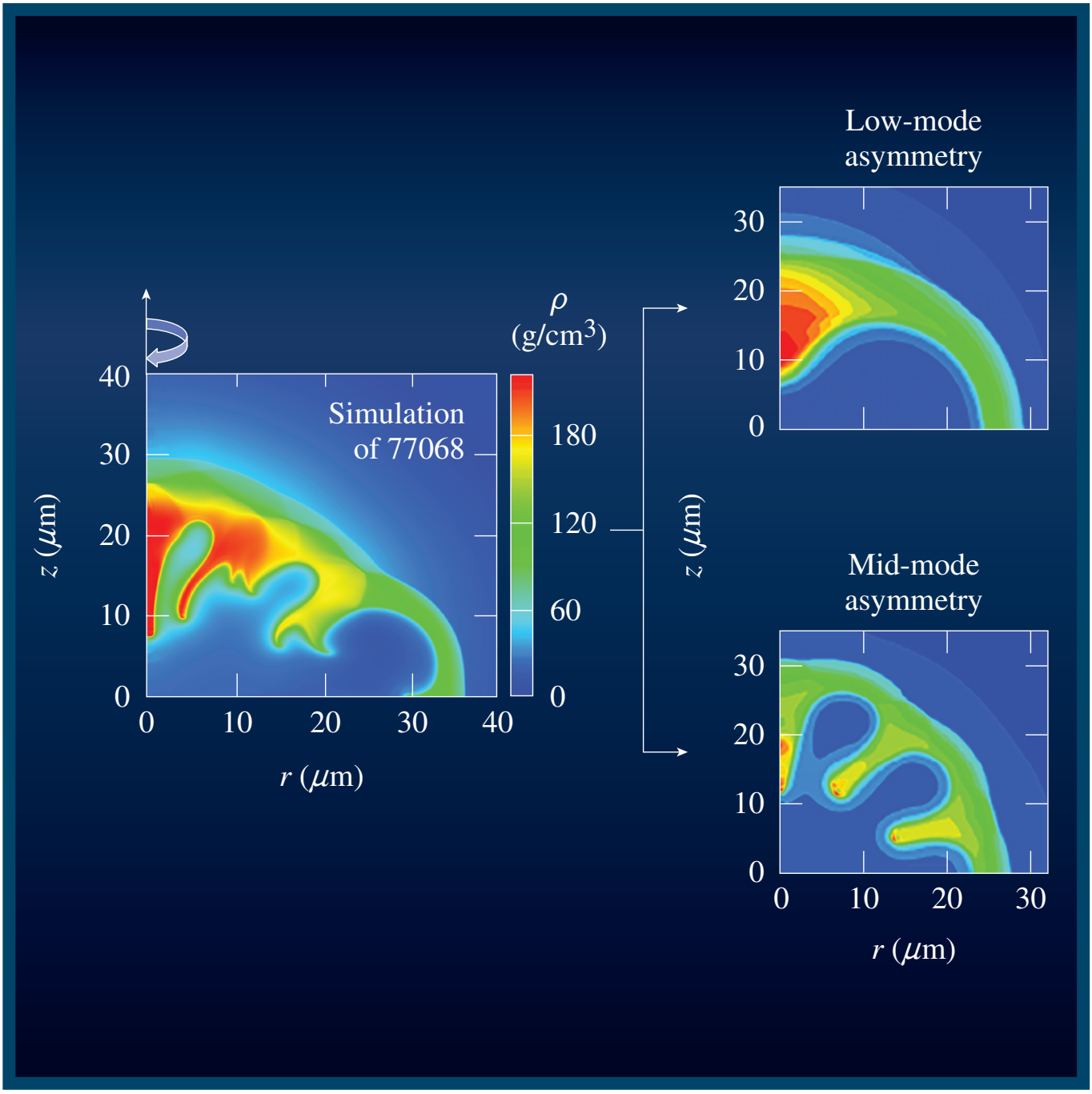

About the Cover:

The figure on the front cover illustrates that a combination of low- ($\ell < 6$) and mid-mode ($6 < \ell < 40$) asymmetries is necessary to reproduce and explain the experimental observables of high-convergence cryogenic implosions on OMEGA. The reconstructed simulation of high-performing shot 77068 is shown. It is expected that mid-mode asymmetries, such as $\ell = 10$, can be introduced by the overlapped intensity variation arising from the superposition of all 60 laser beams on OMEGA. A multi-objective analysis technique has been developed for investigating such systematic degradation mechanisms of an imploding core. This technique was applied to an ensemble of cryogenic DT implosions that generated hot-spot pressures of ~50 Gbar, which showed that a systematic and repeatable combination of modes is responsible for the observed performance degradation. This concept-driven, multi-objective technique for analyzing data from cryogenic DT implosions on OMEGA takes into account the trends in all the experimental observables, thereby providing a technique for investigating the cause of the performance degradation and systematic errors in the measurement.

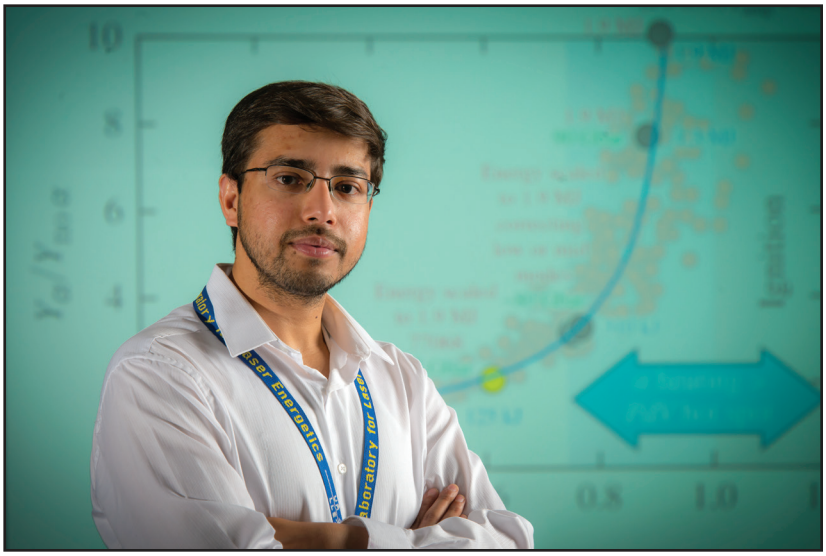

In the photo on the right, student A. Bose is shown with a plot depicting the current standing and future potential of the 100-Gbar Direct-Drive Campaign on OMEGA. This plot illustrates the advantage of the direct-drive approach in producing high fusion yields compared to indirect drive with same laser energy. The downside of this approach is the anticipated drive asymmetries—mid and high modes—that have been analyzed in the context of the experimental results.

The work described in this volume includes current research at the Laboratory for Laser Energetics, which is supported by New York State Energy Research and Development Authority, the University of Rochester, the U.S. Department of Energy Office of Inertial Confinement Fusion under Cooperative Agreement No. DE-NA0001944, and other agencies.

For questions or comments, contact Sid Sampat, Editor, Laboratory for Laser Energetics, 250 East River Road, Rochester, NY 14623-1299, (585) 275-2596.

Worldwide-Web Home Page: http://www.lle.rochester.edu/

Printed in the United States of America
Available from
National Technical Information Services
U.S. Department of Commerce
5285 Port Royal Road
Springfield, VA 22161
www.ntis.gov

UNIVERSITY OF ROCHESTER
LABORATORY FOR LASER ENERGETICS

Volume 154
January–March 2018
DOE/NA/1944-1397

LLE Review

Quarterly Report

UR LLE

Contents

In Brief

This volume of the LLE review covering January–March 2018, features "Analysis of Trends in Implosion Observables and Reconstruction of the Implosion Dynamics for Direct-Drive Cryogenic Targets on OMEGA" by A. Bose, R. Betti, D. Mangino, D. Patel, K. M. Woo, A. Christopherson, V. Gopalaswamy, S. P. Regan, V. N. Goncharov, C. J. Forrest, V. Yu Glebov, J. P. Knauer, F. J. Marshall, R. C. Shah, C. Stoeckl, W. Theobald, T. C. Sangster, and E. M. Campbell (LLE) and J. A. Frenje and M. Gatu Johnson (MIT). This article (p. 59) describes a technique to identify trends in performance degradation for inertial confinement fusion implosion experiments based on reconstruction of the implosion core with a combination of low- and mid-mode asymmetries. This was applied to the ensemble of hydro-equivalent deuterium–tritium implosions on OMEGA that achieved hot-spot pressures $\approx 56 \pm 7$ Gbar when hydrodynamically scaled to the energy of the National Ignition Facility.

Additional research highlights presented in the issue include the following:

- D. Turnbull, P. Franke, J. Katz, J. P. Palastro, I. A. Begishev, R. Boni, J. Bromage, A. L. Milder, J. L. Shaw, and D. H. Froula have demonstrated the successful use of the flying focus technique that uses a chirped laser beam focused by a highly chromatic lens to produce an extended focal region within which the laser intensity can propagate at any velocity (p. 75). When that intensity is high enough to ionize a background gas, an ionization wave will track the intensity isosurface corresponding to the ionization threshold. We report on the demonstration of such ionization waves of arbitrary velocity. Subluminal and superluminal ionization fronts were produced that propagated both forward and backward relative to the ionizing laser. All backward and all superluminal cases mitigated the issue of ionization-induced refraction that typically inhibits the formation of long, contiguous plasma channels.

- W. Theobald, C. Sorce, M. Bedzyk, S. T. Ivancic, F. J. Marshall, C. Stoeckl, R. C. Shah, M. Lawrie, S. P. Regan, T. C. Sangster, and E. M. Campbell (LLE); T. Hilsabeck, K. Engelhorn, J. D. Kilkenny, and D. Morris (General Atomics); M. Chung (TCM2 Innovations); J. D. Hares and A. K. L. Dymoke-Bradshaw (Kentech Instruments); P. Bell, J. Celeste, A. Carpenter, M. Dayton, D. K. Bradley, M. C. Jackson, L. Pickworth, and S. Nagel (LLNL); and G. Rochau, J. Porter, M. Sanchez, L. Claus, G. Robertson, and Q. Looker (SNL) present the single-line-of-sight, time-resolved x-ray imager (SLOS-TRXI) on OMEGA as one of a new generation of fast-gated x-ray cameras comprising an electron pulse-dilation imager and a nanosecond-gated, burst-mode, hybrid complementary metal-oxide semiconductor sensor (p. 80). SLOS-TRXI images the core of imploded cryogenic deuterium–tritium shells in inertial confinement fusion experiments in the ~4- to 9-keV photon energy range with a pinhole imager onto a photocathode. The diagnostic is mounted on a fixed port almost perpendicular to a 16-channel, framing-camera–based, time-resolved Kirkpatrick–Baez microscope, providing a second time-gated line of sight for hot-spot imaging on OMEGA. SLOS-TRXI achieves ~40-ps temporal resolution and ~10-mm spatial resolution. Shots with neutron yields of up to 1×10^{14} were taken without any hint of a neutron-induced background signal. The implosion images from SLOS-TRXI show the evolution of the stagnating core.

- A. M. Hansen, D. Haberberger, J. Katz, R. K. Follett, D. H. Froula discuss the activation of a supersonic gas-jet target platform on the OMEGA laser (p. 86). An analytic model for gas dynamics in a supersonic nozzle was used to predict gas plume parameters and to design nozzles for use in laser-plasma experiments. The gas-jet system was analyzed with a Mach–Zehnder interferometer to study neutral density and with Thomson scattering to study plasma parameters on the OMEGA Laser System. Initial measurements demonstrate the capabilities of the OMEGA gas jet as a platform for future laser–plasma interaction science.

- J. R. Davies, R. E. Bahr, D. H. Barnak, R. Betti, M. J. Bonino, E. M. Campbell, E. C. Hansen, D. R. Harding, J. L. Peebles, A. B. Sefkow, and W. Seka (LLE); P.-Y. Chang (National Cheng Kung University, Taiwan); and M. Geissel and A. J. Harvey-Thompson (SNL) discuss the study of scaling using laser-driven magnetized liner inertial fusion (MagLIF) on OMEGA (p. 91). It is proposed that full laser energy transmission is achieved by relativistic self-focusing, enhanced by focusing related to the electron density profile that forms, followed by a ponderomotive blowout of the plasma.

- A. Howard, D. Haberberger, R. Boni, R. Brown, and D. H. Froula present the use of a Wollaston interferometer for measuring the density of plasma plumes created in experiments on the OMEGA EP Laser System (p. 107). The diagnostic is installed as an additional arm on the 4ω probe system, a suite of diagnostics that share a 10-ps pulse of 263-nm laser light captured by an imaging system at *f*/4. The interferometer utilizes a Wollaston prism to create two angularly separated beams from a single input probe beam. The unique advantages of this system over standard interferometric means are discussed.

- C. Stoeckl, T. Filkins, R. Jungquist, C. Mileham, S. P. Regan, M. J. Shoup III, and W. Theobald (LLE) and N. R. Pereira (Ecopulse Inc.) show that x-ray imaging using shaped crystals in Bragg reflection is a powerful technique used in high-energy-density physics experiments (p. 113). The characterization of these crystal assemblies with conventional x-ray sources is very difficult because of the required angular resolution of the order of ~10 μrad and the narrow bandwidth of the crystal. The 10-J, 1-ps Multi-Terawatt (MTW) laser was used to characterize a set of Bragg crystal assemblies.

- O. M. Mannion, V. Yu. Glebov, C. J. Forrest, J. P. Knauer, V. N. Goncharov, S. P. Regan, T. C. Sangster, and C. Stoeckl (LLE) and M. Gatu Johnson (MIT) present the development of a new neutron time-of-flight diagnostic with an ultrafast instrument response function that has been fielded on the OMEGA laser in a highly collimated line of sight (p. 119). By using a small plastic scintillator volume, the detector provides a narrow instrument response of 1.7-ns FWHM while maintaining a large signal-to-noise ratio for neutron yields between 10^{10} to 10^{14}. The OMEGA Hardware Timing System is used with an optical fiducial to provide an absolute neutron time-of-flight measurement. The fast instrument response enables an accurate measurement of a primary-DT neutron peak shape, while the optical fiducial allows for an absolute neutron energy measurement.

Sid Sampat
Editor

Analysis of Trends in Experimental Observables and Reconstruction of the Implosion Dynamics for Direct-Drive Cryogenic Targets on OMEGA

Introduction

This article describes a technique for identifying trends in performance degradation for inertial confinement fusion implosion experiments. It is based on reconstruction of the implosion core with a combination of low- and mid-mode asymmetries. This technique was applied to an ensemble of hydro-equivalent deuterium–tritium implosions on OMEGA that achieved inferred hot-spot pressures ≈56±7 Gbar (Ref. 1). All the experimental observables pertaining to the core could be reconstructed simultaneously with the same combination of low and mid modes. This suggests that in addition to low modes, which can cause a degradation of the stagnation pressure, mid modes are present that reduce the size of the neutron and x-ray–producing volume. The systematic analysis shows that asymmetries can cause an overestimation of the measured areal density in these implosions. It is also found that an improvement in implosion symmetry resulting from correction of either the systematic mid or low modes would result in an increase of the hot-spot pressure from 56 Gbar to ≈80 Gbar and could produce a burning plasma when the implosion core is extrapolated to an equivalent 1.9-MJ [National Ignition Facility (NIF)-scale] symmetric direct illumination.[2] This represents the current standing and the future potential of the 100-Gbar Direct-Drive Program on OMEGA.

Observation of repeatable data trends in the direct-drive experiments motivated the development of this analysis technique. Since the cause of performance degradation for direct-drive implosions is not yet fully identified, we use trends from simulations of the deceleration phase to infer the degradation mechanisms involved. It is known that Rayleigh–Taylor instability (RTI)–induced distortion of the implosion core is a likely cause of degradation; the asymmetries are categorized into low and mid modes, as in Ref. 3. For low modes ($\ell < 6$) the RTI wavelength is longer than the hot-spot radius, whereas for mid modes ($6 < \ell < 40$) the asymmetry wavelength is shorter than the hot-spot radius. It was also shown in Ref. 3 that the two types of asymmetries have different effects on the neutron-averaged quantities. This article focuses on trends in the experimental observables arising from asymmetries of the implosion core. The two types of asymmetries are used as the independent basis to approximately reproduce all of the experimental observables. Trends arising from an effective 1-D–like degradation, which may be caused by shortcomings in the physical models used in hydrocodes, are also documented in this article for future investigations of 1-D degradation.

It is important to emphasize that the experimental observables cannot be explained by using low or mid modes alone; the comprehensive analysis presented here shows that a combination of the two is necessary for the core reconstruction. The exact mode numbers degrading the experiments have not been determined in this article; other combinations of modes could also produce the observables. However, it is shown that in order to reconstruct all the observables simultaneously, the overall balance between the degradation by low modes and the degradation by mid modes must be preserved.

The following sections (1) summarize the experimental data used in the analysis; (2) describe the reconstruction technique and discuss the trends in the stagnation observables—the inferred pressure, volume, shape, temperature, areal density, neutron burnwidth, and bang time—arising from the various degradation mechanisms; and (3) present our conclusions along with an energy extrapolation of direct-drive implosions and future applications for this analysis technique.

Trends in Cryogenic Implosion Experiments

It has been shown by Regan *et al.*[1] that direct-drive cryogenic implosions on OMEGA have achieved hot-spot pressures exceeding 50 Gbar—a performance that surpassed all previous implosions on OMEGA. The implosion performance was estimated based on the experimental observables: neutron yield, areal density, ion temperature, hot-spot volume, and neutron burnwidth. The "50-Gbar" implosions used standardized pulse shapes (either a single-picket pulse or a triple-picket pulse) and standardized targets (shown in Fig. 154.1). The 1-D performance is estimated from simulations using the hydrodynamic code *LILAC*.[4] It must be noted that the laser deposition models in *LILAC* were optimized to reproduce in-flight observables

like laser-energy deposition and shell trajectory.[5,6] The estimated implosion adiabat for this design is $\alpha \approx 3.5$ to 4 [the adiabat is defined as the ratio of the hydrodynamic pressure (P) and the Fermi pressure of a degenerate electron gas (P_F), at the interface of the hot spot and shell at the time when the laser-driven shocks reach this interface, i.e., $\alpha \equiv P/P_F$]. This is considered to be a mid-adiabat implosion design, with an adiabat higher than the indirect-drive "high-foot" design.[7–9] The peak hot-spot pressure in 1-D is estimated to be ~100 Gbar, close to the ~120 Gbar required to demonstrate hydro-equivalent ignition (the hydro-equivalent scaling of the implosion core has been discussed in Refs. 1, 2, 10, and 11). Notice that the pressure required for ignition with 1.9-MJ direct illumination is lower than the 350 to 400 Gbar required for ignition with the indirect-drive approach and the same laser energy. This is because for direct drive the conversion efficiency of laser energy to kinetic energy of the imploding shell is much higher, therefore allowing the implosion of greater DT fuel mass (i.e., larger target radius), which results in longer confinement times (τ). Since the Lawson ignition condition scales as $P_{ign}\tau$, the pressure required for ignition (P_{ign}) is lower with respect to that required for indirect drive.

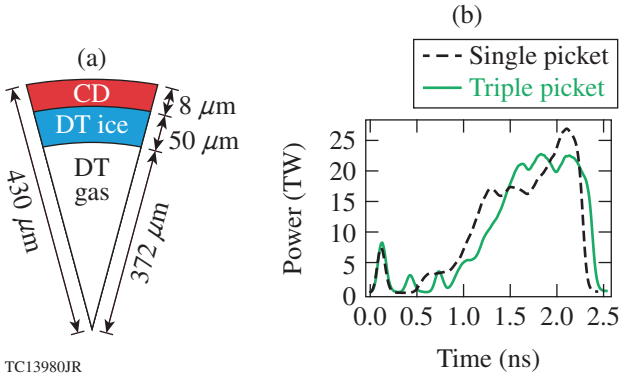

Figure 154.1
The pulse shapes and targets from the 50-Gbar implosions.[1]

Table 154.I lists the performance of several of these 50-Gbar implosions. The performance parameters are similar for all the shots. The neutron yields are ~4×10^{13}, at a yield degradation level $Y/Y_{1\text{-D}} \sim 0.3$, where $Y_{1\text{-D}}$ represents the post-shot 1-D

Table 154.I: The experimental observable and corresponding 1-D estimate from simulations [in brackets] for the ensemble of cryogenic implosions on OMEGA that produced ~50-Gbar pressure.

Shot	Y (×10^{13}) ±5%	X-ray $R_{17\%}$ (μm) ±0.5 μm	T_i (keV)[a] ±0.3 keV	ΔT_i (keV)	ρR (mg/cm^2)[b] ±31, ±19 mg/cm^2	Burnwidth (ps) ±6 ps	t_b–$t_{b,1\text{-D}}$ (ps) ±25 ps	P_{inf} (Gbar) ±7 Gbar
78959	4.39 [13.8]	21.3 [20.9]	3.63 [3.60]	0.54	213, 203 [232]	71 [54.1]	–16	52 [109]
78963	4.38 [16.3]	22.1 [19.8]	3.69 [3.74]	0.88	204, 208 [242]	67 [51.1]	–20	49 [126]
78967	3.76 [15.3]	21.4 [20.4]	3.65 [3.69]	0.85	179, 195 [238]	64 [51.1]	–46	50 [120]
78969	4.48 [14.1]	21.7 [21.4]	3.70 [3.66]	0.46	204, 197 [216]	59 [54.7]	–19	55 [104]
78971	3.77 [14.4]	22.1 [21.4]	3.69 [3.64]	1.06	220, 208 [222]	72 [20.9]	–27	44 [107]
77064	4.21 [12.5]	22.0 [20.4]	3.32 [3.48]	0.42	211, 191 [219]	62 [57.4]	–26	54 [108]
77066	4.11 [16.1]	21.9 [21.4]	3.18 [3.66]	0.57	221, 193 [228]	67 [52.9]	–20	56 [112]
77068	5.3 [17.0]	22.0 [22.0]	3.60 [3.82]	0.16	211, 194 [211]	66 [61.0]	–31	56 [97]
77070	4.02 [13.3]	20.3 [20.4]	3.40 [3.55]	0.23	220, 229 [239]	70 [52.6]	–11	56 [114]

[a]The ion temperatures were inferred using the instrument response function that was used prior to 2017. Currently an updated response function is being investigated that would result in temperatures that are ≈300 eV lower than stated and are within the experimental error.

[b]Both neutron time-of-flight and magnetic recoil spectrometer (second) measurements are listed.

simulation yield, calculated using *LILAC*. The hot-spot radii for all the shots are ~22 μm; they were estimated using time-resolved x-ray images.[12] The ion temperatures ($T_i \sim 3.5$ keV) are comparable to the temperatures from 1-D simulations, to within a 10% degradation level. The T_i's were measured using three different detectors—the chemical-vapor deposition (CVD) detector[13] and the 12-m and 15-m neutron time-of-flight (nTOF) detectors[14,15]—positioned along different implosion lines of sight; the minimum temperature is listed in Table 154.I. The variation in T_i measurement ΔT, which is the difference between the maximum and minimum measured temperatures, is considerable for a majority of the shots, ranging between 150 eV and 1.1 keV. It is observed that the measured areal densities are comparable to the 1-D estimates. The ρR is measured using the nTOF and magnetic recoil spectrometer (MRS)[16] detectors. The measured burnwidths are slightly longer than the 1-D estimate. The burnwidths are measured using the neutron temporal diagnostic (NTD).[17]

For direct-drive implosions on OMEGA, it is anticipated that the core is degraded by a combination of low and intermediate modes. Although the origin of the asymmetries is uncertain, low modes can arise from several factors, including long-wavelength target defects, target positioning, laser beam balance, and laser beam pointing.[18–20] In addition, the superposition of all 60 laser beams on OMEGA can produce overlapped intensity variations, which is expected to introduce intermediate-mode nonuniformities, similar to the mode ℓ = 10 in 2-D geometry. The cross-beam energy transfer (CBET) calculations by Edgell *et al.*,[21] shown in Fig. 154.2, represent the variation in laser-energy absorption at the target surface. When CBET is included, the nonuniformity is higher by 10×.

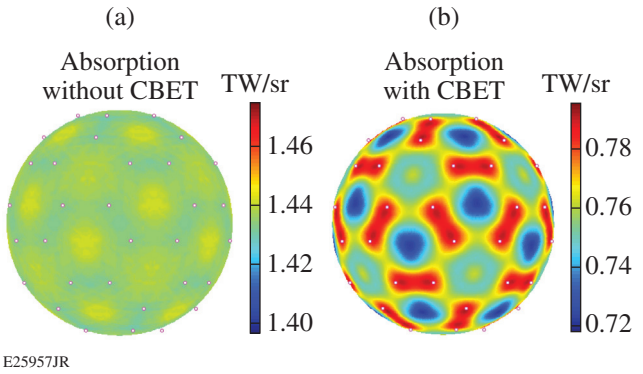

Figure 154.2
The laser power absorbed at the target surface is shown for calculations: (a) without considering cross-beam energy transfer (CBET) between the interacting laser beams and (b) with CBET.

These variations may be associated with the origin of mid-mode asymmetry in direct-drive implosions.

The Reconstruction Technique and Its Application

Unlike the conventional approach that involves full simulations of the implosions including nonuniformities from numerous sources, our technique focuses only on the final phase of an implosion. The final phase consists of the deceleration phase followed by stagnation and disassembly, which are critical in the production of fusion reaction neutrons detected by the nuclear diagnostics, and bremsstrahlung emission detected by the x-ray imaging diagnostics. Performance degradation results from a combination of nonuniformities: they are amplified by the RTI during the acceleration phase and can feed through to the inner surface, where they are further amplified during the deceleration phase by the RTI. Our technique is based on the multi-objective analysis of the degradation trends in the core observables and reconstruction of the implosion core.

The 2-D radiation–hydrodynamic code *DEC2D* is used to simulate the deceleration phase of implosions. The details of the code have been discussed in Ref. 10. Figure 154.3 provides an outline to our technique: the acceleration phase was simulated using *LILAC*;[4] it includes the laser drive with models for CBET[5] and nonlocal thermal transport.[6] The hydrodynamic profiles at the end of the laser pulse were used as initial conditions for the deceleration-phase simulations in 2-D. Initial perturbations for the deceleration-phase RTI were introduced at the interface of the shell and the hot spot through the angular variation of the velocity field.

Here we consider three categories of degradation: low-mode asymmetry, mid-mode asymmetry, and 1-D degradation. The low-mode trends are represented using mode 1 ("ℓ = 1"), mode 2 ("ℓ = 2"), and phase-reversed mode 2 ("ℓ = 2 *phase reversed*"); the RTI spike axis coincides with the simulation axis of symmetry for the former and is orthogonal for the latter. The mid-mode trends are represented using a mode-10 ("$\ell = 10^*$") and a multimode spectrum referred to as "*mid modes*." The $\ell = 10^*$ consists of a central mode 10 along with sideband modes 8 and 12 at 20% of central mode amplitude. The mid modes consist of a spectrum of modes given by $4 \le \ell \le 20$ at the same amplitude and a $1/\ell^2$ roll-off spectrum for higher modes $20 \le \ell \le 100$; the latter was motivated by the DT ice inner surface roughness spectrum. In simulations, the implosion performance was degraded by increasing the peak amplitude of the velocity perturbation spectrum. The 1-D degradation is incorporated as a degradation in the implosion velocity of the target, i.e., degradation in the initial condition

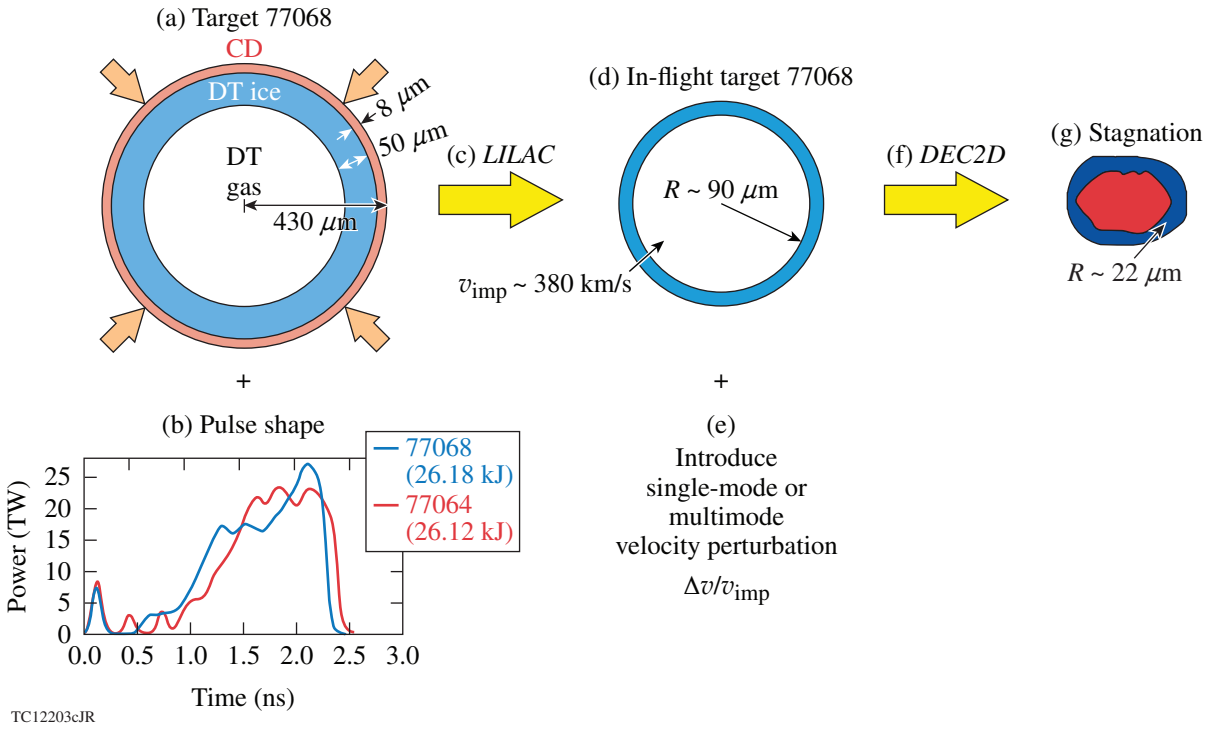

Figure 154.3
The procedure involved in the reconstruction technique. The (a) target and (b) pulse shape are used as initial conditions for the 1-D hydrodynamic code *LILAC*, which is used to (c) simulate the acceleration phase of implosions. The hydrodynamic profiles from the (d) in-flight target simulation are transferred to *DEC2D*; single- or multimode velocity perturbations are (e) introduced at the inner surface of the shell. (f) The deceleration phase of the implosion is simulated in 2-D, and (g) the stagnation parameters are extracted from these simulations.

of the deceleration-phase simulations; this has been denoted using "1-D v_{imp}." The scaling of the implosion observables with v_{imp} will be shown in the following sections. They are in reasonable agreement with Ref. 22, which instead uses a set of optimally performing *LILAC* simulations.

The single-picket pulse shape and target from OMEGA shot 77068 (used in this analysis) are shown in Fig. 154.3(b) (see blue curve). The analysis technique is very robust and can be applied to any implosion and any scale. The choice of shot 77068 was motivated by the fact that this was the best shot in terms of performance metric $\chi_{no\,\alpha}$ (Refs. 1 and 2) and other experimental observables such as yield and areal density. The target was driven with 26.18 kJ of laser energy to an implosion velocity of 380 km/s. The experimental observables, the 1-D simulation parameters, and the reconstructed observables for this shot are shown in Table 154.II. Notice that the experimental observables were reproduced using a combination of (1) the mid-modes component and (2) the low-mode component; a degradation of the simulated 1-D performance with either the low or mid modes alone would not produce the estimated results (this can be shown using the last two columns of Table 154.II). The velocity perturbation used for the reconstruction of shot 77068 is shown in Fig. 154.4; it consists of a combination of low-mode ($\ell = 2$) and mid-mode (a spectrum of mid modes) asymmetries. Figure 154.5 shows the shape of the hot spot and shell at the time of peak neutron production (i.e., bang time t_b); the final shape resembles a combination of a low-mode $\ell = 2$ and a dominant mid-mode $\ell = 10$. We emphasize that the exact mode numbers

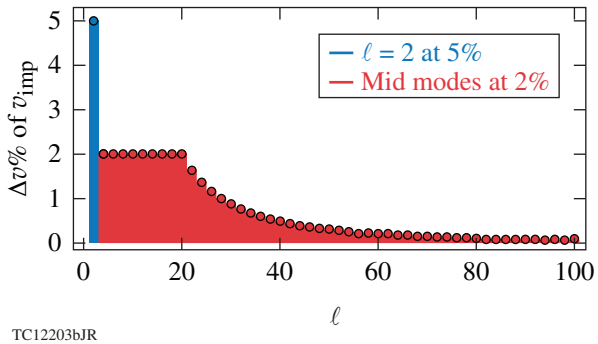

Figure 154.4
The initial velocity perturbation spectrum $\Delta v/v_{imp}\%$ (ℓ) that was used to synthetically reconstruct shot 77068 observables.

Table 154.II: Comparison of measurements with 1-D simulations (using *LILAC* and *DEC2D*) and 2-D simulations (using *DEC2D*).

Observables	Experiment shot 77068	1-D simulation	Reconstructed shot 77068	Mid modes component (1)	$\ell = 2$ component (2)	Mid modes $Y/Y_{1\text{-D}} \approx 0.3$	$\ell = 2$ $Y/Y_{1\text{-D}} \approx 0.3$
Yield	5.3×10^{13} (±5%)	1.7×10^{14}	5.3×10^{13}	7.9×10^{13}	9.8×10^{13}	5.3×10^{13}	5.3×10^{13}
P^* (Gbar)	56 (±7)	97	57	77	73	66	50
T_i (keV)	3.6 (±0.3)	3.82	3.70	3.78	3.71	3.64	3.42
R_{hs} (μm)	22 (±1)	22	22	20.9	23.4	21	25.3
t (ps)	66 (±6)	61	54	55	56	53	59
ρR (g/cm^2)	0.194 (±0.018)	0.211	0.194	0.222	0.193	0.211	0.180

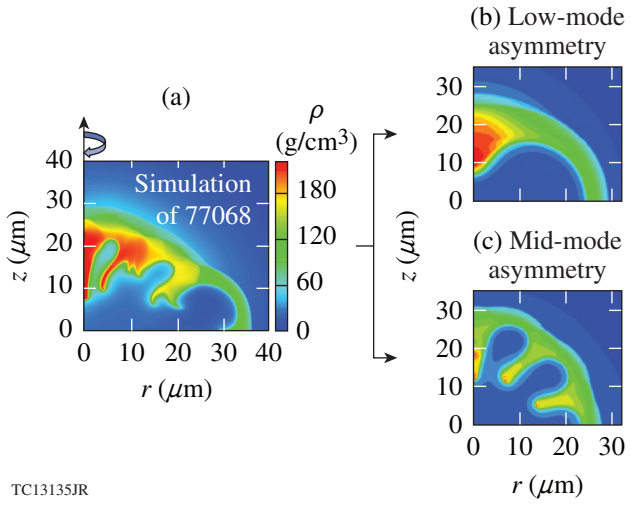

Figure 154.5
Plots illustrating a combination of low and mid modes that were used to reconstruct the core conditions of shot 77068. The density profiles at time of peak neutron production are shown for (a) reproduced shot 77068 with $Y/Y_{1\text{-D}} \approx 0.3$, (b) the low-mode $\ell = 2$ component at $Y/Y_{1\text{-D}} \approx 0.6$, and (c) an equivalent mid-mode $\ell = 10^*$ component at $Y/Y_{1\text{-D}} \approx 0.6$.

degrading the experimental performance cannot be inferred from this analysis technique, and other combinations of modes could also lead to the same reconstructed observables. However, the overall balance between the degradation by low modes and the degradation by mid modes on all of the observables must be preserved. To illustrate this, we also show trends from a different low mode: the $\ell = 1$ mode and the $\ell = 2$ asymmetry with a reversed phase. Although these modes are structurally different, the resulting trends are the same; for example, see trends in pressure and volume degradation in Figs. 154.6, 154.8, 154.12, 154.14, and 154.15. A discussion on the mode $\ell = 1$ asymmetry and an alternative reconstruction is shown in Appendix A of Ref. 23. Similarly, the mid modes (of the spectrum in Fig. 154.4) produces very similar degradation trends as the mode $\ell = 10^*$.

The following sections show the analysis of the 50-Gbar implosion results using this technique. The effect of low and mid modes on each of the implosion observables is discussed.

1. Inferred Hot-Spot Pressure

The hot-spot pressure is not directly measurable but it is inferred from other experimental observables using[24]

$$\frac{P_{\text{inf}}}{P_{\text{inf, l-D}}} = \sqrt{\left(\frac{Y}{Y_{\text{1-D}}}\right)\left(\frac{V}{V_{\text{1-D}}}\right)^{-1}\left[\frac{\left\langle \sigma v \right\rangle / T_i^2}{\left\langle \sigma v \right\rangle / T_i^2)_{\text{1-D}}}\right]^{-1}\left(\frac{\tau}{\tau_{\text{1-D}}}\right)^{-1}}, \quad (1)$$

where Y is the implosion yield obtained from experiments or simulations and is normalized with the 1-D yield ($Y_{1\text{-D}}$) from simulations. The $V/V_{1\text{-D}}$ is the normalized volume of the hot spot, calculated from the x-ray images of experiments or simulations. The fusion reactivity is a function of temperature only,[25] with $\sigma \approx 1$ to 2 for the temperature range of interest to ICF. The neutron burnwidth τ is the full width at half maximum of the neutron rate. The degradation trends for each of these observables will be shown in the following sections.

The degradation in pressure corresponding to a given degradation in yield is shown in Fig. 154.6. The degradation in inferred pressure is an outcome of the degradation in all of the measurable parameters shown in Eq. (1). For any yield degradation level, the low modes (in blue) result in a greater degradation of the hot-spot pressure as compared to mid modes (in red). The $\ell = 1$, $\ell = 2$, and $\ell = 2$ phase reversed produce nearly identical pressure degradation curves; also the $\ell = 10^*$ and mid modes produce similar curves. This is because for implosions with mid-mode asymmetries, the hot-spot volume is smaller as a result of cooling by penetration of the RTI spikes, but for low modes the volume is larger (see the next subsection). The

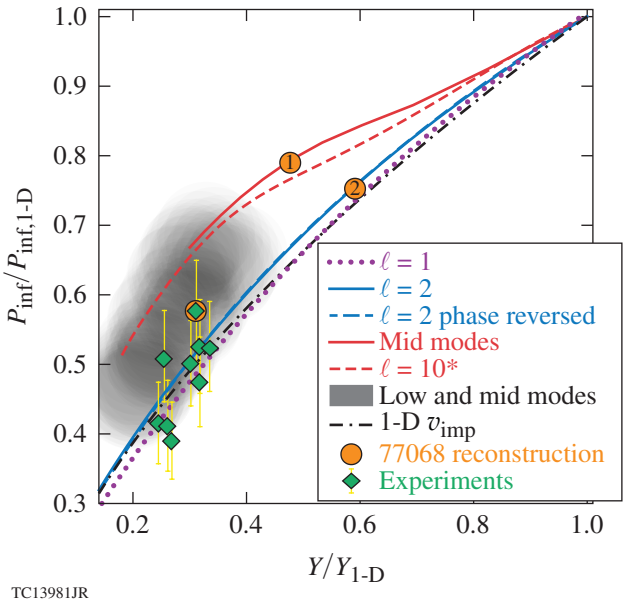

Figure 154.6
The degradation in inferred hot-spot pressure P_{inf}, normalized with 1-D pressure ($P_{inf,1\text{-}D}$), versus degradation in yield ($Y/Y_{1\text{-}D}$). This pressure is computed using Eq. (1) and the x-ray volume. The 50-Gbar shots in Table 154.I are shown in green. Reconstructed shot 77068 is shown in orange (overlapping the experimentally inferred pressure for shot 77068), with points (1) and (2) representing the degradation caused separately by the mid-mode and low-mode components. The gray-shaded region represents an ensemble of simulations using different amplitude combinations of $\ell = 2$ and mid modes; it is observed that these reproduce the experiments approximately.

gray-shaded region represents an ensemble of simulations using different amplitude combinations of $\ell = 2$ and mid modes, with the $\ell = 2$ amplitude varying between 4% and 7% of v_{imp} and the mid-mode amplitude varying between 2% and 4% of v_{imp}. The initial velocity perturbation spectrum of Fig. 154.4 could be used to reproduce the experimental pressure for shot 77068. The dashed–dotted black line in Fig. 154.6 shows the 1-D pressure scaling with implosion velocity; it follows $P_{inf} \sim v_{imp}^{3.72}$. The corresponding yield scaling with implosion velocity follows $Y \sim v_{imp}^{6.26}$. The implosion velocity degradation is a simplistic method to model the degradation in implosion convergence; it is useful for comparing trends. In experiments, degradation in implosion convergence can be caused by the following: very short scale nonuniformities arising from laser imprinting or reduced laser-to-capsule drive with respect to simulation, and preheating caused by superthermal electrons (which decrease the implosion convergence by increasing the implosion adiabat α).

Notice that in Fig. 154.6 the pressure degradation curve for the 1-D v_{imp} coincides with the low-mode curves ($\ell = 1$, $\ell = 2$, and $\ell = 2$ phase reversed), but is different from the mid-mode curves ($\ell = 10^*$ and mid modes). This can be explained based on Ref. 3. First, the hot spot is not isobaric for implosions with mid-mode asymmetries; second, the inferred pressure for mid modes is the average pressure of the x-ray–producing region of the hot spot. The x-ray–producing volume, however larger than the neutron-producing volume, is still smaller than the total hot-spot volume including the bubbles (i.e., $V_{\langle hs \rangle}$ of Ref. 3). As a result, the inferred pressure for implosions with mid-mode asymmetry using the x-ray volume is higher than the average hot-spot pressure. However, for the low-mode asymmetry or 1-D v_{imp} degradation curves (Fig. 154.6) the hot spot is approximately isobaric and the neutron and x-ray volumes are comparable to the total hot-spot volume ($V_{\langle hs \rangle}$, see Fig. 7 of Ref. 3); therefore, the inferred pressures are similar. If the neutron-producing volume is used instead of the x-ray volume, the inferred pressure for mid modes would be similar to the clean (1-D) value—irrespective of the yield, also shown in Fig. 7 of Ref. 3. In summary, the inferred pressure for implosions with mid-mode asymmetry is higher than that of low modes at the same yield-degradation level, as a result of a non-isobaric hot spot and a smaller hot-spot volume for the former.

2. Estimation of the Hot-Spot Size: Using Time-Gated Self-Emission Images

Time-resolved images of the core x-ray self-emission, as shown in Fig. 154.7, have been used to estimate the hot-spot volume.[12] Here R_{17} is the radius at 17% of peak intensity and $V_{x\ ray}/V_{x\ ray,1\text{-}D} = \left(R_{17}/R_{17,1\text{-}D}\right)^3$.

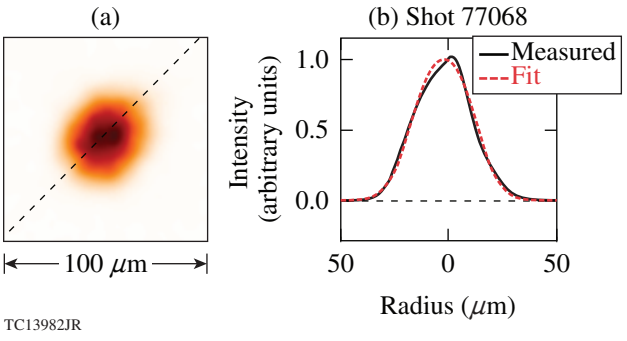

Figure 154.7
(a) An x-ray image of the hot spot at stagnation for shot 77068, obtained using a time-resolved Kirkpatrick–Baez (KB) framed camera with a 4- to-8 keV photon energy range and a 6-μm spatial resolution.[12] (b) The measured and fit x-ray profiles along the dashed line.

The effect of asymmetries on the hot-spot volume is shown in Fig. 154.8, where with increasing mode amplitude, the x-ray volume increases for low modes and decreases for mid modes. By cooling the plasma within the RTI bubbles, mid-mode asymmetries cause a reduction in the x-ray–emitting volume.

The gray-shaded region (representing the ensemble of simulations) shows that the volume estimated using a combination of low and mid modes is in agreement with the measured volume for the 50-Gbar shots, illustrating that the experiments can be reconstructed using such combinations of low and mid modes. The effect of an implosion velocity degradation on the x-ray volume has been shown using the dashed black line (1-D v_{imp}); it follows the scaling $V_{x\ ray} \sim v_{imp}^{-2.14}$. Notice that this curve coincides with the low-mode curves, but it is different from the mid-mode asymmetry curves for the same reasons as previously explained.

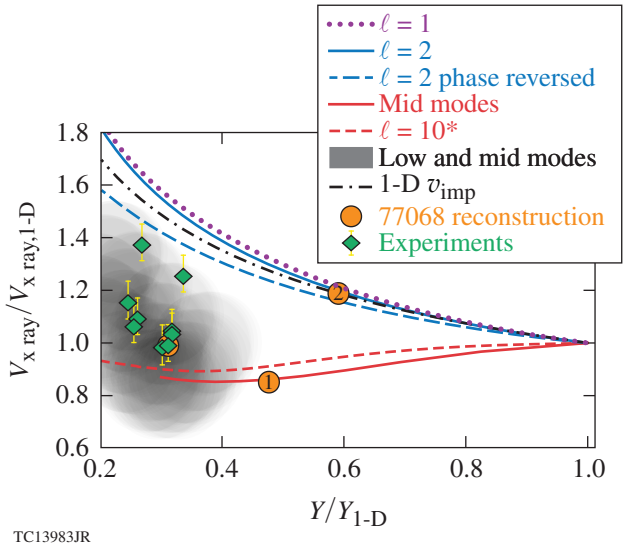

Figure 154.8
Plot showing the volume of the hot spot, obtained from time-resolved x-ray images and normalized with the 1-D volume $\left(V_{x\ ray}/V_{x\ ray,1\text{-}D}\right)$, versus the yield degradation $Y/Y_{1\text{-}D}$. The 50-Gbar shots in Table 154.I are shown in green. The reconstructed shot 77068 is shown in orange (overlapping the x-ray volume for shot 77068), with points (1) and (2) representing the degradation caused by the mid- and low-mode components, separately. The gray-shaded region represents an ensemble of simulations using different amplitude combination of $\ell = 2$ and mid modes; it is observed that these reproduce the experiments.

The disassembly phase of implosions is different for low- and mid-mode asymmetries. The physical mechanism involved has been discussed in Ref. 3. In this section we discuss signatures in time-resolved x-ray images that could aid the detection of mid modes. Time-resolved x-ray images (i.e., with 10-ps gate width) were produced from the simulations using the atomic physics code *Spect3D*.[26,27] These images were normalized with the maximum intensity for each image and fit with the following function:

$$f(x,y) = e^{-\left[(x/a)^2+(y/b)^2\right]^{\eta/2}}. \qquad (2)$$

The R_{17} was obtained from the fit using

$$R_{17} = \sqrt{a \times b}\left[\log(0.17)\right]^{1/\eta}.$$

The index η represents the index of the super-Gaussian fit, with $\eta = 2$ representing a Gaussian function. Figure 154.9 shows that during the disassembly (i.e., for $t > t_b$), the R_{17} decreases with time for mid modes, whereas it increases for low modes with respect to 1-D. A similar trend was also observed for other arbitrary definitions of the radius, i.e., radius at 37%, 50%, and 75% of peak intensity. Since detecting mid modes in experiments is challenging (because of the limited spatial resolution of the detectors), the above time-evolution trends in the x-ray images could motivate future experiments.

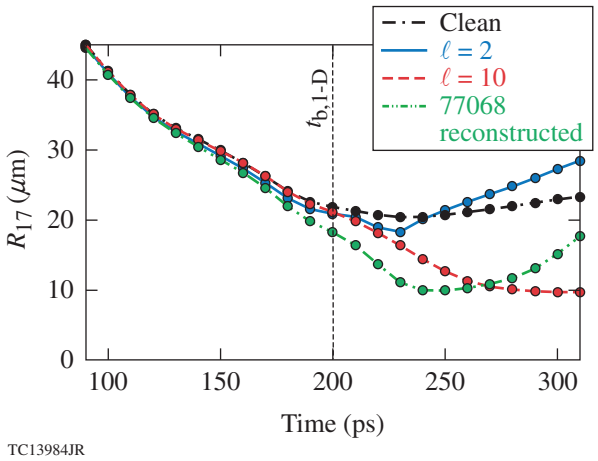

Figure 154.9
Plot showing the time evolution of the x-ray R_{17} obtained from simulations. This is shown for the symmetric case (black curve), low-mode $\ell = 2$ case with $Y/Y_{1\text{-}D} = 0.6$ (blue curve), mid-mode $\ell = 10$ case with $Y/Y_{1\text{-}D} = 0.6$ (red curve), and the reproduced case with $Y/Y_{1\text{-}D} \approx 0.3$ (green curve) for simulations of shot 77068.

3. Shape Analysis of Time-Integrated Self-Emission Images

In this section we discuss how asymmetries influence the time-integrated x-ray images. Since the photon statistics (i.e., determined by the number of incident photons) are insufficient for the 10- to-15-ps time-gated images (in the previous section), we do not use those images to infer the shape of the hot spot; instead we use the time-integrated images obtained using the gated monochromatic x-ray imaging (GMXI) module.[28] In Fig. 154.10 the first column shows the density profile and plasma-flow pattern at bang time. The corresponding synthetic self-emission images along with lineouts across a different axis are shown in the second and third columns, respectively. The cross sections were taken through the center

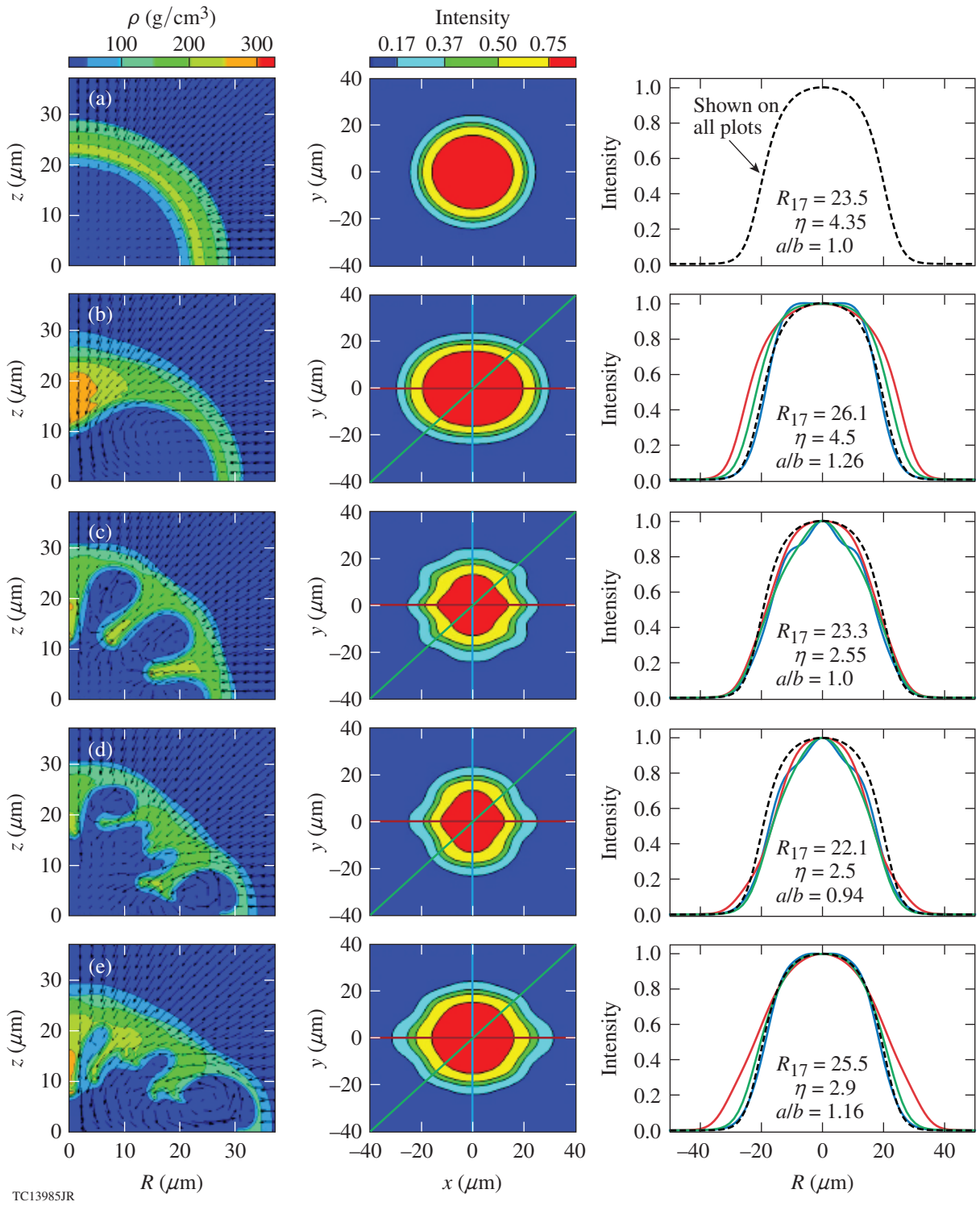

Figure 154.10
Contour plots of the density profile and plasma flow pattern at bang time (first column), time-integrated synthetic x-ray emission images (second column), and image lineouts (third column). The black dashed line represents the lineout of the symmetric image; it is shown on all plots in the third column for reference. The lineouts along the three different axes are labeled with different colors (red, blue, and green). The 2-D super-Gaussian fit parameters have been included. The images for (a) symmetric implosion, (b) $\ell = 2$ at $Y/Y_{1\text{-D}} = 0.6$, (c) $\ell = 10^{*}$ at $Y/Y_{1\text{-D}} = 0.6$, (d) mid modes (spectrum) with 2% ΔV at $Y/Y_{1\text{-D}} = 0.47$, and (e) reconstructed shot 77068 are shown.

of the image; they are marked on the contour plot with the same color as on the intensity plot. The x-ray images were reconstructed with the same filter, point spread function (PSF), and detector response as the experimental shot 77068; i.e., filtered with 6.5 mil of Be and 2 mil of Al, which transmit x rays in the 4- to 8-keV range, and a 7.5-μm PSF. The images were fit using the function shown in Eq. (2). The R_{17} of the time-integrated images, the ellipticity parameter (a/b), and the super-Gaussian exponent η were calculated from the fit. It was found that low modes cause an increase in the a/b and R_{17}, with the index η comparable or larger than the 1-D case. In comparison, mid modes cause a reduction in the index η because the mid modes exhibit several low-temperature bubbles surrounding the hot center, producing a more-gradual intensity variation with radius. The mid modes have a negligible effect on the calculated a/b and R_{17}.

Table 154.III shows the properties of the time-integrated x-ray images for the 50-Gbar shots. It is observed that for all of the shots, the time-integrated R_{17} is larger than the time-resolved images by 3 to 4 μm (see Table 154.I). This is in consistent agreement with our analysis showing that the time-integrated radius (R_{17}) is larger than the radius at bang time for low modes ($\ell = 2$) in simulations. The $\eta < \eta_{1\text{-D}}$ indicates the presence of mid modes and $a/b > 1$ indicates the presence of low modes in the implosions.

Table 154.III: The properties for the time-integrated GMXI[28] x-ray images from experiments.

Shot	R_{17} (mm) ±0.5 mm	η ±0.2	a/b ±0.01	Filter 6.5 mil Be+
78959	25.6	2.7	1.16	3 mil Al
78963	28.1	2.3	1.17	3 mil Al
78967	26.7	2.3	1.16	3 mil Al
78969	27.4	2.6	1.16	3 mil Al
78971	27.1	1.9	1.20	3 mil Al
77064	27.7	2.6	1.11	2 mil Al
77066	26.8	2.6	1.10	2 mil Al
77068	26.7	2.69	1.16	2 mil Al
77070	25.9	2.56	1.13	2 mil Al

Figure 154.11 shows the time-integrated image for shot 77068 and the reconstructed image. The agreement in shape and other parameters (R_{17}, a/b, and η) supports the presence of systematic mid modes along with low modes in the 50-Gbar implosions. In summary, low modes increase the ellipticity parameter (a/b) and radius (R_{17}) with respect to 1-D from the time-integrated x-ray images, and mid modes produce a lower super-Gaussian index η. A combination of low- and mid-mode asymmetries can be used to reproduce the experimental images.

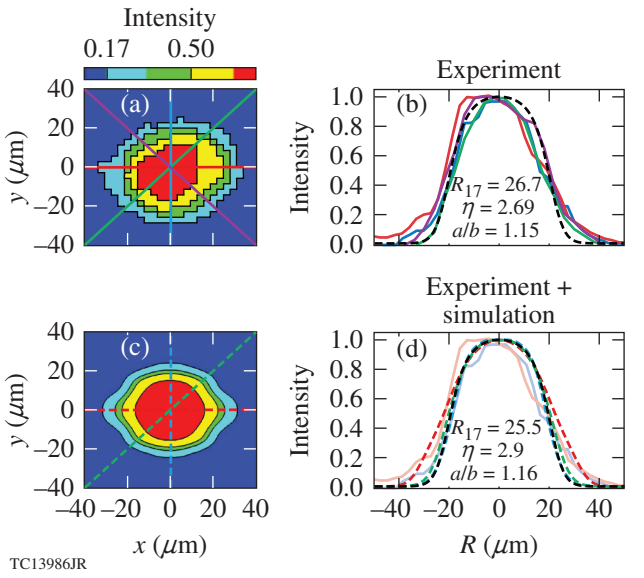

Figure 154.11
A comparison between time-integrated x-ray images for shot 77068 obtained from [(a) and (b)] experiments and [(c) and (d)] the reconstructed simulation. The lineouts along the different axes are labeled with different colors (red, blue, green, and purple), the lineouts for the experimental image are represented using solid curves [in (b) and (d)], and the simulations are represented using dashed curves [in (d)]. The lineout for the symmetric case is shown with black dashed curve [in (b) and (d)] for reference. The super-Gaussian fit parameters for both (b) experiment and (d) simulation are listed.

4. Neutron-Averaged Ion Temperature

Figure 154.12 shows the degradation in ion temperature $\left(T_i / T_{i,\,1\text{-D}}\right)$ with degradation in yield ($Y/Y_{1\text{-D}}$). It is observed that asymmetries cause a small degradation in $T_i / T_{i,\,1\text{-D}}$, within 10% to 15% of the 1-D value, for all yield degradation levels above $Y/Y_{1\text{-D}} > 0.2$. This is because the temperature of the region of the hot spot that produces fusion neutrons, i.e., the hot region, is only marginally affected by asymmetries (see Ref. 3). The results from simulations with a combination of low- and mid-mode asymmetries are in the gray-shaded area. The green diamonds, representing the 50-Gbar experiments, fall within the gray-shaded region. The temperature scaling with implosion velocity follows $T_i \sim v_{imp}^{0.91}$ in 1-D, which is estimated from the dashed black curve. It is observed that at the same yield degradation ($Y/Y_{1\text{-D}}$) level, the temperature is lower for the curve representing implosion velocity degradation (1-D v_{imp}) as compared to asymmetries.

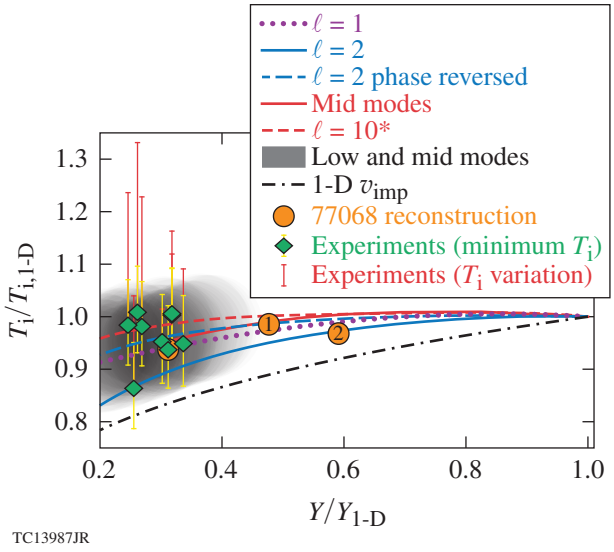

Figure 154.12
Plot showing degradation in neutron-averaged ion temperature $\left(T_i/T_{i,1\text{-}D}\right)$ versus the degradation in yield ($Y/Y_{1\text{-}D}$). The points in green represent the minimum ion temperature measured for the 50-Gbar shots; the red bar associated with each data point extends to the maximum ion temperature measurement. The reconstructed shot 77068 is shown in orange (overlapping with data); the points (1) and (2) represent degradation caused by the mid-mode and low-mode components separately. The gray-shaded region represents an ensemble of simulations using different amplitude combination of $\ell = 2$ and mid modes; it is observed that these reproduce the experiments.

The variation in ion-temperature measurements between detectors is shown by the red bars in Fig. 154.12; the length of the red bar represents the maximum variation $\Delta T_{max} = T_{i,max} - T_{i,min}$ between measurements along different lines of sight for the shot. It is known that flows[29–31] in the neutron-producing region of the hot spot, marked with arrows in Fig. 154.10 (first column), can affect the temperature measurements. This results in a higher apparent temperature, depending on the detector line of sight. The 50-Gbar implosions exhibit a considerable variation in ion-temperature measurements. The maximum variation in neutron-averaged ion temperature (ΔT_{max}) versus yield degradation level is also shown in Fig. 154.13. The experiments (represented by the green diamonds) exhibit shot-to-shot variation in ΔT_{max}, which is possibly caused by the differences in flow effects along different lines of sight. For the simulations, the apparent temperatures (i.e., including flow effects) were calculated using the Murphy[32] formulation [see Eq. (20) of Ref. 32]

$$T_{sp/bub}^{(app)}\,[\text{keV}] = T_i\,[\text{keV}] + \left(m_\alpha + m_n\right)\left\langle v_{sp/bub}^2\right\rangle[\text{keV}] \quad (3)$$

with

$$T_i = \frac{\iint T n_D n_T \langle\sigma v\rangle \, dV dt}{\iint n_D n_T \langle\sigma v\rangle \, dV dt}, \quad (4)$$

$$\left\langle v_{sp/bub}^2\right\rangle = \frac{\iint v_{sp/bub}^2 n_D n_T \langle\sigma v\rangle \, dV dt}{\iint n_D n_T \langle\sigma v\rangle \, dV dt} \quad (5)$$

for which we estimate (approximately) the neutron-averaged flow broadening along the spike or bubble axis using the above Eqs. (3)–(5). In the simulations (except the $\ell = 2$ phase-reversed case) the spike axis corresponds to the z axis (represented by subscript "sp") and the bubble axis is the r axis (represented by subscript "bub") (see Fig. 154.5; see Fig. 154.10 for the velocity flow field). Notice that the apparent temperature $T_{sp/bub}^{(app)} \geq T_i$ is the neutron average temperature. The maximum variation possible is estimated using the following

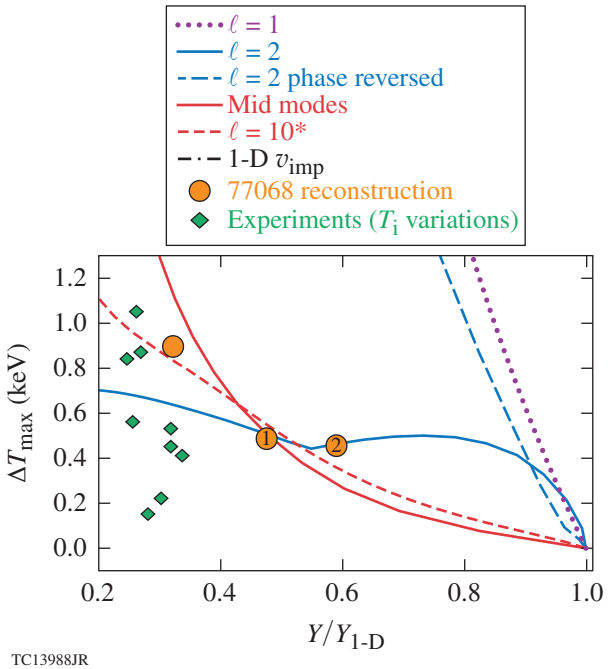

Figure 154.13
Plot showing the maximum variation in ion-temperature measurements (ΔT_{max}) versus degradation in yield ($Y/Y_{1\text{-}D}$). For the 50-Gbar experiments (green diamonds), the ΔT_{max} is given by $\Delta T_{max} = T_{i,max} - T_{i,min}$ across measurements along different lines of sight. The simulations show the maximum variation in ion temperature (ΔT_{max}) estimated using Eq. (6). The reconstructed shot 77068 is shown in orange, with points (1) and (2) representing the degradation caused by the mid- and low-mode components, separately.

$$\Delta T_{max} = \max\left[T_{sp}^{(app)}, T_{bub}^{(app)}\right] - T_i, \quad (6)$$

where $T_{sp}^{(app)}$ [or $T_{bub}^{(app)}$] is the apparent temperature measured by a detector sitting on the spike axis [or bubble axis] and T_i is the neutron-averaged ion temperature calculated without including the flow effects (as expected, the variation in ion temperature is negligible for symmetric implosions). We find that the ΔT_{max} from experiments and the calculated ΔT_{max} are comparable for implosions with $\ell = 2$ and mid modes. The $\ell = 1$ mode and the phase-reversed low mode ($\ell = 2$ phase reversed) produce higher variations in apparent temperature than others in the simulations because these implosions are influenced by significant bulk flow motion within the relatively large neutron-producing volume.

Our technique, which uses a combination of low and mid modes, can be used to consistently reproduce the neutron-averaged temperature measurements and estimate the variation in temperature for the 50-Gbar experiments.

5. Implosion Areal Density

The effect of asymmetries on the areal density (ρR) is discussed in this section. The ρR's estimated from the down-scattered ratio (DSR) of the neutron spectrum obtained from experiments and simulations are shown in Fig. 154.14. It is observed that the measured ρR's are comparable to the corresponding 1-D estimated values (from *LILAC*) although the yields are heavily degraded ($Y/Y_{1\text{-D}} \sim 0.3$) in the experiments. In Fig. 154.14, the ρR scaling with symmetric yield (produced by decreasing the implosion velocity) is shown by the dashed black curve (1-D v_{imp}); it follows $\rho R \sim v_{imp}^{1.42}$. In the simulations the ρR's are calculated using the Monte Carlo neutron-tracking post-processor code *IRIS3D*.[33] Notice that the ρR for implosions with asymmetries is always higher than the 1-D v_{imp} curve. The ρR is a parameter dependent on the implosion convergence; for symmetric implosions the yield and ρR decrease with decreasing convergence according to the 1-D v_{imp} curve of Fig. 154.14. Instead, for distorted implosions, the convergence of the spikes can be high, producing a relatively higher ρR, but this does not increase the yield (see Ref. 3). The ρR for implosions with mid-mode asymmetry (represented by the $\ell = 10^*$ and mid-mode curves) is comparable to the estimated $\rho R_{1\text{-D}}$. This is because for mid modes, multiple RTI spikes approach the implosion center, producing a compressed plasma with a higher ρR. For the low-mode cases ($\ell = 1$, $\ell = 2$, and $\ell = 2$ phase reversed), this effect is relatively small; nevertheless, the ρR's at any given $Y/Y_{1\text{-D}}$ are higher than the 1-D ρR versus yield scaling (represented by the 1-D v_{imp}).

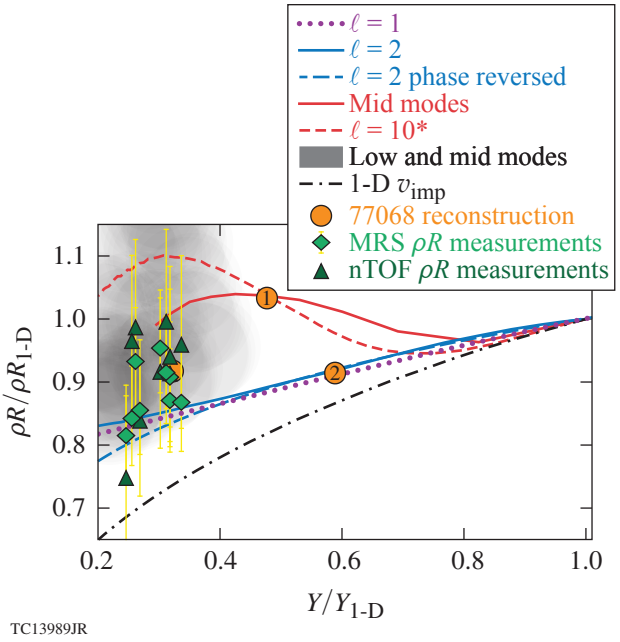

Figure 154.14
Plot showing the degradation in areal density (i.e., ρR estimated from DSR) versus degradation in yield. The ρR and yield are normalized with the 1-D estimated values. The neutron time-of-flight (nTOF, triangles) and magnetic recoil spectrometer (MRS, diamonds) ρR measurements for the 50-Gbar shots are shown in green. The reconstructed shot 77068 is shown in orange (overlapping with data), with points (1) and (2) representing degradation caused by the mid-mode and low-mode components, separately. The gray-shaded region represents an ensemble of simulations using different amplitude combinations of $\ell = 2$ and mid modes; it is observed that these reproduce the experiments.

A combination of low and mid modes (shown by the gray-shaded region) could be used to reconstruct the ρR for the 50-Gbar shots (shown as green triangles and diamonds). The measurements along with consideration of the asymmetry trends suggest that a fraction of the measured ρR is provided by the cold spikes and ablated mass accumulated in the bubbles surrounding the burn volume; therefore, they do not contribute to fusion-yield production but augment the areal density.

6. Burnwidth and Bang Time

Figure 154.15(a) shows a plot of burnwidth degradation ($\tau/\tau_{1\text{-D}}$) with yield degradation ($Y/Y_{1\text{-D}}$). It is observed that the burnwidths from NTD measurements are longer than the 1-D values (from *LILAC*), i.e., $\tau/\tau_{1\text{-D}} > 1$; however, the estimated error in the NTD burnwidths is ~±7 ps. The scaling of burnwidth with implosion velocity is represented using the 1-D v_{imp} curve; it follows $\tau \sim v_{imp}^{-1.2}$.

In simulations with asymmetries, the burnwidth shows a modest reduction with degradation in yield. However, for very large low-mode asymmetries (i.e., $Y/Y_{1\text{-D}} < 0.4$), the burnwidth

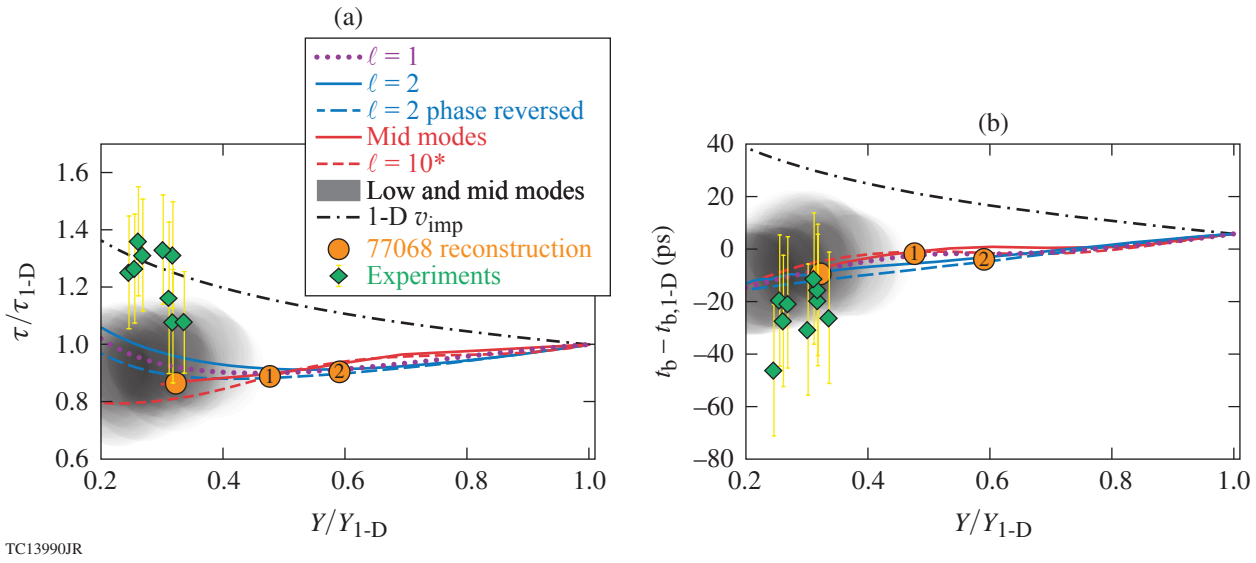

Figure 154.15
Plots showing (a) burnwidth ($\tau/\tau_{1\text{-D}}$) and (b) shift in bang time with respect to the 1-D simulations (i.e., $t_b - t_{b,1\text{-D}}$) versus degradation in yield ($Y/Y_{1\text{-D}}$). The green diamonds represent the experimental results from the 50-Gbar implosions (Table 154.I). The reconstructed shot 77068 is shown in orange; points (1) and (2) represent degradation caused by the mid-mode and low-mode components, separately. The gray-shaded region represents an ensemble of simulations using different amplitude combinations of $\ell = 2$ and mid modes.

increases with decreasing yield; this phenomenon has been described in Ref. 3. A combination of low and mid modes (shown in the gray-shaded region) produce burnwidths that are comparable to the 1-D estimated burnwidth (from *LILAC*) to within 30%, but, on average, they are shorter than the burnwidths for the 50-Gbar experiments.

Figure 154.15(b) shows a shift in bang time compared to the 1-D estimated values ($t_b - t_{b,1\text{-D}}$) with degradation in yield ($Y/Y_{1\text{-D}}$). The bang time from experiments (measured using the NTD) are shifted earlier in time; however, the estimated error in the NTD bang times are considerable ($\approx \pm 25$ ps). Notice that unlike burnwidths, this is in agreement with the asymmetry trends, which also shift the bang time forward, but it is opposite to what an implosion velocity (i.e., 1-D) degradation would do, as shown by the 1-D v_{imp} curve for which the bang time occurs later, i.e., $(t_b - t_{b,1\text{-D}}) > 0$.

We propose two possible explanations for the discrepancy between burnwidth and bang time. One possibility is the inaccuracy of the measurements. The NTD measurements for burnwidth and bang time have large error bars and probably are influenced by systematic effects that are not being considered here. It is possible that the actual burnwidths are 10 to 15 ps shorter and the actual bang times are 10 to 15 ps later than what are measured. The 10 to 15 ps in both burnwidth and bang time are within the measurement error. This would mean that both are consistent with the trends arising from asymmetries.

The second possible explanation is that in addition to a low mode (like $\ell = 1$ or $\ell = 2$) and a mid mode (like $\ell = 10$), there is a 1-D degradation in implosion convergence. This would mean that there is a systematic difference in the laser drive that is not accounted for by the laser–plasma coupling models (or equation-of-state model) in the *LILAC* simulations. Therefore the burnwidths are indeed longer, as measured by the NTD and predicted by the 1-D v_{imp} scaling curves. However, the bang time, which depends on the history of the acceleration phase, is not correctly captured by the simplistic deceleration-phase scaling (represented by the 1-D v_{imp} curves). In experiments, a degradation in implosion convergence can be caused by the following: very short scale nonuniformities arising from laser imprinting or reduced laser-to-capsule drive with respect to simulation, and preheating caused by super-thermal electrons (which decrease the implosion convergence by increasing the implosion adiabat α).

Conclusions and Future Application

This article discussed a technique to investigate the implosion performance degradation mechanisms based on trends in the experimental observables. This technique was applied to an ensemble of DT cryogenic implosions on OMEGA that

achieved hot-spot pressures of ~50 Gbar (Ref. 1). It was shown that a combination of low- and mid-mode asymmetries could be used to reconstruct the implosion core.[2] In addition to the presence of low modes, which cause a degradation of the stagnation pressure, it was shown that mid-mode asymmetries have a significant impact on the implosion performance. While it is challenging to image mid-mode asymmetries in implosions, this technique can be used to infer the effect of mid modes on the observables. It was shown that mid modes decrease the hot-spot size (i.e., time-resolved x-ray R_{17}) and lead to center-peaked, time-integrated x-ray images (i.e., a smaller super-Gaussian exponent η compared to a symmetric implosion). This occurs because the region of mid-mode bubbles surrounding the hot center introduces a gradual variation in the x-ray intensity. A consistent explanation for the ion-temperature, areal-density, volume, and pressure measurements for the 50-Gbar shots was described. The possible reasons behind the modest discrepancies between burnwidth and bang time were discussed based on the measurements and the predicted degradation trends.

Determining the exact mode numbers that degrade the experiments was not the goal of this article; other combinations of modes could also produce the observables simultaneously. The overall balance between the degradation by low modes and mid modes must be preserved. It was also shown that the trends in the implosion observables arising from an $\ell = 1$ asymmetry[34–36] are similar to the other low modes like the $\ell = 2$ or $\ell = 2$ with a reversed phase; only the ion-temperature variation introduced by the $\ell = 1$ mode or $\ell = 2$ with a reversed phase is higher than the $\ell = 2$ (or all other higher modes) and the experiments. In principle, it is challenging to distinguish between these modes given the quality of the experimental images.

This article complements the more detailed analysis of asymmetries provided in Ref. 3 with analysis of experiments. It was shown in Ref. 3 that the neutron-averaged observables can differ from the hot-spot volume-averaged quantities; the differences, although small for low modes, are more pronounced for mid-mode asymmetries. In other words, the energy distribution at stagnation is similar for both asymmetry types; however, the fusion reaction distribution is different. Also described is an analysis technique that ventures a consistent correlation between all the experimental observables of the implosion core, based on studies of asymmetries and 1-D degradation. It must be emphasized that this multi-objective prescription for analyzing cryogenic implosions simultaneously takes into account trends in all of the experimental observables, therefore providing leads to investigating systematic errors in measurements.

The analysis of several repeats of the cryogenic implosion experiments suggests a systematic degradation mechanism affecting the implosions. A combination of low and mid modes was used to reconstruct all the experimental observables pertaining to the core. It was shown that the experimental observables cannot be explained using either low- or mid-mode asymmetries separately; therefore, a combination was necessary for the reconstruction.

Quantitative measurements and mitigation of asymmetries in direct-drive implosions constitute a major component of the ongoing and future research at the Omega Laser Facility. To mention a few: A monochromatic backlighter using the short pulse from OMEGA EP has been developed to radiograph the cryogenic implosions on OMEGA.[37] Systematic low-mode asymmetries were observed using narrowband self-emission x-ray images from a titanium tracer layer placed at the fuel–shell interface.[38] Laser phase-plate designs are being investigated to improve laser coupling and drive symmetry.[39] Multiple self-emission x-ray images are being used to measure asymmetry modes up to the end of the laser drive, followed by adjustments in the laser beam energy balance to correct the asymmetry modes.[40] To motivate this effort, we provide an estimate of the implosion performance with improved implosion symmetry, i.e., by correcting the systematic and repeatably occurring asymmetries. It is estimated that mitigation of low- and mid-mode asymmetries would both result in an increase in the fusion yield, however, through an increase in the hot-spot pressure (from 56 Gbar to 80 Gbar) for low modes and an increase in the burn volume for mid-modes.

Figure 154.16 shows that an improvement in implosion core symmetry by correcting either the systematic mid or low modes, included in the reconstruction of shot 77068 (and other 50-Gbar shots[1]), can produce a burning plasma (i.e., $Q_\alpha \geq 1$, see Ref. 41) when extrapolated to a NIF-scale implosion core; i.e., an equivalent 1.9-MJ implosion with symmetric direct illumination (see Ref. 2). Note that the pressure values shown in Fig. 154.16 are relevant for the targets discussed in this article and serve only as an approximate gauge; in fact, implosion performance must be estimated using a Lawson-type metric like the $\chi_{\mathrm{no}\,\alpha}$. For extrapolated shot 77068, it is estimated that multidimensional effects produce a small uncertainty in the performance metric and the yield amplification factor. It was repeated in Ref. 16 that the $\chi_{\mathrm{no}\,\alpha} = 0.61$ produces a 2× amplification in yield in the simulation, in agreement with the 1-D alpha-heating model[41,42] and the fit formula: yield amplification $Y_{\mathrm{amp}} \approx \left(1 - \chi_{\mathrm{no}\,\alpha}/0.96\right)^{-0.75}$. In addition, it must be

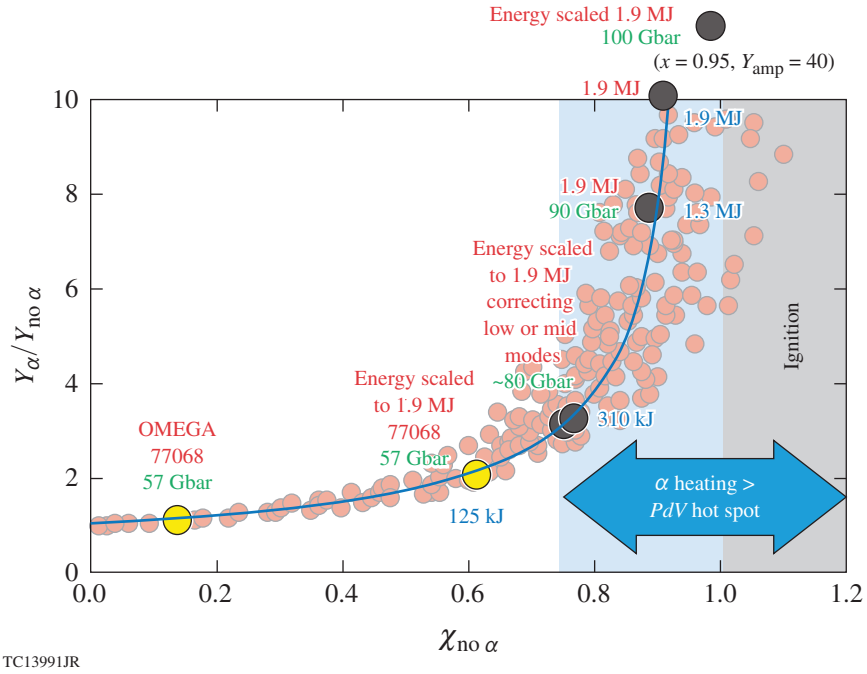

Figure 154.16

Plot of yield amplification versus $\chi_{no\,\alpha}$ (Ref. 41), where $\chi_{no\,\alpha}$ is estimated using Eq. (3) of Ref. 2; 1-D and 2-D simulation results (red circles) and $Y_\alpha / Y_{no\,\alpha} = \left(1-\chi_{no\,\alpha}/0.96\right)^{-0.75}$ (blue curve) are shown. The Lawson ignition condition $\chi_{no\,\alpha} \geq 1$ and the burning plasma regime $Q_\alpha \geq 1$ are shown by the gray- and blue-shaded regions, respectively. OMEGA shot 77068 (with 26 kJ of laser energy) and its equivalent implosion extrapolated to a 1.9-MJ driver[2] are shown (yellow circles); they exhibit inferred core pressures of 57 Gbar. Correcting either the low- or mid-mode component of this implosion can produce ≈80-Gbar pressure (see Table 154.II), with its performance approaching the burning plasma regime (simulation results are shown by black circles). Improving the asymmetry sources by 0.1× produces 90-Gbar pressure. The 1-D design has a hot-spot pressure of ≈100 Gbar with $\chi_{no\,\alpha} = 0.95$ and a yield amplification of $Y_{amp} = 40$. The fusion energy output corresponding to each of the extrapolated simulations is shown in blue. Shot 77068 when extrapolated to 1.9 MJ is estimated to produce 125 kJ of fusion energy—much higher (≈5×) than indirect-drive implosions at the same $\chi_{no\,\alpha}$. Improving the asymmetry sources by 0.01× is estimated to produce 1.9 MJ of fusion energy (the same as the laser driver). The relatively higher fusion energy output accentuates the advantage of the direct-drive approach over indirect drive with the same laser energy.

noted that in Fig. 154.16 the $\chi_{no\,\alpha}$ for other representative points (black circles) are increasingly accurate; this is because they are obtained by improving the implosion symmetry, as can be observed from the proximity of the simulation points (black circles) to the 1-D fit (blue curve).

In the future this analysis technique will be applied to different 1-D implosion designs (i.e., with different implosion adiabat, obtained from optimization of pulse shape and target dimensions), which would enhance the understanding and possibly lead to identification of the degradation sources for OMEGA direct-drive implosions.

ACKNOWLEDGMENT

This research has been supported by the U.S. Department of Energy under Cooperative Agreements DE-FC02-04ER54789 (Office of Fusion Energy Sciences) and DE-NA0001944 (National Nuclear Security Administration), the NYSERDA, and by the Lawrence Livermore National Laboratory under subcontract B614207.

REFERENCES

1. S. P. Regan, V. N. Goncharov, I. V. Igumenshchev, T. C. Sangster, R. Betti, A. Bose, T. R. Boehly, M. J. Bonino, E. M. Campbell, D. Cao, T. J. B. Collins, R. S. Craxton, A. K. Davis, J. A. Delettrez, D. H. Edgell, R. Epstein, C. J. Forrest, J. A. Frenje, D. H. Froula, M. Gatu Johnson, V. Yu. Glebov, D. R. Harding, M. Hohenberger, S. X. Hu, D. Jacobs-Perkins, R. T. Janezic, M. Karasik, R. L. Keck, J. H. Kelly, T. J. Kessler, J. P. Knauer, T. Z. Kosc, S. J. Loucks, J. A. Marozas, F. J. Marshall, R. L. McCrory, P. W. McKenty, D. D. Meyerhofer, D. T. Michel, J. F. Myatt, S. P. Obenschain, R. D. Petrasso, R. B. Radha, B. Rice, M. Rosenberg, A. J. Schmitt, M. J. Schmitt, W. Seka, W. T. Shmayda, M. J. Shoup III, A. Shvydky, S. Skupsky, A. A. Solodov, C. Stoeckl, W. Theobald, J. Ulreich, M. D. Wittman, K. M. Woo, B. Yaakobi, and J. D. Zuegel, Phys. Rev. Lett. **117**, 025001 (2016); **117**, 059903(E) (2016).

2. A. Bose, K. M. Woo, R. Betti, E. M. Campbell, D. Mangino, A. R. Christopherson, R. L. McCrory, R. Nora, S. P. Regan, V. N. Goncharov, T. C. Sangster, C. J. Forrest, J. Frenje, M. Gatu Johnson, V. Yu. Glebov, J. P. Knauer, F. J. Marshall, C. Stoeckl, and W. Theobald, Phys. Rev. E **94**, 011201(R) (2016).

3. A. Bose, R. Betti, D. Shvarts, and K. M. Woo, Phys. Plasmas **24**, 102704 (2017).

4. J. Delettrez, R. Epstein, M. C. Richardson, P. A. Jaanimagi, and B. L. Henke, Phys. Rev. A **36**, 3926 (1987).

5. I. V. Igumenshchev, W. Seka, D. H. Edgell, D. T. Michel, D. H. Froula, V. N. Goncharov, R. S. Craxton, L. Divol, R. Epstein, R. Follett, J. H. Kelly, T. Z. Kosc, A. V. Maximov, R. L. McCrory, D. D. Meyerhofer, P. Michel, J. F. Myatt, T. C. Sangster, A. Shvydky, S. Skupsky, and C. Stoeckl, Phys. Plasmas **19**, 056314 (2012).

6. V. N. Goncharov, T. C. Sangster, P. B. Radha, R. Betti, T. R. Boehly, T. J. B. Collins, R. S. Craxton, J. A. Delettrez, R. Epstein, V. Yu. Glebov, S. X. Hu, I. V. Igumenshchev, J. P. Knauer, S. J. Loucks, J. A. Marozas, F. J. Marshall, R. L. McCrory, P. W. McKenty, D. D. Meyerhofer, S. P. Regan, W. Seka, S. Skupsky, V. A. Smalyuk, J. M. Soures, C. Stoeckl, D. Shvarts, J. A. Frenje, R. D. Petrasso, C. K. Li, F. Séguin, W. Manheimer, and D. G. Colombant, Phys. Plasmas **15**, 056310 (2008).

7. O. A. Hurricane *et al*., Nature **506**, 343 (2014).

8. T. Döppner, D. A. Callahan, O. A. Hurricane, D. E. Hinkel, T. Ma, H. S. Park, L. F. Berzak Hopkins, D. T. Casey, P. Celliers, E. L. Dewald, T. R. Dittrich, S. W. Haan, A. L. Kritcher, A. MacPhee, S. Le Pape, A. Pak, P. K. Patel, P. T. Springer, J. D. Salmonson, R. Tommasini, L. R. Benedetti, E. Bond, D. K. Bradley, J. Caggiano, J. Church, S. Dixit, D. Edgell, M. J. Edwards, D. N. Fittinghoff, J. Frenje, M. Gatu Johnson, G. Grim, R. Hatarik, M. Havre, H. Herrmann, N. Izumi, S. F. Khan, J. L. Kline, J. Knauer, G. A. Kyrala, O. L. Landen, F. E. Merrill, J. Moody, A. S. Moore, A. Nikroo, J. E. Ralph, B. A. Remington, H. F. Robey, D. Sayre, M. Schneider, H. Streckert, R. Town, D. Turnbull, P. L. Volegov, A. Wan, K. Widmann, C. H. Wilde, and C. Yeamans, Phys. Rev. Lett. **115**, 055001 (2015).

9. O. A. Hurricane, D. A. Callahan, D. T. Casey, E. L. Dewald, T. R. Dittrich, T. Döppner, M. A. Barrios Garcia, D. E. Hinkel, L. F. Berzak Hopkins, P. Kervin, J. L. Kline, S. Le Pape, T. Ma, A. G. MacPhee, J. L. Milovich, J. Moody, A. E. Pak, P. K. Patel, H.-S. Park, B. A. Remington, H. F. Robey, J. D. Salmonson, P. T. Springer, R. Tommasini, L. R. Benedetti, J. A. Caggiano, P. Celliers, C. Cerjan, R. Dylla-Spears, D. Edgell, M. J. Edwards, D. Fittinghoff, G. P. Grim, N. Guler, N. Izumi, J. A. Frenje, M. Gatu Johnson, S. Haan, R. Hatarik, H. Herrmann, S. Khan, J. Knauer, B. J. Kozioziemski, A. L. Kritcher, G. Kyrala, S. A. Maclaren, F. E. Merrill, P. Michel, J. Ralph, J. S. Ross, J. R. Rygg, M. B. Schneider, B. K. Spears, K. Widmann, and C. B. Yeamans, Phys. Plasmas **21**, 056314 (2014).

10. A. Bose, K. M. Woo, R. Nora, and R. Betti, Phys. Plasmas **22**, 072702 (2015).

11. R. Nora, R. Betti, K. S. Anderson, A. Shvydky, A. Bose, K. M. Woo, A. R. Christopherson, J. A. Marozas, T. J. B. Collins, P. B. Radha, S. X. Hu, R. Epstein, F. J. Marshall, R. L. McCrory, T. C. Sangster, and D. D. Meyerhofer, Phys. Plasmas **21**, 056316 (2014).

12. F. J. Marshall, R. E. Bahr, V. N. Goncharov, V. Yu. Glebov, B. Peng, S. P. Regan, T. C. Sangster, and C. Stoeckl, Rev. Sci. Instrum. **88**, 093702 (2017).

13. G. J. Schmid, R. L. Griffith, N. Izumi, J. A. Koch, R. A. Lerche, M. J. Moran, T. W. Phillips, R. E. Turner, V. Yu. Glebov, T. C. Sangster, and C. Stoeckl, Rev. Sci. Instrum. **74**, 1828 (2003).

14. V. Yu. Glebov, D. D. Meyerhofer, C. Stoeckl, and J. D. Zuegel, Rev. Sci. Instrum. **72**, 824 (2001).

15. V. Yu. Glebov, C. J. Forrest, K. L. Marshall, M. Romanofsky, T. C. Sangster, M. J. Shoup III, and C. Stoeckl, Rev. Sci. Instrum. **85**, 11E102 (2014).

16. J. A. Frenje, D. T. Casey, C. K. Li, J. R. Rygg, F. H. Séguin, R. D. Petrasso, V. Yu. Glebov, D. D. Meyerhofer, T. C. Sangster, S. Hatchett, S. Haan, C. Cerjan, O. Landen, M. Moran, P. Song, D. C. Wilson, and R. J. Leeper, Rev. Sci. Instrum. **79**, 10E502 (2008).

17. C. Stoeckl, R. Boni, F. Ehrne, C. J. Forrest, V. Yu. Glebov, J. Katz, D. J. Lonobile, J. Magoon, S. P. Regan, M. J. Shoup III, A. Sorce, C. Sorce, T. C. Sangster, and D. Weiner, Rev. Sci. Instrum. **87**, 053501 (2016).

18. S. X. Hu, P. B. Radha, J. A. Marozas, R. Betti, T. J. B. Collins, R. S. Craxton, J. A. Delettrez, D. H. Edgell, R. Epstein, V. N. Goncharov, I. V. Igumenshchev, F. J. Marshall, R. L. McCrory, D. D. Meyerhofer, S. P. Regan, T. C. Sangster, S. Skupsky, V. A. Smalyuk, Y. Elbaz, and D. Shvarts, Phys. Plasmas **16**, 112706 (2009).

19. V. N. Goncharov, T. C. Sangster, R. Betti, T. R. Boehly, M. J. Bonino, T. J. B. Collins, R. S. Craxton, J. A. Delettrez, D. H. Edgell, R. Epstein, R. K. Follett, C. J. Forrest, D. H. Froula, V. Yu. Glebov, D. R. Harding, R. J. Henchen, S. X. Hu, I. V. Igumenshchev, R. Janezic, J. H. Kelly, T. J. Kessler, T. Z. Kosc, S. J. Loucks, J. A. Marozas, F. J. Marshall, A. V. Maximov, R. L. McCrory, P. W. McKenty, D. D. Meyerhofer, D. T. Michel, J. F. Myatt, R. Nora, P. B. Radha, S. P. Regan, W. Seka, W. T. Shmayda, R. W. Short, A. Shvydky, S. Skupsky, C. Stoeckl, B. Yaakobi, J. A. Frenje, M. Gatu-Johnson, R. D. Petrasso, and D. T. Casey, Phys. Plasmas **21**, 056315 (2014).

20. I. V. Igumenshchev, D. T. Michel, R. C. Shah, E. M. Campbell, R. Epstein, C. J. Forrest, V. Yu. Glebov, V. N. Goncharov, J. P. Knauer, F. J. Marshall, R. L. McCrory, S. P. Regan, T. C. Sangster, C. Stoeckl, A. J. Schmitt, and S. Obenschain, Phys. Plasmas **24**, 056307 (2017).

21. D. H. Edgell, R. K. Follett, I. V. Igumenshchev, J. F. Myatt, J. G. Shaw, and D. H. Froula, Phys. Plasmas **24**, 062706 (2017); *LLE Review Quarterly Report* **150**, 61, Laboratory for Laser Energetics, University of Rochester, Rochester, NY, LLE Document No. DOE/NA/1944-1331 (2017). Copies may be obtained from the National Technical Information Service, Springfield, VA 22161.

22. C. D. Zhou and R. Betti, Phys. Plasmas **14**, 072703 (2007).

23. A. Bose, R. Betti, D. Mangino, D. Patel, K. M. Woo, A. R. Christopherson, V. Gopalaswamy, S. P. Regan, V. N. Goncharov, C. J. Forrest, J. A. Frenje, M. Gatu Johnson, V. Yu. Glebov, J. P. Knauer, F. J. Marshall, R. Shah, C. Stoeckl, W. Theobald, T. C. Sangster, and E. M. Campbell, "Analysis of Trends in Implosion Observables for Direct-Drive Cryogenic Implosions on OMEGA," to be published in Physics of Plasmas.

24. C. Cerjan, P. T. Springer, and S. M. Sepke, Phys. Plasmas **20**, 056319 (2013).

25. H. S. Bosch and G. M. Hale, Nucl. Fusion **32**, 611 (1992); **33**, 1919(E) (1993).

26. J. J. MacFarlane *et al*., High Energy Density Phys. **3**, 181 (2007).

27. R. Epstein, S. P. Regan, B. A. Hammel, L. J. Suter, H. A. Scott, M. A. Barrios, D. K. Bradley, D. A. Callahan, C. Cerjan, G. W. Collins, S. N. Dixit, T. Döppner, M. J. Edwards, D. R. Farley, K. B. Fournier, S. Glenn,

S. H. Glenzer, I. E. Golovkin, A. Hamza, D. G. Hicks, N. Izumi, O. S. Jones, M. H. Key, J. D. Kilkenny, J. L. Kline, G. A. Kyrala, O. L. Landen, T. Ma, J. J. MacFarlane, A. J. Mackinnon, R. C. Mancini, R. L. McCrory, D. D. Meyerhofer, N. B. Meezan, A. Nikroo, H.-S. Park, P. K. Patel, J. E. Ralph, B. A. Remington, T. C. Sangster, V. A. Smalyuk, P. T. Springer, R. P. J. Town, and J. L. Tucker, AIP Conf. Proc. **1811**, 190004 (2017).

28. F. J. Marshall and J. A. Oertel, Rev. Sci. Instrum. **68**, 735 (1997).

29. H. Brysk, Plasma Phys. **15**, 611 (1973)

30. R. E. Chrien *et al*., Phys. Plasmas **5**, 768 (1998).

31. B. Appelbe and J. Chittenden, Plasma Phys. Control. Fusion **53**, 045002 (2011).

32. T. J. Murphy, Phys. Plasmas **21**, 072701 (2014).

33. *LLE Review Quarterly Report* **150**, 100, Laboratory for Laser Energetics, University of Rochester, Rochester, NY, NTIS Order No. DOE/NA/1944-1331 (2017). Copies may be obtained from the National Technical Information Service, Springfield, VA 22161.

34. B. K. Spears, M. J. Edwards, S. Hatchett, J. Kilkenny, J. Knauer, A. Kritcher, J. Lindl, D. Munro, P. Patel, H. F. Robey, and R. P. J. Town, Phys. Plasmas **21**, 042702 (2014).

35. I. V. Igumenshchev, D. T. Michel, R. C. Shah, E. M. Campbell, R. Epstein, C. J. Forrest, V. Yu. Glebov, V. N. Goncharov, J. P. Knauer, F. J. Marshall, R. L. McCrory, S. P. Regan, T. C. Sangster, C. Stoeckl, A. J. Schmitt, and S. Obenschain, Phys. Plasmas **24**, 056307 (2017).

36. K. M. Woo, R. Betti, Shvarts. D., A. Bose, D. Patel, R. Yan, P.-Y. Chang, O. M. Mannion, R. Epstein, J. A. Delettrez, M. Charissis, K. S. Anderson, P. B. Radha, A. Shvydky, I. V. Igumenshchev, V. Gopalaswamy, A. R. Christopherson, J. Sanz, and H. Aluie, Phys. Plasmas **25**, 052704 (2018).

37. C. Stoeckl, R. Epstein, R. Betti, W. Bittle, J. A. Delettrez, C. J. Forrest, V. Yu. Glebov, V. N. Goncharov, D. R. Harding, I. V. Igumenshchev, D. W. Jacobs-Perkins, R. T. Janezic, J. H. Kelly, T. Z. Kosc, R. L. McCrory, D. T. Michel, C. Mileham, P. W. McKenty, F. J. Marshall, S. F. B. Morse, S. P. Regan, P. B. Radha, B. S. Rice, T. C. Sangster, M. J. Shoup III, W. T. Shmayda, C. Sorce, W. Theobald, J. Ulreich, M. D. Wittman, D. D. Meyerhofer, J. A. Frenje, M. Gatu Johnson, and R. D. Petrasso, Phys. Plasmas **24**, 056304 (2017).

38. R. C. Shah, B. M. Haines, F. J. Wysocki, J. F. Benage, J. A. Fooks, V. Glebov, P. Hakel, M. Hoppe, I. V. Igumenshchev, G. Kagan, R. C. Mancini, F. J. Marshall, D. T. Michel, T. J. Murphy, M. E. Schoff, K. Silverstein, C. Stoeckl, and B. Yaakobi, Phys. Rev. Lett. **118**, 135001 (2017).

39. I. V. Igumenshchev, V. N. Goncharov, F. J. Marshall, J. P. Knauer, E. M. Campbell, C. J. Forrest, D. H. Froula, V. Yu. Glebov, R. L. McCrory, S. P. Regan, T. C. Sangster, S. Skupsky, and C. Stoeckl, Phys. Plasmas **23**, 052702 (2016).

40. D. T. Michel, I. V. Igumenshchev, A. K. Davis, D. H. Edgell, D. H. Froula, D. W. Jacobs-Perkins, V. N. Goncharov, S. P. Regan, A. Shvydky, and E. M. Campbell, Phys. Rev. Lett. **120**, 125001 (2018).

41. R. Betti, A. R. Christopherson, B. K. Spears, R. Nora, A. Bose, J. Howard, K. M. Woo, M. J. Edwards, and J. Sanz, Phys. Rev. Lett. **114**, 255003 (2015).

42. A. R. Christopherson, R. Betti, A. Bose, J. Howard, K. M. Woo, E. M. Campbell, J. Sanz, and B. K. Spears, Phys. Plasmas **25**, 012703 (2018).

Ionization Waves of Arbitrary Velocity

Efforts to engineer plasmas for the generation and manipulation of electromagnetic waves have been growing in sophistication. Recent examples of plasma-based photonic devices include mirrors,[1] wave plates,[2,3] polarizers,[4,5] q-plates,[6] radiation sources ranging from x rays[7,8] to THz,[9,10] laser amplifiers,[11–13] and laser compressors.[14] Many such tools rely on the controlled propagation of an ionization front, the velocity of which can strongly impact the performance of the system.

For example, a light source propagating within an ionization front will undergo "photon acceleration"—a continual upshift of its frequency induced by the dynamic refractive index gradient.[15–18] However, the frequency upshift results in group velocity acceleration and a tendency for the source to decouple from the constant velocity ionization front. To highlight a second example, recent simulations of plasma-based laser amplification showed that a dynamic ionization front propagating just ahead of an amplifying seed pulse provides enhanced control over plasma parameters as well as improved noise suppression.[19]

A technique providing unprecedented spatiotemporal control over the propagation of laser intensity—the "flying focus"—was recently pioneered.[20,21] A chirped broadband laser pulse with duration τ (with the sign of τ indicating the direction of the chirp) is focused by a highly chromatic diffractive optic that produces an extended focal region with length l. In general, each color reaches best focus at a unique time, and the rate at which the location of best focus moves is uniquely determined by the ratio τ/l for a linearly chirped beam. Peak laser intensity can be made to propagate at any velocity, from $-\infty$ to $+\infty$, by tuning τ/l.

Subsequent calculations have demonstrated that a dynamic ionization front will track the velocity of an intensity isosurface at the ionization threshold of a background gas.[22] Therefore, the flying focus can be used to produce an ionization wave of arbitrary velocity (IWAV). These simulations also revealed that backward IWAV propagation relative to the ionizing laser mitigates ionization-induced refraction, which typically degrades the formation of long, uniform laser-produced plasmas.[23,24]

In this article, we report the first experimental demonstration of ionization waves of arbitrary velocity. The velocities ranged from subluminal to superluminal (slower and faster than the speed of light, respectively), both forward- and backward-propagating relative to the ionizing laser. Ionization fronts were observed to propagate smoothly over several millimeters in most cases, although subluminal forward propagation was degraded by ionization-induced refraction, as expected. To diagnose the IWAV propagation, a novel spectrally resolved schlieren diagnostic was developed, exploiting the linear time–frequency relationship of a chirped probe. These data demonstrate the feasibility of flying-focus–produced IWAV's for use in applications like those discussed above.

The experimental setup is shown in Fig. 154.17. An Nd:YLF laser with optical parametric chirped-pulse amplification (OPCPA) generated a beam with central wavelength λ_0 = 1.053 μm and full-width-at-half-maximum (FWHM) bandwidth $\Delta\lambda$ = 8.7 nm, providing the source for the pump and probe beams. The linearly chirped pulse duration was tuned by adjusting the grating position in the stretcher. A beam splitter directed 85% of the energy to the pump path. A diffractive lens with radially varying groove density, described more fully in Ref. 21, was used to focus the pump beam in ambient air. Its focal length for the central wavelength of the pump was f_0 = 51.1 cm, and it produced an extended focal region of length $l = f_0\Delta\lambda/\lambda_0$ = 4.2 mm, with the red and blue sides of the spectrum focusing nearest to and farthest from the lens, respectively. With an energy of 25.5±0.3 mJ, the pump could create a plasma channel in air at best focus for pulse durations ranging from best compression (<1 ps) up to ≈40 ps.

The additional 15% transmitted through the beam splitter was down-collimated, converted to 2ω using a second-harmonic crystal, and directed to the plasma orthogonal to the pump axis for use as a probe beam. An optical delay path was used to time the probe such that its passage coincided with the IWAV propagation. The plasma channel was imaged along the probe path onto the entrance slit of a 0.3-m imaging spectrometer equipped with a 1200-grooves/mm grating. A

knife edge was used as a schlieren stop in a focal location of the probe beam along the imaging path. It was oriented in order to probe gradients orthogonal to the axis of the plasma channel (i.e., the edge of the channel). A Finger Lakes charge-coupled–device (CCD) camera was used to capture images at the exit plane of the spectrometer.

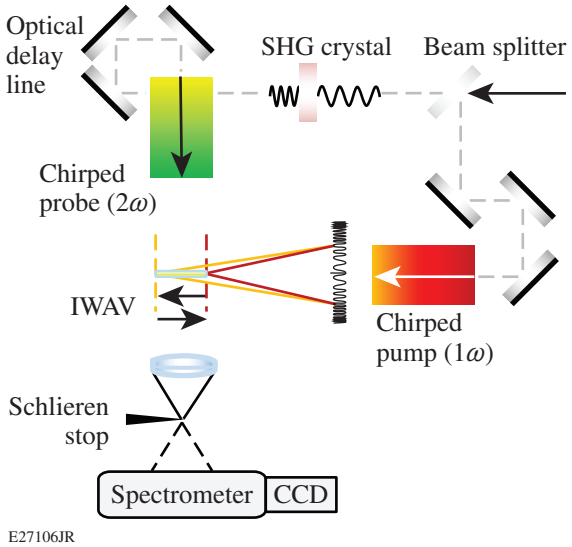

Figure 154.17
Experimental setup: a 1.053-μm laser with tunable pulse duration τ was split into two beams. The pump beam remained 1ω and was focused by a diffractive optic to produce an ionization wave of arbitrary velocity (IWAV). The probe beam was converted to 2ω and diagnosed the plasma channel in a side-on geometry coincident with the plasma formation. A spectrally resolved schlieren diagnostic was used to determine the ionization front velocity. SHG: second-harmonic generation; CCD: charge-coupled device.

Removing the schlieren stop, opening the spectrometer slit, and operating the spectrometer in zero order, the CCD camera captured a 2-D shadowgraphy image of the plasma channel. Inserting the schlieren stop with otherwise the same parameters yielded a 2-D schlieren image. The spectrometer slit was then centered on the edge of the plasma channel (the location of maximum signal) and the grating was set to disperse the probe wavelengths orthogonal to the plasma channel axis. The spectral axis effectively provides picosecond time resolution as a result of the linear time-frequency dependence of the chirped probe beam.

Figure 154.18(a) shows the flying focus focal-spot velocity (expected to correspond directly to the ionization front velocity) given by $v_f = dz/dt = c\,(1 + \tau c/l)^{-1}$ (Ref. 21). Negative values of the pulse duration τ correspond to negatively chirped beams, with the blue end of the spectrum preceding the red end in time. The IWAV velocity is converted to an observable on the spectrally resolved schlieren measurement by noting that $dz/dt = (dz/d\lambda)\,(d\lambda/dt)$, and for the linearly chirped second-harmonic probe beam, the derivative $d\lambda/dt = -\Delta\lambda/2\tau$ (i.e., the FWHM spectral bandwidth of the probe—half that of the pump—is spread out over the FWHM pulse duration). Therefore, the expected edge slope on the schlieren diagnostic is given by

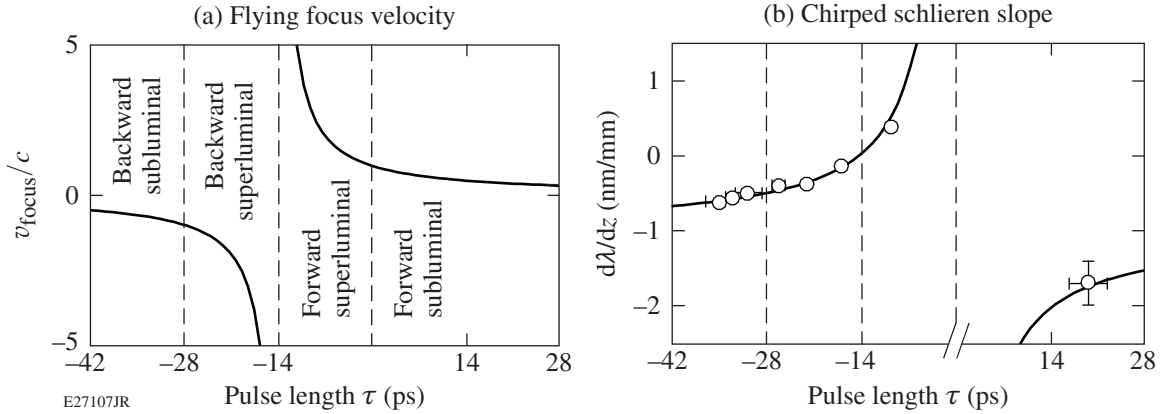

Figure 154.18
(a) The flying focus velocity (i.e., the speed at which constant intensity isosurfaces move near best focus) is determined by the ratio of the chirped-pulse duration to the length of the extended chromatic focal region produced by the diffractive optic. Any velocity (including faster than the speed of light) is achievable in both the forward and backward directions relative to the laser propagation. (b) For the spectrally resolved schlieren diagnostic, the expected linear slope of an edge marking the onset of plasma formation is plotted as a function of pump and probe pulse duration. The overlaid points correspond to the experimental data. Both forward- and backward-propagating ionization waves of arbitrary velocity were produced, with velocities both less than and greater than the speed of light in each direction.

$d\lambda/dt = -\Delta\lambda/2\,[(1/c\tau) + (1/l)]$; this slope is plotted as a function of pulse length in Fig. 154.18(b).

Results from the spectrally resolved schlieren diagnostic are shown in Fig. 154.19. Each image is an average of five to ten shots divided by an average of several reference spectra, which were obtained by removing the schlieren stop and blocking the pump beam. The pump beam propagated from left to right along the z axis. An edge-finding routine was used to find the time of the ionization wave's appearance at each axial location; vertical lineouts were taken averaging over ≈30-μm increments along the z axis, and typically the value closest to 10% along the spectral axis was specified as the edge. The slope was determined from a linear best fit through the data points. The points found by the edge-finding routine, as well as the best fit result, are plotted with the data in Fig. 154.19.

In Figs. 154.19(a)–154.19(c), there is no signal on the blue side of the probe spectrum because that portion of the probe passed the pump's focal region prior to any plasma formation. The edge of the signal then appears and varies linearly, as expected, over a distance of at least 2 to 3 mm. Hydrodynamic expansion of the plasma channel is negligible on the time scale of the probe beam, so the plasma channel persists and continues to refract all subsequent probe colors on the red side of the spectrum. Figures 154.19(a) and 154.19(b) are both examples of superluminal backward propagation since $-2l/c < \tau < -l/c$; the latter example is close to $t = -l/c$, in which case each color arrives at best focus simultaneously and the IWAV travels across the focal region instantaneously.

Figure 154.19(c) shows an example of superluminal forward propagation, with $-l/c < \tau < 0$. Note that although the IWAV co-propagates with the ionizing laser, ionization-induced refraction did not compromise the channel formation. This naturally follows from the fact that the shorter-wavelength photons that ionize the plasma at larger values along the z axis are ahead of the ionization front and are therefore not affected by propagation through the existing plasma. (Similar logic explains why superluminal IWAV propagation does not violate causality.)

In Fig. 154.19(d), the laser is positively chirped, which always yields a subluminal forward-propagating flying focus. Note that the sign of the slope expected in the schlieren images is the same as for negatively chirped backward propagation because two sign changes (the IWAV propagation direction and the direction of the probe chirp) cancel one another out; only within the narrow range $-l/c < \tau < 0$ is the slope positive

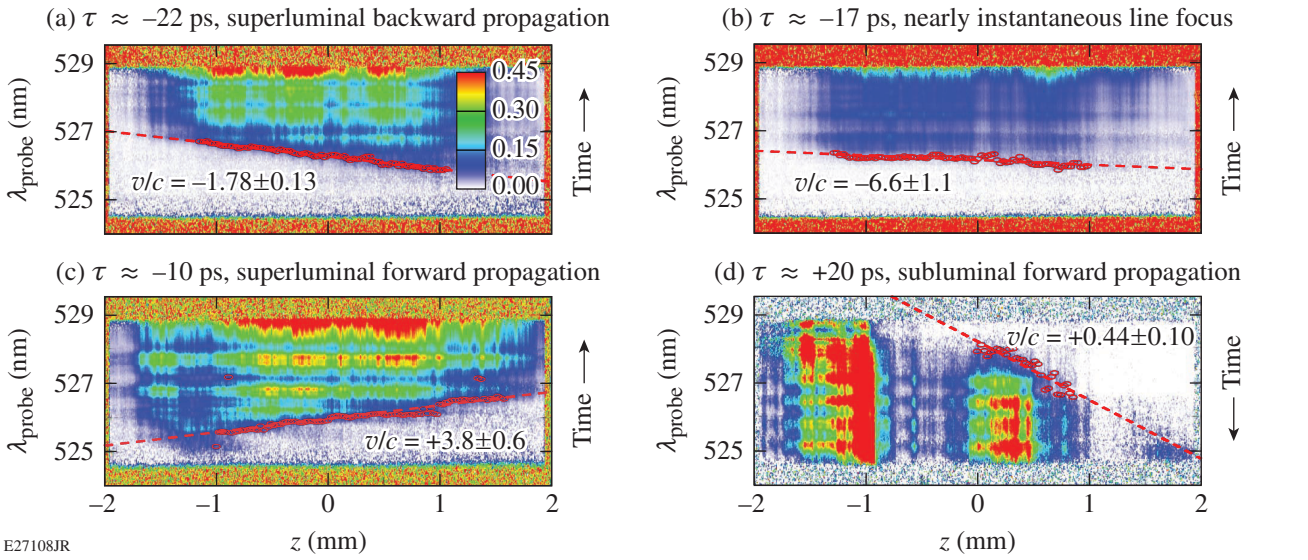

Figure 154.19
Spectrally resolved schlieren results. (a) An example of superluminal backward propagation for $\tau \approx -22$ ps. The probe is negatively chirped so the direction of time is from the blue end to the red end of the spectrum. The IWAV begins at $+z$ and propagates backward to $-z$ along the pump axis. (b) A more highly superluminal example producing a nearly instantaneous line focus. (c) With $-l/c < \tau < 0$, the IWAV remains superluminal but switches to forward-propagating, reversing the sign of the slope. (d) When the probe is positively chirped, the direction of time is effectively reversed, and subluminal forward propagation produces a disjointed plasma channel because of ionization-induced refraction.

because the IWAV's are forward-propagating but the probe chirp is negative [e.g., Fig. 154.19(c)]. The reversed direction of time is evident in the schlieren image because the blue side of the spectrum probes the fully formed plasma channels in contrast to the previous examples. Note also that for $\tau > -l/(2c)$, the time v_f/l that it takes the IWAV to propagate from one edge of the focal region to the other is greater than the probe pulse duration $|\tau|$, limiting the IWAV propagation distance that the probe can diagnose. Therefore, in the example shown, the plasma is already over 1 mm in length by the time the probe arrives.

The key difference in Fig. 154.19(d) is that the schlieren signal appears disjointed along the axis of the pump beam. This results from ionization-induced refraction in the case of subluminal forward propagation—an effect that was predicted in Ref. 22. To illustrate this more clearly, 2-D shadowgraphs and 2-D schlieren images are shown for three cases in Fig. 154.20. The example in Fig. 154.20(a) happens to be the case of a nearly instantaneous line focus, but all cases of backward propagation that were tested, in addition to superluminal forward propagation, produced similar long, uniform plasma channels. Contrast that with Fig. 154.20(b), which shows that the initial plasma at $z = -1$ mm disrupts subsequent plasma formation over the next ≈1 mm. At a later point along the pump axis, the initial plasma is far enough away (refracting a small enough fraction of the wavelength that focuses to that location) that ionization is once again triggered locally. This cycle repeats itself once more, producing three distinct sparks [the third being more evident in Fig. 154.19(d) than in Fig. 154.20(b)].

Using the edge-finding routine on the middle spark resulted in a linear fit that roughly tracks the central plasma and also seems to predict the timing of the third plasma's formation, but the fit's confidence was much lower, resulting in larger error bars. The slopes for all data sets, including subluminal backward propagation (which has not been shown), were overplotted with the analytic calculation in Fig. 154.18(b). In most cases, the uncertainties in pulse length and schlieren slope were smaller than the marker size shown, with the exception of the subluminal forward-propagating IWAV just described; nevertheless, that result is also in good agreement with the prediction.

For completeness, Fig. 154.20(c) shows the plasma channel formation that occurs when the probe duration was at best compression ($\tau \approx 500$ fs). In this case, the diffractive lens produces a distributed focal spot that would be expected to have approximately constant intensity over several millimeters

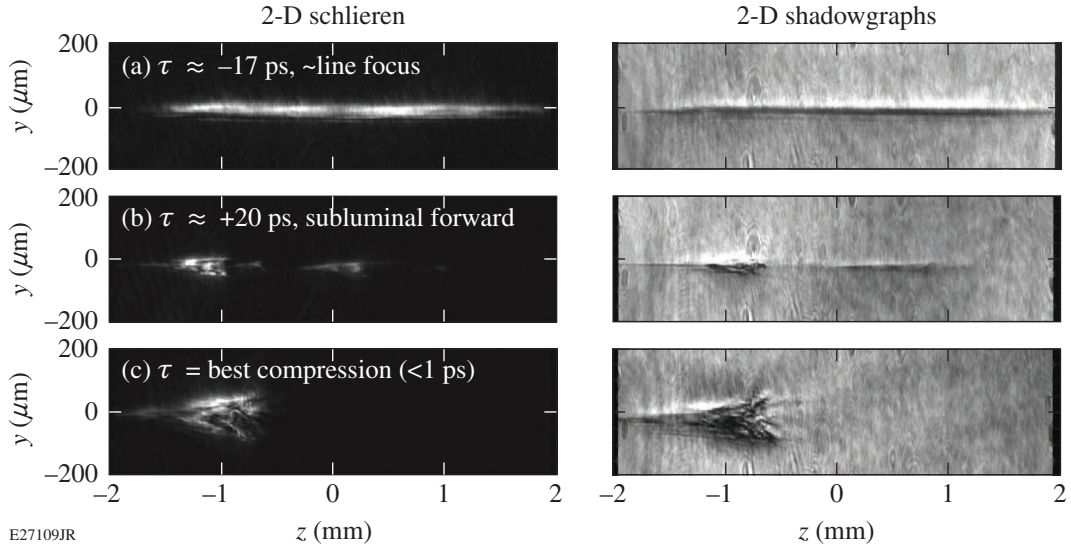

Figure 154.20
Two-dimensional schlieren and shadowgraphy of various cases. (a) The $\tau \approx -17$-ps example shows a long, uniform plasma channel and is representative of all tested cases of backward propagation as well as superluminal forward propagation. (b) Subluminal forward propagation leads to plasma channel breakup because of ionization-induced refraction; (c) this also occurs for best compression, which is most similar to conventional beam propagation in that laser intensity moves forward at the group velocity.

while propagating at the laser's group velocity (and is therefore the case most similar to conventional beam propagation). This case was degraded even more severely by ionization-induced refraction such that only one short plasma was formed.

In summary, ionization waves of arbitrary velocity have been demonstrated experimentally using the flying focus. While superluminal ionization front propagation has been demonstrated previously,[25] and a different (more complicated) scheme for tuning the velocity of ionization waves has been proposed,[26] to our knowledge this represents the first experimental demonstration of IWAV's. Producing plasma channels in this manner could facilitate improved performance in a wide range of applications that rely on synchronization with an ionization front, such as plasma-based laser amplification, photon acceleration, and THz generation. Even neglecting the potentially beneficial dynamics of the ionization front, we have demonstrated long, uniform, flying focus-produced plasma channels that are comparable to those created using an axicon lens, which may be of interest to applications that utilize plasma waveguides.[27–30]

ACKNOWLEDGMENT

This work was supported by the U.S. Department of Energy Office of Fusion Energy Sciences under contract No. DE-SC0016253, Department of Energy under Cooperative Agreement No. DE-NA0001944, the University of Rochester, and the New York State Energy Research and Development Authority. The support of DOE does not constitute an endorsement by DOE of the views expressed in this article.

REFERENCES

1. C. Thaury *et al*., Nat. Phys. **3**, 424 (2007).
2. P. Michel *et al*., Phys. Rev. Lett. **113**, 205001 (2014).
3. D. Turnbull, P. Michel, T. Chapman, E. Tubman, B. B Pollock, C. Y Chen, C. Goyon, J. S Ross, L. Divol, N. Woolsey, and J. D Moody, Phys. Rev. Lett. **116**, 205001 (2016).
4. D. J. Stark *et al*., Phys. Rev. Lett. **115**, 025002 (2015).
5. D. Turnbull, C. Goyon, G. E. Kemp, B. B. Pollock, D. Mariscal, L. Divol, J. S. Ross, S. Patankar, J. D. Moody, and P. Michel, Phys. Rev. Lett. **118**, 015001 (2017).
6. K. Qu, Q. Jia, and N. J. Fisch, Phys. Rev. E **96**, 053207 (2017).
7. M. R. Edwards and J. M. Mikhailova, Phys. Rev. Lett. **117**, 125001 (2016).
8. M. R. Edwards, J. M. Mikhailova, and N. J. Fisch, Phys. Rev. E **96**, 023209 (2017).
9. C. D'Amico *et al*., Phys. Rev. Lett. **98**, 235002 (2007).
10. K. Y. Kim *et al*., Opt. Express **15**, 4577 (2007).
11. G. Shvets *et al*., Phys. Rev. Lett. **81**, 4879 (1998).
12. L. Lancia *et al*., Phys. Rev. Lett. **116**, 075001 (2016).
13. R. K. Kirkwood, D. P. Turnbull, T. Chapman, S. C. Wilks, M. D. Rosen, R. A. London, L. A. Pickworth, W. H. Dunlop, J. D. Moody, D. J. Strozzi, P. A. Michel, L. Divol, O. L. Landen, B. J. MacGowan, B. M. Van Wonterghem, K. B. Fournier, and B. E. Blue, Nat. Phys. **14**, 80 (2018).
14. V. M. Malkin, G. Shvets, and N. J. Fisch, Phys. Rev. Lett. **82**, 4448 (1999).
15. W. B. Mori, Phys. Rev. A **44**, 5118 (1991).
16. E. Esarey, G. Joyce, and P. Sprangle, Phys. Rev. A **44**, 3908 (1991).
17. P. Sprangle and E. Esarey, Phys. Fluids B **4**, 2241 (1992).
18. J. M. Dias *et al*., Phys. Rev. Lett. **78**, 4773 (1997).
19. D. Turnbull, S. Bucht, A. Davies, D. Haberberger, T. Kessler, J. L. Shaw, and D. H. Froula, Phys. Rev. Lett. **120**, 024801 (2018).
20. A. Sainte-Marie, O. Gobert, and F. Quéré, Optica **4**, 1298 (2017).
21. D. H. Froula, D. Turnbull, A. S. Davies, T. J. Kessler, D. Haberberger, J. P. Palastro, S.-W. Bahk, I. A. Begishev, R. Boni, S. Bucht, J. Katz, and J. L. Shaw, "Spatiotemporal Control of Laser Intensity," to be published in Nature Photonics.
22. J. P. Palastro, D. Turnbull, S.-W. Bahk, R. K. Follett, J. L. Shaw, D. Haberberger, J. Bromage, and D. H. Froula, Phys. Rev. A **97**, 033835 (2018).
23. W. P. Leemans *et al*., Phys. Rev. A **46**, 1091 (1992).
24. T. M. Antonsen, Jr. and Z. Bian, Phys. Rev. Lett. **82**, 3617 (1999).
25. I. Alexeev, K. Y. Kim, and H. M. Milchberg, Phys. Rev. Lett. **88**, 073901 (2002).
26. A. Zhidkov *et al*., Phys. Rev. Lett. **103**, 215003 (2009).
27. C. G. Durfee and H. M. Milchberg, Phys. Rev. Lett. **71**, 2409 (1993).
28. P. Volfbeyn, E. Esarey, and W. P. Leemans, Phys. Plasmas **6**, 2269 (1999).
29. Y.-F. Xiao *et al*., Phys. Plasmas **11**, L21 (2004).
30. S. Z. Green *et al*., Plasma Phys. Control. Fusion **56**, 084011 (2014).

The Single-Line-of-Sight, Time-Resolved X-Ray Imager Diagnostic on OMEGA

Introduction

Time-resolved x-ray imaging of the self-emission from a hot spot formed in implosions of cryogenic deuterium–tritium (DT) shells in inertial confinement fusion experiments provides critical information for inferring the hot-spot pressure.[1] A 16-channel, framing-camera–based, time-resolved Kirkpatrick–Baez x-ray microscope (KBframed)[2] is routinely used to measure the evolution of the stagnation region of imploded cryogenic targets on the University of Rochester's OMEGA Laser System.[3] The high spatial (~6-μm) and temporal (~40-ps) resolutions of this system make it possible to accurately determine the core emission size and shape at the peak of stagnation. The hot spot in OMEGA implosions typically has a radius of ~20 to 30 μm, and the core x-ray emission lasts for ~100 ps (Ref. 2). Measurements of the core size, ion temperature, neutron-production temporal width, and neutron yield provide the input to infer the hot-spot pressure, which currently exceeds 50 Gbar in OMEGA implosions.[1] Multiple-lines-of-sight imaging will provide information about the hot-spot morphology and improve the confidence in the measurement of its size. This is important to better understand the physics that currently limits the hot-spot pressure. The new diagnostics will contribute to strategies to improve the implosion performance so that pressures are reached that will scale to ignition-relevant implosions. With the achievable target compression on OMEGA, the optimum photon-energy range for imaging the hot spot is 4 to 8 keV, where the shell is optically thin to this radiation. This article discusses a novel time-gated, x-ray imager that was installed on OMEGA almost perpendicular to the existing KBframed diagnostic: the single-line-of-sight, time-resolved x-ray imager (SLOS-TRXI). SLOS-TRXI is the product of a joint project with General Atomics (GA), Sandia National Laboratories (SNL), Kentech Instruments, Lawrence Livermore National Laboratory (LLNL), and the Laboratory for Laser Energetics (LLE). It comprises a new generation of fast-gated x-ray framing camera that is capable of capturing multiple frames along a single line of sight with ~40-ps temporal resolution and high spatial resolution. It captures x-ray images of the core of an imploded target during high-energy-density (HED) physics experiments for analysis.

Figure 154.21 shows a schematic of SLOS-TRXI in its initial configuration. The x-ray–emitting hot spot is imaged with a pinhole onto a photocathode through several foil filters that protect the diagnostic from target debris, optical emission, and contamination. A fraction of the photons is absorbed in the photocathode, producing secondary photoelectrons. The photoelectron image is then imaged with 1:1 magnification through a 75-cm-long drift tube containing a homogenous magnetic field of 6 kG onto a nanosecond-gated, burst-mode, hybrid complementary metal-oxide semiconductor (hCMOS) sensor developed by SNL.[4] SLOS-TRXI uses the radiation-tolerant system Icarus I1G6 (Ref. 5), which was developed for the National Ignition Facility (NIF).[6] The novel aspect is to combine the electron pulse-dilation imager technique[7,8] developed by GA and LLNL with a nanosecond-gated hCMOS sensor. A temporally varying voltage is applied between the photocathode and a grid that accelerates the photoelectrons to a speed that depends on the time when they are produced by the x rays. The kinetic energy of early photoelectrons is higher than that of later electrons. The long drift tube stretches the electron pulse by a factor of ~70 in time because of the different times of flight. The electrons are then directly detected with the gated hCMOS sensor. The pulse-dilatation technique makes it possible to achieve ~40-ps time resolution with 2-ns gating in

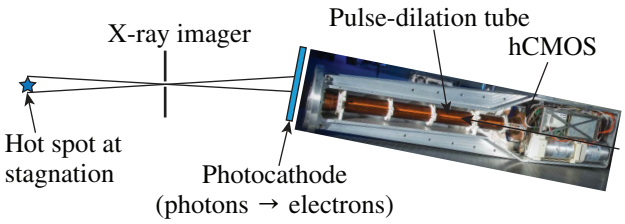

Figure 154.21
Schematic of the single-line-of-sight, time-resolved x-ray imager on OMEGA in its initial configuration. A pinhole is used to image the x rays from the hot spot onto a photocathode. A pulse-dilation tube stretches the secondary electron pulse in time and forms an image of the hot spot on a time-gated, solid-state detector (hCMOS). The pinhole will later be replaced with an advanced optic to provide improved spatial resolution.

the hCMOS. Efforts are underway to develop an hCMOS sensor with ~1-ns gating time, which then would improve the time resolution to ~20 ps using the same time magnification. The combination of these two transformative technologies leads to a new class of radiation-hardened x-ray imagers that will have a significant impact in HED diagnostic applications requiring high temporal and spatial resolutions on the NIF,[6] Sandia's Z machine,[9] and OMEGA.[3]

Mechanical Design of the Pinhole Imager

Figure 154.22 shows a computer-aided design (CAD) model of the front part of SLOS-TRXI. The snout comprises a pinhole-array imager casting multiple images of the hot spot onto the detector. The pinhole array with 10-μm-diam holes is placed 166.5 mm from target chamber center (TCC), where the imploding target is located. The pinhole array is sandwiched between two 500-μm-thick Ta collimators with 150-μm-diam holes and is protected from target debris by a 254-μm-thick Be-foil blast shield. The hole spacing in the collimators and the pinhole array is 238±5 μm in the vertical and 381±5 μm in the horizontal directions. Collimators and the pinhole array are mounted in a spring-loaded nose cap, which can be easily changed during a vacuum chamber entry. A second 254-μm-thick Be foil between the snout and the extension tube serves as a vacuum window and separates the clean, high vacuum on the detector side from the target chamber vacuum. The CsI photocathode is located 2238 mm from TCC, providing a spatial magnification of 12.4. A tungsten aperture is located 1904 mm from TCC to reduce background from scattered radiation. An image plate with a rectangular opening can be placed in front of the aperture to obtain additional time-integrated pinhole images of the implosion. The spatial magnification for the images on the image plate is 10.4. A gate valve is placed between the two vacuum spools, allowing one to change the image plate between shots without breaking the vacuum in the drift tube. The drift tube is tilted by 4° in the vertical direction, thereby moving the hCMOS sensor out of the direct line of sight of radiation from the target. The main reason for this adjustment is to prevent neutron-induced background in high-yield shots from compromising the signal. Two 100-mm-thick blocks of polyethylene, each encapsulated in a stainless-steel case, were placed in the direct line of sight to reduce the neutron flux on the hCMOS sensor.

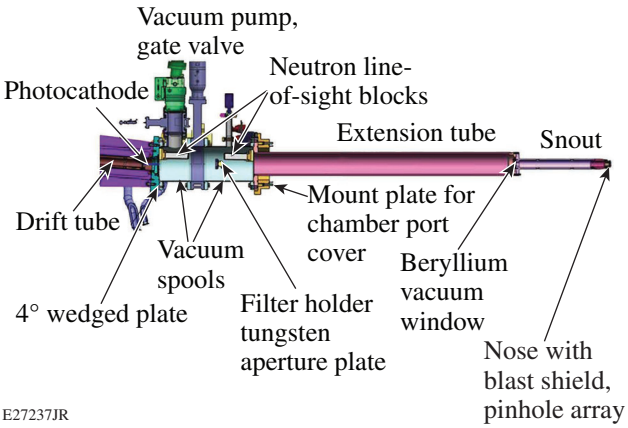

Figure 154.22
CAD model of the pinhole imager that produces an x-ray image on the photocathode of SLOS-TRXI.

SLOS-TRXI is installed in the H4F port (polar angle of 45.2° and azimuthal angle of 234°) of the OMEGA target chamber. Figure 154.23 shows the installation of the diagnostic on OMEGA. The x-ray imager, located inside the target chamber, is not visible. The long aluminum housing contains the pulse dilation tube, the hCMOS detector, and various electronic components.

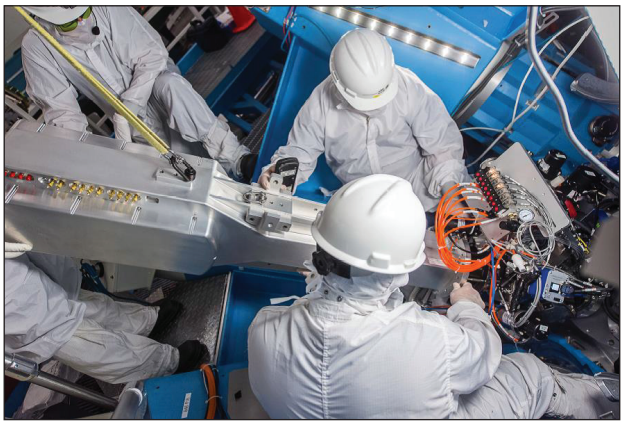

Figure 154.23
Installation of the SLOS-TRXI diagnostic on the OMEGA target chamber.

Figure 154.24 shows the calculated point-spread function (PSF) of the diagnostic (solid blue curve) in the target plane, which was obtained by convolving the pinhole imager PSF (dotted green curve) with the detector PSF (dashed red curve). The pinhole PSF was calculated for a pinhole diameter of 10 μm using the Fresnel approximation and spectrally averaging over the calculated spectral response for a cryogenic target implosion on OMEGA (see Fig. 154.27, p. 84). The detector PSF was assumed to be of Gaussian shape with a full width at half maximum (FWHM) of 40 μm in the image plane based on the Larmor radius of the electrons in the magnetic field inside the drift tube and a pixel size of 25 μm in the hCMOS

sensor. The corresponding detector width in the target plane is 3.2 μm by taking the spatial magnification into account. The calculated FWHM of the convolved diagnostic PSF is 5.0 μm and the full width at the 20% point is 8.4 μm. The two vertical dashed lines mark the 10.7-μm calculated spatial resolution of the pinholes from geometrical optics. Dedicated shots that will measure the spatial resolution of the diagnostic are planned.

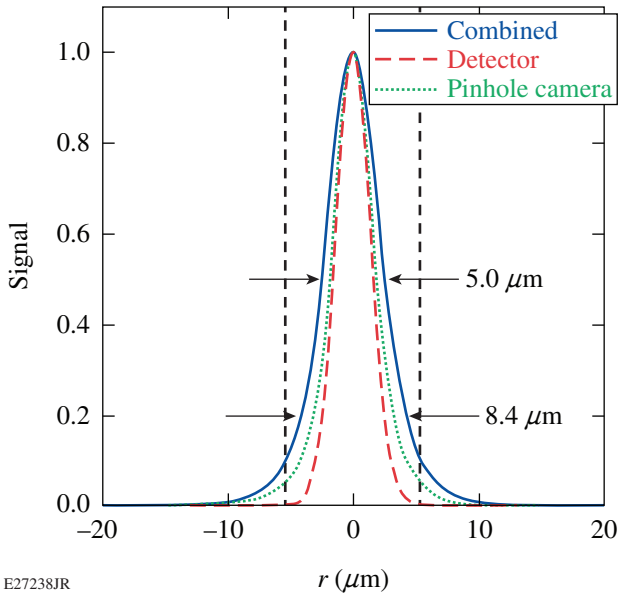

Figure 154.24
Calculated point-spread function (PSF) of the pinhole imager (dotted green curve), the detector PSF (dashed red curve), and the combined PSF (solid blue curve).

The pinhole imager will be replaced later in phase II with an advanced optic to provide improved spatial resolution.

Drift Tube and Hybrid Complementary Metal-Oxide Semiconductor Detector

Figure 154.25(a) shows the back part of SLOS-TRXI on a test bench with the solenoid-wound drift tube and hCMOS sensor at the right end, installed in their aluminum housing. The inside of the drift tube and the sensor are at vacuum; the electronics and the case are in air. The electronics include a magnet pulser, capacitors, and a photocathode pulser that are stored in the back of the aluminum case (not shown in the figure). Two energy storage capacitors generate a 6-kG magnetic field at the photocathode. Figure 154.25(b) shows a schematic of the hCMOS sensor and its timing. The sensor is comprised of 1024 × 512 pixels with a size of 25 μm × 25 μm, providing a total detector area of 25.6 mm × 12.8 mm. It is split into two halves (hemisphere A and hemisphere B) that can be independently gated to provide continuous temporal coverage. The reading sequence is frame 1 (A,B) and frame 2 (A,B). The schematic shows how each hemisphere is timed. The black time axis corresponds to time at the hCMOS detector, which shows that each hemisphere is alternatively read out with an integration time of 2 ns and a 2-ns delay between hemispheres, providing a total of four snapshots. The red time axis is the effective instrument time at the target plane when taking the time magnification of the pulse-dilation drift tube into account. The available time range covers ~120 ps. Each hemisphere provides a sufficient area to accommodate multiple

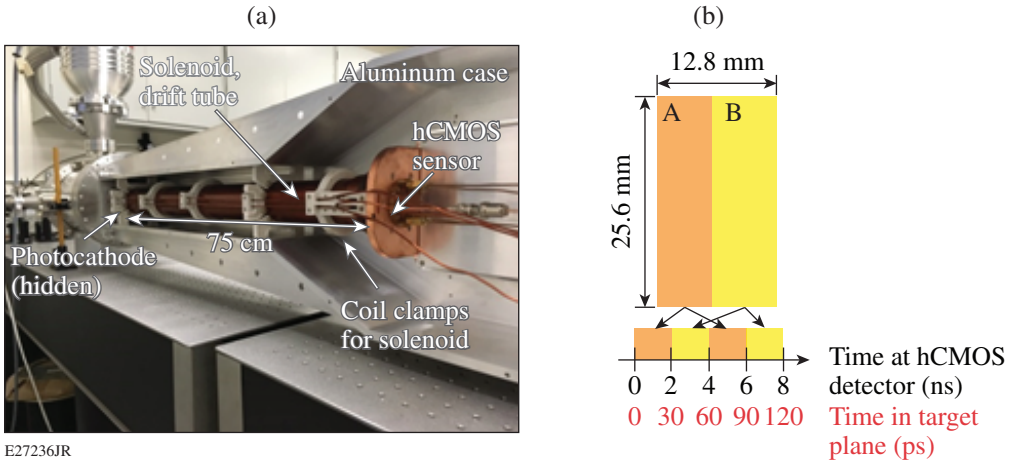

Figure 154.25
(a) Photograph of the solenoid with a drift tube and hCMOS sensor installed in the aluminum case. The camera is mounted on a test bench for testing. The space on the right is for electronics that include a magnet pulser, capacitors, and a photocathode pulser (not shown). (b) Schematic of the timing of the hCMOS sensor. The black time axis corresponds to time at the hCMOS detector, while the red time axis corresponds to time at the target plane for maximum time magnification because of the pulse dilation in the drift tube.

images of the hot spot. The images of each hemisphere that are simultaneously read out can then be added up to improve signal fidelity and signal-to-noise ratio. Another possibility is to apply different filtration across different regions of the sensor to obtain hot-spot images for different photon-energy ranges and to improve the dynamic range.

The temporal resolution and gate profiles of SLOS-TRXI were measured using a pulsed UV laser with a pulse duration of 21-ps FWHM and a wavelength of 266 nm. The laser beam was focused to a single 1-mm-diam FWHM spot onto the photocathode, and an image formed in the center of one of the hCMOS hemispheres. Separate scans for each hemisphere were obtained by shifting the laser spot on the other hemisphere. The gate-width scan consists of 100 image captures as the relative timing of the laser pulse and the SLOS-TRXI gate was varied in 2-ps steps. The system's trigger jitter was ~25 ps. A fast oscilloscope measured simultaneously the monitor pulse from the photocathode and the laser pulse to remove the jitter and to obtain high-fidelity temporal profiles. The laser pulse width and the detector gate width are about the same so deconvolution was needed to infer true gate width. Gate-width scans were taken at various laser intensities to measure space-charge broadening of the electron pulse. Figure 154.26 depicts the measured effective gate profiles. The sensor was operated in (2,2) mode with a delay of 2 ns and the drift tube at nominal 80× temporal magnification, which is currently the fastest performance mode for SLOS-TRXI with the Icarus 1 sensor.

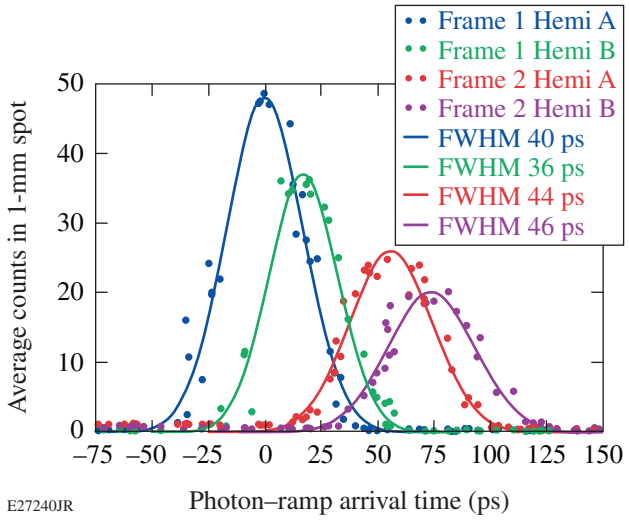

Figure 154.26
Measured gate profiles of the four frames in (2,2) mode with a delay of ~2 ns and nominal 80× temporal magnification. The gate width varies from 36 to 46 ps.

The frame-to-frame amplitude decay is caused by an electron energy drop during ramp and a lower detection efficiency of the hCMOS for lower-kinetic-energy photoelectrons produced later in time. The laser intensity was chosen to give 20% space-charge broadening of the electron pulse in frame 1, which effectively lowers the temporal magnification from nominally 80× to ~70×. The solid curves are fits with a Gaussian-shaped curve to the data and the corresponding FWHM's are given in the legend. The effective gate FWHM varies from 36 to 46 ps and the sensitivity drops by about a factor of 2. The system operation is quite stable. Space-charge broadening increased with the laser intensity, which resulted in longer gate widths. Further details on the electron detection by the hCMOS sensor and the drift-tube design, its operation, and characterization can be found in Ref. 10.

Activation Shots on OMEGA

A series of activation shots were taken, and the diagnostic was used for the first time on cryogenic target implosions in September 2017. In its initial phase, the imaging concept was tested under the high background from neutrons and hard x rays in OMEGA cryogenic target implosions. The experiment used 60 UV (λ = 351 nm) beams from the OMEGA laser[3] with an energy of up to 28 kJ. The diagnostic has been successfully activated with (1) flat-foil shots with dedicated beams, (2) room-temperature exploding-pusher implosions of thin glass shells with various fills (DT and D_2 with Ar dopant),[11] and (3) cryogenic implosions with 42-μm-thick DT ice targets providing neutron yields of up to ~1×10^{14} (Ref. 12). Coarse timing within ~200 ps was achieved in the first campaign at lower temporal resolution (~250 ps). Fine timing within ~50 ps was achieved in the second and third campaigns with higher temporal resolution (~40 ps). Figure 154.27 shows the detected spectrum of SLOS-TRXI for an OMEGA cryogenic target implosion from a photometric calculation. The calculation used the spectrum from a 1-D hydrodynamic simulation (obtained with the code *LILAC*[13]) of a cryogenic target, the solid angle of the pinhole imager, an integration time of 30 ps, the transmission through 508 μm of Be, 51 μm of Kapton (the photocathode substrate), and an additional 12 μm of Cu that had to be inserted to reduce the signal level in the cryogenic shots. The calculation also considers the photon absorption in the 200-nm-thick CsI photocathode layer. The detected spectrum ranges from 4 to 9 keV and peaks at 6 keV.

Figure 154.28 shows the core emission from cryogenic target implosion shot 87024. The instrument recorded the hot-spot x-ray emission in the photon energy range from ~4 to 9 keV in four frames. Each frame was integrated over ~40 ps and

the frame-to-frame delay time was ~25 ps. Up to eight pinhole images were averaged for each frame to improve the signal fidelity. The bang time was in the fourth frame showing the smallest object. The data show that shots with neutron yields of up to 1×10^{14} produced no neutron-induced background in the hCMOS. Space-charge effects currently dictate that the signal level of the instrument is kept below 100 counts per pixel. With a noise floor of one count per pixel, this limits the dynamic range to two orders of magnitude.

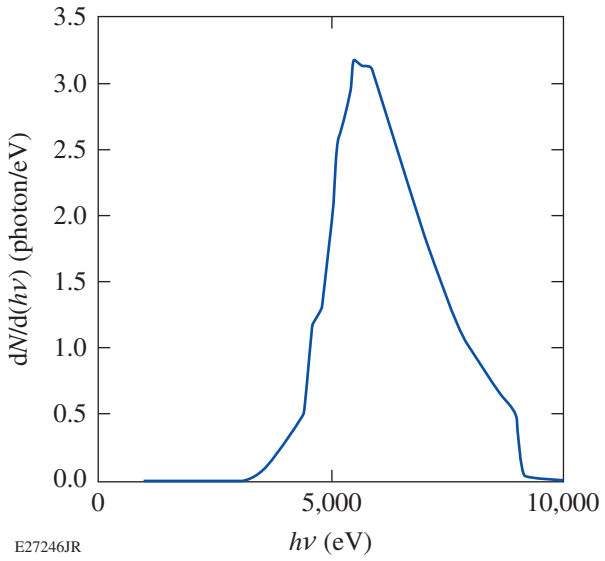

Figure 154.27
Detected spectrum of SLOS-TRXI for an OMEGA cryogenic target implosion from a photometric calculation.

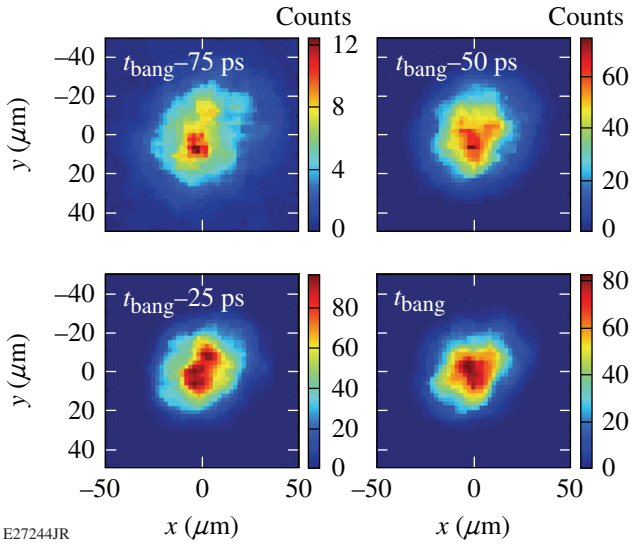

Figure 154.28
Four frames of the hot-spot x-ray emission (~4 to 9 keV) were recorded in cryo shot 87024 with the bang time in the fourth frame. For each frame multiple pinhole images were averaged in order to improve the signal fidelity.

The pattern from the pinhole array provides an *in-situ* measure for the image magnification. Eddy currents in the aluminum case surrounding the drift tube cause a slight anamorphic demagnification when imaging the photoelectrons from photocathode to hCMOS. The design magnification of 12.4× is slightly reduced to 11.9× in the vertical and 11.4× in the horizontal direction. The images were warp corrected by rotating and scaling in x and y to minimize residual error between fitted centroids of each image and the pinhole array centers. The drift tube contains three grids with a period of 230 μm. The grid structure becomes visible in the hot-spot image at high signal levels, which affects to some extent the quality of a single pinhole image and the signal-to-noise ratio. The grid structure averages out when overlapping multiple pinhole images. In the future this will be mitigated by using grids with a larger period so there is less interference with the spatial structures that are imaged.

Conclusions

The single-line-of-sight, time-resolved x-ray imager (SLOS-TRXI) has been activated on OMEGA to provide time-resolved images of the core of imploded cryogenic deuterium–tritium shells in inertial confinement fusion experiments. Activation shots with neutron yields of up to 1×10^{14} produced background-free images of the imploded core in four frames. In phase II, the diagnostic will be further developed to improve the spatial resolution, add additional frames, achieve a higher space-charge operating limit, and provide better temporal resolution. Advanced x-ray optical systems that are under consideration include a Kirkpatrick–Baez optic, a Wolter-like optic, and penumbral imaging.

ACKNOWLEDGMENT

This work was supported by the DOE NNSA under awards No. DE-NA0001944 and DE-FC02-04ER54789, the Laboratory Basic Science Program, the University of Rochester, and the New York State Energy Research and Development Authority.

REFERENCES

1. S. P. Regan, V. N. Goncharov, I. V. Igumenshchev, T. C. Sangster, R. Betti, A. Bose, T. R. Boehly, M. J. Bonino, E. M. Campbell, D. Cao, T. J. B. Collins, R. S. Craxton, A. K. Davis, J. A. Delettrez, D. H. Edgell, R. Epstein, C. J. Forrest, J. A. Frenje, D. H. Froula, M. Gatu Johnson, V. Yu. Glebov, D. R. Harding, M. Hohenberger, S. X. Hu, D. Jacobs-

Perkins, R. T. Janezic, M. Karasik, R. L. Keck, J. H. Kelly, T. J. Kessler, J. P. Knauer, T. Z. Kosc, S. J. Loucks, J. A. Marozas, F. J. Marshall, R. L. McCrory, P. W. McKenty, D. D. Meyerhofer, D. T. Michel, J. F. Myatt, S. P. Obenschain, R. D. Petrasso, R. B. Radha, B. Rice, M. Rosenberg, A. J. Schmitt, M. J. Schmitt, W. Seka, W. T. Shmayda, M. J. Shoup III, A. Shvydky, S. Skupsky, A. A. Solodov, C. Stoeckl, W. Theobald, J. Ulreich, M. D. Wittman, K. M. Woo, B. Yaakobi, and J. D. Zuegel, Phys. Rev. Lett. **117**, 025001 (2016); **117**, 059903(E) (2016).

2. F. J. Marshall, R. E. Bahr, V. N. Goncharov, V. Yu. Glebov, B. Peng, S. P. Regan, T. C. Sangster, and C. Stoeckl, Rev. Sci. Instrum. **88**, 093702 (2017).

3. T. R. Boehly, D. L. Brown, R. S. Craxton, R. L. Keck, J. P. Knauer, J. H. Kelly, T. J. Kessler, S. A. Kumpan, S. J. Loucks, S. A. Letzring, F. J. Marshall, R. L. McCrory, S. F. B. Morse, W. Seka, J. M. Soures, and C. P. Verdon, Opt. Commun. **133**, 495 (1997).

4. L. Claus, *et al*., Proc. SPIE **9591**, 95910P (2015).

5. A. C. Carpenter *et al*., Proc. SPIE **9966**, 99660H (2016).

6. E. M. Campbell and W. J. Hogan, Plasma Phys. Control. Fusion **41**, B39 (1999).

7. R. D. Prosser, J. Phys. E: Sci. Instrum. **9**, 57 (1976).

8. T. J. Hilsabeck *et al*., Rev. Sci. Instrum. **81**, 10E317 (2010).

9. R. B. Spielman, W. A. Stygar, J. F. Seamen, F. Long, H. Ives, R. Garcia, T. Wagoner, R. W. Struve, M. Mostrom, I. Smith, D. Spence, and P. Corcoran, in *11th IEEE International Pulsed Power Conference*, edited by G. Cooperstein and I. Vitkovitsky (IEEE, Piscataway, NJ, 1997), Vol. 1, pp. 709–714.

10. K. Engelhorn, T. J. Hilsabeck, J. D. Kilkenny, D. Morris, T. M. Chung, A. K. L. Dymoke-Bradshaw, J. D. Hares, P. Bell, D. Bradley, A. C. Carpenter, M. Dayton, S. R. Nagel, L. Claus, J. Porter, G. Rochau, M. Sanchez, S. P. Regan, C. Sorce, and W. Theobald, "Subnanosecond Single Line-of-Sight X-Ray Imagers," submitted to Review of Scientific Instruments.

11. M. J. Rosenberg, H. G. Rinderknecht, N. M. Hoffman, P. A. Amendt, S. Atzeni, A. B. Zylstra, C. K. Li, F. H. Séguin, H. Sio, M. Gatu Johnson, J. A. Frenje, R. D. Petrasso, V. Yu. Glebov, C. Stoeckl, W. Seka, F. J. Marshall, J. A. Delettrez, T. C. Sangster, R. Betti, V. N. Goncharov, D. D. Meyerhofer, S. Skupsky, C. Bellei, J. Pino, S. C. Wilks, G. Kagan, K. Molvig, and A. Nikroo, Phys. Rev. Lett. **112**, 185001 (2014).

12. R. Betti, J. P. Knauer, V. Gopalaswamy, D. Patel, K. M. Woo, K. S. Anderson, A. Bose, A. R. Christopherson, V. Yu. Glebov, F. J. Marshall, S. P. Regan, P. B. Radha, C. Stoeckl, and E. M. Campbell, Bull. Am. Phys. Soc. **62**, BAPS.2017.DPP.TI2.1 (2017).

13. J. Delettrez, R. Epstein, M. C. Richardson, P. A. Jaanimagi, and B. L. Henke, Phys. Rev. A **36**, 3926 (1987).

Supersonic Gas-Jet Characterization with Interferometry and Thomson Scattering on the OMEGA Laser System

Introduction

The generation of long, uniform plasmas is important to many disciplines in the laser–plasma interaction field. These plasmas are used in the study of laser–plasma instabilities relevant to inertial confinement fusion (ICF)[1] and the development of compact particle acceleration methods such as wakefield acceleration.[2] Supersonic gas-jet targets provide several advantages over comparable targets. Supersonic gas jets have excellent density profiles with steep gradients at the edges and consistent uniform densities in the central regions. This density profile is important for applications where propagation distance through the gas or plasma medium must be minimized before the laser beam reaches the experimental volume.

A wide range of plasma density regimes become accessible by modifying the backing pressure in the jet reservoir. The nozzle geometry can be modified to provide shaping and tuning of the gas-jet profile to experimental requirements. These features make the gas jet a versatile target. Other comparable targets, such as gas bags, rely on a solid-density envelope to maintain pressure prior to the experiment, but this outer skin generates blast waves with peak densities significantly greater than the central plateau density.[3]

The gas-jet system on the OMEGA Laser System[4] shown in Fig. 154.29 is a self-contained unit that was deployed from a TIM (ten-inch manipulator). The gas-jet system uses a fast opening and closing electromagnetically controlled valve fitted with a supersonic nozzle.[5] The valve is designed for use at high pressure (~1000 psi) to make possible the generation of high-density jets. The gas supply system enables the use of a wide variety of gases and allows rapid reconfiguration between different experimental demands.

To operate at high pressures, a strong return spring and a high-current electromagnet with a high-energy capacitor bank are used in the valve-control system. The high-energy capacitor bank is housed in a sealed atmospheric bubble at the rear of the apparatus. Together these components make it possible for the valve to be opened in ~100 μs and closed in <500 μs. The rapid opening and closing of this gas jet reduces the contamination of the high-vacuum environment that is required to protect sensitive diagnostic electronics prone to dielectric breakdown.

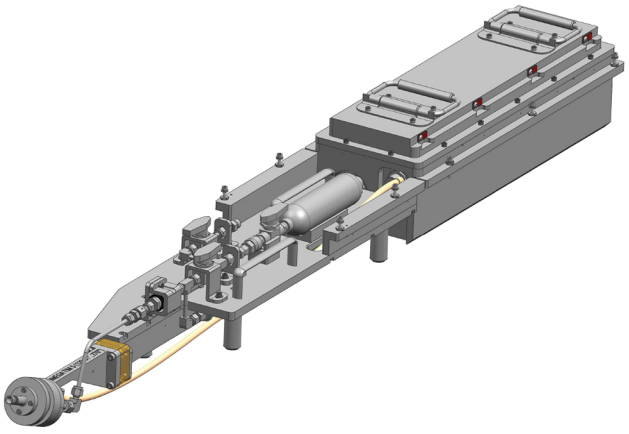
E27023JR

Figure 154.29
A complete engineering drawing of the gas-jet system. The control electronics are housed in the sealed box at the back of the system. The supply cylinder and a system of valves and plumbing feed the gas-jet reservoir. Inside the gas-jet body, an electromagnetic coil actuates a valve to allow the target gas to flow through the supersonic nozzle.

The ability to generate a consistent and well-characterized plasma is important for future laser-plasma experiments. A time-resolved Mach–Zehnder interferometer was used to measure the neutral density throughout the jet. The OMEGA Laser System was used along with the Thomson-scattering system (TSS) diagnostic[6] to measure plasma characteristics. These experimental parameters are then compared to an analytic gas-jet model.

Supersonic Nozzles

A supersonic gas jet generates a flow of gas that is moving with a velocity greater than the local sound speed. The density profile can be predicted using an analytic model of the behavior of a compressible ideal gas moving through the supersonic converging–diverging nozzle geometry.[7] Figure 154.30 shows an example of the converging–diverging supersonic nozzle

design. In this type of nozzle, the flow will accelerate until it reaches the speed of sound:

$$c_s = \sqrt{\frac{\gamma RT}{\mathcal{M}}}, \tag{1}$$

where γ is the adiabatic index, R is the molar gas constant, T is the temperature, and $\mathcal{M}$ is the molar mass. The flow velocity will be equal to the speed of sound at the throat of the nozzle, which is the point at which the cross-sectional area is smallest.

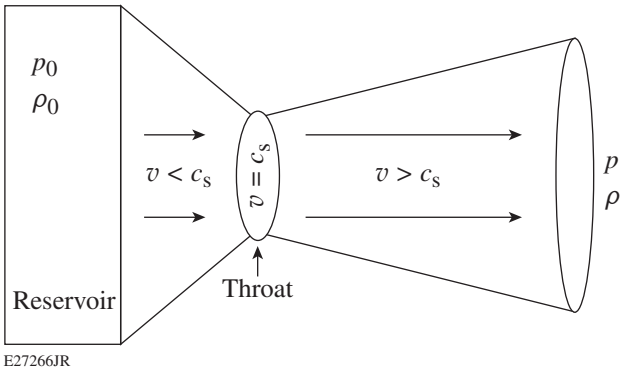

Figure 154.30
A sketch of a converging–diverging nozzle. In the converging section of the nozzle, the flow's velocity is below the speed of sound. The flow velocity will reach the speed of sound and then continue to accelerate past the throat of the nozzle into the diverging section.

As the gas moves from the throat, the gas undergoes isentropic adiabatic expansion in the diverging section of the nozzle, where it accelerates to supersonic velocities. This expansion is characterized by energy conservation,

$$C_p T_0 = \frac{v^2}{2} + C_p T, \tag{2}$$

where C_p is the specific heat of the gas at constant pressure and v is the velocity of the gas. The subscript "0" refers to conditions in the reservoir, while parameters without a subscript refer to conditions at the nozzle exit. Using this conservation equation, one can solve for all thermodynamic properties of the gas flow at all points along the nozzle. In these thermodynamic relations, the most-convenient variable for determining flow properties is the Mach number $\mathrm{M} = v/c_s$, which characterizes the flow velocity as a ratio to the sound speed. Using conservation of energy and solving in terms of the adiabatic index γ and Mach number M,

$$\frac{A}{A_*} = \frac{1}{\mathrm{M}}\left[\frac{2+(\gamma-1)\mathrm{M}^2}{\gamma+1}\right]^{\frac{\gamma+1}{2(\gamma-1)}}, \tag{3}$$

$$\frac{\rho_0}{\rho} = \left(1+\frac{\gamma-1}{2}\mathrm{M}^2\right)^{\frac{1}{\gamma-1}}. \tag{4}$$

Here, ρ_0 is the density in the reservoir, ρ is the density at the nozzle exit, A is the nozzle exit area, and A_* is the nozzle area at the throat. Assuming that gas parameters change smoothly along the entire length of the nozzle, Eq. (4) shows that the density ratio depends only on the Mach number and the adiabatic index of the target gas.

After the gas leaves the nozzle exit, a lineout of the gas density will have a flattop profile with a diameter equal to the nozzle exit diameter and the peak density defined by Eq. (4). Farther away from the nozzle, edges of the profile will be more gradual and expand at an angle approximately equal to 1/M. The full width at half maximum of the gas density can be estimated by

$$D = D_{\mathrm{exit}} + 2\frac{L}{\mathrm{M}}, \tag{5}$$

where D is the plume diameter, D_{exit} is the nozzle exit diameter, and L is the distance from the exit of the nozzle along the nozzle's axis of symmetry. Along with this geometric expansion, there is an accompanying decrease in density. The density in the center of the plume can be related back to the density at the nozzle exit:

$$\rho' = \rho\left(\frac{D_{\mathrm{exit}}}{D_{\mathrm{exit}} + 2\frac{L}{\mathrm{M}}}\right)^2. \tag{6}$$

The complete expression relating the density $\rho'(L)$ to the density in the reservoir ρ is

$$\rho' = \rho_0 \frac{1}{\left(1+\frac{\gamma-1}{2}\mathrm{M}^2\right)^{\frac{1}{\gamma-1}}}\left(\frac{D_{\mathrm{exit}}}{D_{\mathrm{exit}} + 2\frac{L}{\mathrm{M}}}\right)^2. \tag{7}$$

It is important to note that the Mach number of a particular nozzle is a function of the adiabatic index of the gas. For example, a Mach 3 nozzle designed for monatomic gases with $\gamma = 5/3$ will

be a Mach 2.6 nozzle when used with diatomic gases with γ = 7/5. Nozzle configurations for the OMEGA gas-jet system are defined by their monatomic Mach number and their exit diameter, which for a conical nozzle specifies all design parameters.

Nozzles used on the OMEGA gas-jet system are machined from 6061-T6 aluminum. The minimum throat diameter that can be manufactured is 0.25 mm, which is set by tooling aspect-ratio constraints. The maximum throat diameter is 3.6 mm, which is set by the size of the sealing surface that seats against the throat of the nozzle and creates the vacuum seal. These manufacturing constraints place limits on the Mach number and exit diameters of the gas-jet nozzles. Figure 154.31 shows the relationship between the exit diameter and the throat diameter for a range of Mach numbers along with the manufacturing limitations.

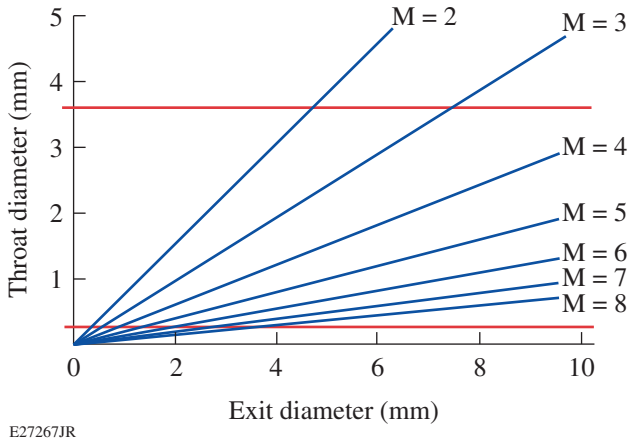

Figure 154.31
A plot of supersonic nozzle throat diameters versus exit diameters for various Mach numbers. Nozzles built for the OMEGA gas jet have a minimum throat diameter of 0.25 mm and a maximum throat diameter of 3.6 mm (shown as horizontal red lines). Mach numbers are calculated for gases with γ = 5/3.

Neutral Gas Density Measurement

The neutral density profile of the gas jet were measured using a Mach–Zehnder interferometer in a vacuum chamber separate from the OMEGA Laser System. In this setup, a 532-nm cw diode laser was expanded and collimated to an ~2-cm beam and split into two legs inside a vacuum chamber, where the probing leg was directed through the gas-jet plume. The image was captured using a PI-MAX3 camera, which uses a fast gate (~10 μs) to resolve the hydrodynamic evolution of the gas-jet plume as the valve opens and closes. The argon gas used in this experiment was chosen for its high index of refraction. To extract the density in the jet from the measured phase shift in the interference pattern, an Abel inversion was performed, which exploits the cylindrical symmetry of the gas plume to measure the density as a function of radius.[8] Figure 154.32(a) shows a measured interferogram and Fig. 154.32(b) the neutral density profile of the gas jet that was extracted from the phase shift using the Abel inversion.

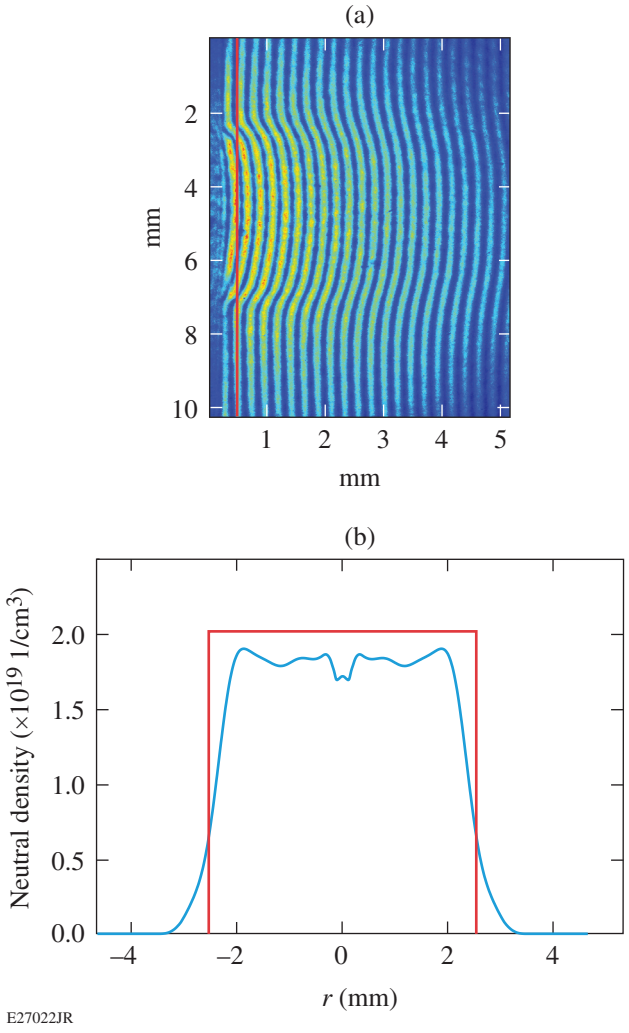

Figure 154.32
(a) An example image of the gas-jet interference pattern measured with the Mach–Zehnder interferometer and (b) a lineout of neutral density versus radius at 0.5 mm away from the nozzle in the gas plume. The flattopped density profile predicted by the analytic model is compared to the measured density profile.

Figure 154.33 shows the density in the gas-jet flow as a function of time. The valve opens in ~100 μs, reaches a steady-state density, and takes ~150 μs to close from a steady-state flow. The time that the gas jet spends in the steady-state flow

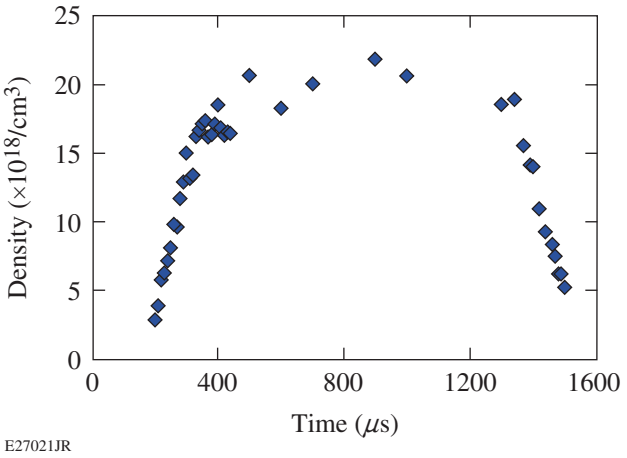

Figure 154.33
Density versus time was measured using a Mach–Zehnder interferometer and a 10-μs gated camera. The gas jet reaches steady state in 150 μs and then closes in a similar amount of time.

regime is dependent on the driving voltage and can range from ~500 μs to ~1 ms.

Plasma Density Measurement

Thomson scattering was used to characterize the conditions in the gas-jet plasma.[9] The OMEGA Thomson-scattering system uses one of the 60 OMEGA beams to provide a Thomson probe beam. The Thomson probe is frequency doubled to 526.5 nm in a 100-ps, square-shaped pulse with 20 J of energy in the *f*/6.7 beam.[10] For beam smoothing and optimal propagation through the plasma volume, a phase plate was used to produce a 200-μm-diam spot at the Thomson volume. Thomson-scattered light was collected along the probe's entire propagation distance through the plasma. An *f*/10 reflective Thomson-scattering collection system makes it possible to achromatically collect and transport the scattered light from the target plasma to a pair of spectrometers and cameras.[6]

To ionize the gas in order to produce a plasma, 11 frequency-tripled, 351-nm beams illuminated a 1-mm-diam spherical volume 1 mm from the end of the gas-jet nozzle. Each heater beam was a 1-ns-long, square-shaped pulse with 300 J per beam, making the total energy on target 3.3 kJ. The Thomson probe was delayed 250 ps compared to the heater pulses. The nozzle was a Mach 2.6 and the target gas was nitrogen.

The imaging Thomson-scattering spectra allow one to analyze the plasma conditions along the entire probe in an ~200-μm-wide channel. Figure 154.34 shows the EPW (electron plasma wave) feature along the Thomson-scattering probe.[11] The EPW feature was used to fit electron density by location of its peak and electron temperature by fitting its width. The flat region of the spectra between ±0.2 mm shows a nearly constant density plateau. The rapidly changing features on either side indicate a dropping density as a result of the rarefaction wave.

When the plasma is first formed, the pressure differential between the inside and outside of the plasma volume creates a rarefaction wave as the plasma expands into the surrounding space. This rarefaction wave is transmitted through the plasma at the ion sound speed $c_s = \sqrt{\gamma Z T_e / m_i}$. Using this velocity, the rarefaction wave takes ~1 ns to reach the center of the plasma volume, which is consistent with its location (200 μm) after 700 ps.

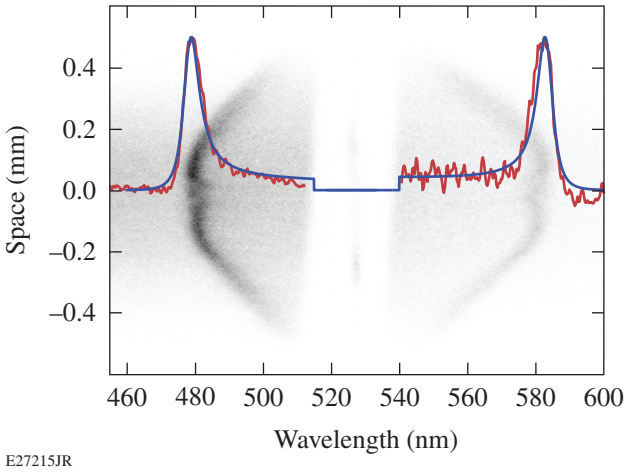

Figure 154.34
Imaging Thomson-scattering electron plasma wave feature of the gas-jet plasma. At the center of the plasma a lineout is taken and a fit is made using the Thomson-scattering form factor. The central portion of the spectrum is removed with a notch filter to remove light near the probe wavelength.

Figure 154.35 shows the density as a function of space through the plasma volume. The density in the central ~500 μm of the plasma is a constant plateau, similar to the measurements shown in Fig. 154.32. The analytic model does not include plasma hydrodynamics and therefore does not match the linear sloping sides of the density profile. The analytic model predicts a peak density ~30% higher than the peak density that is measured with Thomson scattering. In similar experiments this discrepancy between the analytic and experimental peak density was measured to be ~20% to 10%.

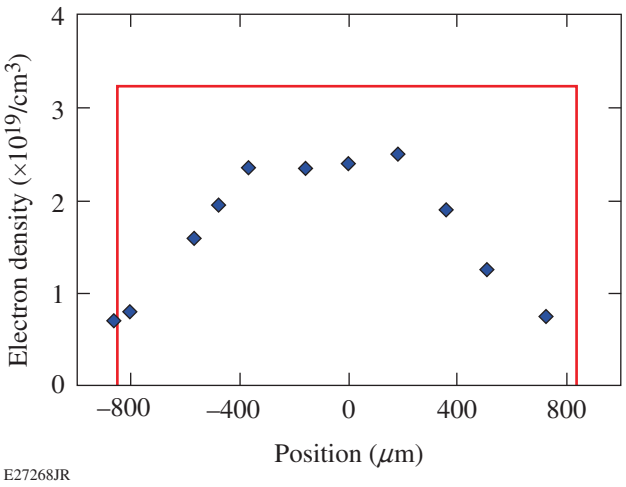

Figure 154.35
Electron density versus position in the gas-jet plasma at 400 ps. A constant density is measured in the central portion of the plasma volume. The outer part of the plasma density drops off linearly because of a rarefaction wave. The analytic model (shown in red) predicts a peak density ~30% higher than the measured peak density. The lower-density fringes of the plasma exceed the predicted bounds of the neutral gas as a result of hydrodynamic expansion in the plasma.

Summary

A gas-jet system has been activated on the OMEGA Laser System. Design considerations for supersonic nozzles and other target parameters have been analyzed in depth using an analytic model for compressible gas flow. The OMEGA gas-jet system has been characterized using a Mach–Zehnder interferometer to study neutral density and timing characteristics. The gas-jet plasma has been characterized using Thomson scattering with the OMEGA laser to measure plasma density across a plasma volume heated by 11 UV beams. In each of these studies the gas jet was found to have excellent characteristics, which will provide a flexible platform for a wide variety of experiments.

ACKNOWLEDGMENT

This material is based upon work supported by the Department of Energy National Nuclear Security Administration under Award Number DE-NA0001944, the University of Rochester, and the New York State Energy Research and Development Authority.

REFERENCES

1. D. Turnbull, C. Goyon, G. E. Kemp, B. B. Pollock, D. Mariscal, L. Divol, J. S. Ross, S. Patankar, J. D. Moody, and P. Michel, Phys. Rev. Lett. **118**, 015001 (2017).
2. A. Döpp *et al*., Rev. Sci. Instrum. **87**, 073505 (2016).
3. D. H. Kalantar *et al*., Phys. Plasma **2**, 3161 (1995).
4. T. R. Boehly, R. S. Craxton, T. H. Hinterman, J. H. Kelly, T. J. Kessler, S. A. Kumpan, S. A. Letzring, R. L. McCrory, S. F. B. Morse, W. Seka, S. Skupsky, J. M. Soures, and C. P. Verdon, Rev. Sci. Instrum. **66**, 508 (1995).
5. M. Krishnan *et al*., Phys. Rev. Spec. Top., Accel. Beams **14**, 033502 (2011).
6. J. Katz, R. Boni, C. Sorce, R. Follett, M. J. Shoup III, and D. H. Froula, Rev. Sci. Instrum. **83**, 10E349 (2012).
7. S. Semushin and V. Malka, Rev. Sci. Instrum. **72**, 2961 (2001).
8. K. Schmid and L. Veisz, Rev. Sci. Instrum. **83**, 053304 (2012).
9. D. H. Froula *et al*., *Plasma Scattering of Electromagnetic Radiation: Theory and Measurement Techniques*, 2nd ed. (Academic Press, Amsterdam, 2011).
10. A. J. Mackinnon, S. Shiromizu, G. Antonini, J. Auerbach, K. Haney, D. H. Froula, J. Moody, G. Gregori, C. Constantin, C. Sorce, L. Divol, R. L. Griffith, S. Glenzer, J. Satariano, P. K. Whitman, S. N. Locke, E. L. Miller, R. Huff, K. Thorp, W. Armstrong, W. Bahr, W. Seka, G. Pien, J. Mathers, S. Morse, S. Loucks, and S. Stagnitto, Rev. Sci. Instrum. **75**, 3906 (2004).
11. R. K. Follett, J. A. Delettrez, D. H. Edgell, R. J. Henchen, J. Katz, J. F. Myatt, and D. H. Froula, Rev. Sci. Instrum. **87**, 11E401 (2016).

Laser Entrance Window Transmission and Reflection Measurements for Preheating in Magnetized Liner Inertial Fusion

Introduction

Magnetized liner inertial fusion (MagLIF)[1,2] relies on the compression of a cylindrical, axially magnetized, preheated plasma to achieve the temperature and radially integrated magnetic field (*BR*) necessary for fusion ignition: ~7 keV and 0.6 T•m for DT (deuterium–tritium) fusion, respectively.[3] The Z machine has achieved neutron-averaged ion temperatures of up to 3 keV and *BR* of up to 0.4 T•m by compressing deuterium-filled beryllium liners, with an initial 10-T axial magnetic field, preheated with 2.5 kJ of 527-nm light from the Z-Beamlet laser.[4]

Laser-driven MagLIF is now being developed on the OMEGA laser[5–7] to study scaling by driving a target ~10× smaller in linear dimensions than those used on Z, dictated by the ~1000× lower drive energy (from ~10 MJ on Z to ~10 kJ on OMEGA). OMEGA also provides a higher shot rate, better diagnostic access, and x-ray and neutron diagnostics with a greater dynamic range than can be achieved on Z, facilitating parameter scans. Figure 154.36 illustrates MagLIF on Z and OMEGA and the scaling between them.

The initial point design for laser-driven MagLIF on OMEGA is described by Davies *et al.*;[6] a brief overview of the design work and initial experiments is given by Barnak *et al.*;[5] and a more-detailed description of compression-only experiments and simulations is given by Hansen *et al.*[7] Here we describe some of the results from our very first experiment, carried out during the initial design phase, looking at just the laser preheating. MagLIF targets require a preheat laser entrance window that can hold the gas in the target, yet allow sufficient laser energy to enter the gas. A similar situation is also encountered with gas-filled hohlraums, although the gas pressures used are lower, allowing a thinner window to be used. We measured the laser transmission of polyimide foils, selected for our window material, with a calorimeter and three time-resolved spectrometers, at different angles; we also measured the reflection from foils only and from full targets with the time-resolved spectrometers. These measurements were intended to show if sufficient laser energy could be coupled into the target to achieve the goal of preheating to a mean temperature ≥100 eV, established by the point-design simulations.[6] Of particular concern was the possibility of significant backscatter caused by parametric instabilities in the expanding foil plasma. Transmission and reflection measurements can also be directly compared to results from hydrodynamic simulations with ray tracing, providing a test of our simulation capabilities. We used the 2-D code *DRACO*[8] to simulate the experiments.

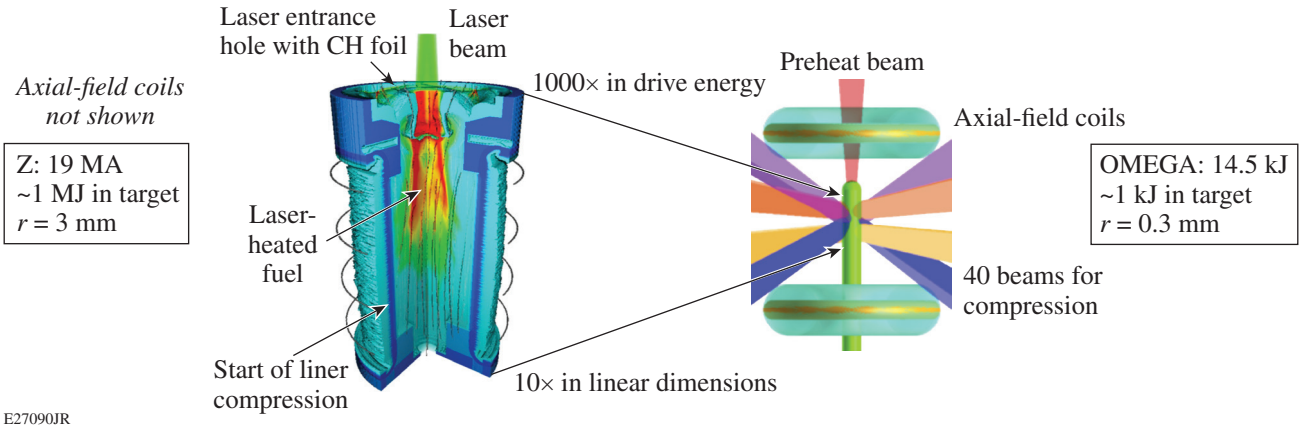

Figure 154.36
An illustration of MagLIF on Z and OMEGA, roughly to scale. The image for Z is from a 3-D simulation and the image for OMEGA is from a 3-D design drawing.

Preheating experiments for Z-scale MagLIF targets have been carried out using the Z-Beamlet laser,[9] OMEGA EP,[10] and OMEGA; for potential ignition-scale MagLIF targets, experiments were carried out on the NIF (National Ignition Facility). The targets in these experiments were all significantly larger than used here and the laser energies and powers were higher, but there is some overlap with the laser intensities and foil thickness used here.

The following sections describe the experimental and simulation methods, respectively; present and analyze the results from both the experiments and simulations; and present the conclusions.

Experimental Methods

1. Targets

The point-design process led to the choice of a 0.6-mm-outer-diam plastic (CH) target, based on available phase plates, with a ≤30-μm-thick shell and a deuterium fuel density from 1.5 to 2.7 mg/cm^3, corresponding to a pressure of 9 to 16 atm at room temperature, based on simulated neutron yields and fuel convergence ratios.[6]

Polyimide ($C_{15}H_5N_3O_2$, 1.44 g/cm^3) was chosen for the window material because of its high ultimate tensile strength and low mean atomic number. The window foils were glued to a plastic washer using compliant glue, and the washers were glued to the outside of the cylindrical targets using epoxy, with the foil on the front of the target. Foils mounted on washers with a 1.1-mm inner diameter were used to measure laser transmission. In a preliminary test, a 2-μm-thick foil burst at a pressure of about 18 atm, so this thickness was chosen for subsequent experiments. The polyimide film delivered by Schafer for these experiments was measured to have a thickness of 1.84±0.01 μm. Z experiments, and associated experiments studying just the preheating, have used 0.5- to 3-μm-thick polyimide as the laser entrance window. During experiments, a series of targets failed at 14 atm, with the washer–target joint being the principle issue, so the experiments described here were carried out with an initial fill pressure of 11 atm. Slow leaks led to the pressure at shot time, measured using a pressure transducer on the fill tube at the back of the target, being lower than 11 atm; final pressures varied from 5.2 to 10.9 atm. Design drawings of the targets are shown in Fig. 154.37.

The cylindrical targets for these experiments were made of 30-μm-thick fluorinated parylene-AF4 ($C_8H_4F_4$, 1.32 g/cm^3, also denoted by the suffixes SF, HT, and VT), and the deuterium gas was doped with 2% Ne, by atom, for x-ray diagnostics.

The foils on the full targets bowed outward under the pressure, as can be seen in Fig. 154.38(b), which is the only image of a full target where the foil is visible because the metal x-ray shield was not attached. The force on the foils certainly exceeded the yield stress; flat-plate calculations showed that they would rupture below 10 atm, but for a hemisphere, the stress is below the ultimate tensile strength. Foil bowing can also be caused by motion of the glue joint, which was chosen to be compliant to reduce the risk of tearing, so we cannot be certain of the actual thickness of the foils on the full targets.

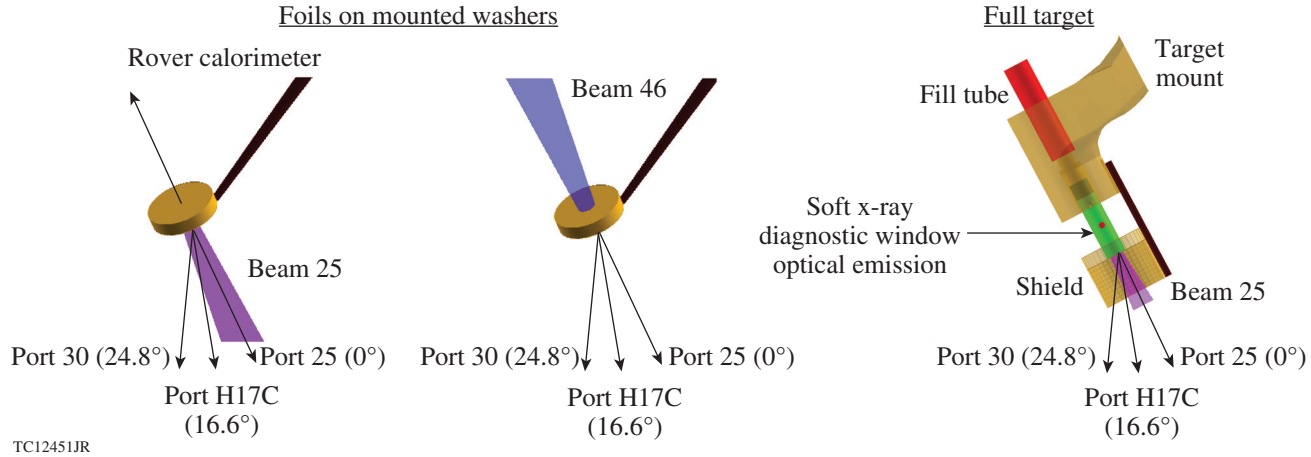

Figure 154.37
Design drawings of the targets used in the experiments, indicating the beams used and the ports through which light was collected. The full targets had a polyimide window on the side and a metal shield around the entrance window for the sake of the soft x-ray diagnostics (not considered here).

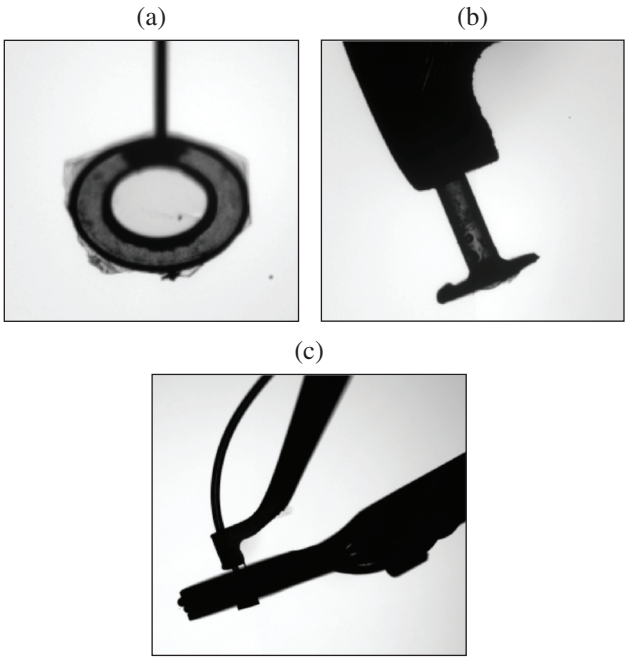

Figure 154.38
Images from the OMEGA Target Viewing System: (a) a foil target from shot 76671, (b) a full target from shot 76683, which was the only one that had no cylindrical metal shield around the entrance window, and (c) a full target with a magnetic-field coil from shot 76673, with a lower magnification than (a) and (b).

MagLIF targets require an axial magnetic field, ideally around 30 T (Refs. 1 and 6). Therefore, a magnetic field was applied on two full target shots using a single multiple-turn coil near the center, which can be seen in Fig. 154.38(c). The radius of the coil was sufficient to give a roughly constant field of 15 T over the region of interest.

2. Laser Parameters

The pulse shape for the preheat beam must be the same as the pulse shape for the compression beams because OMEGA has independent pulse shaping on only one of the three legs of beams, and beams from all three legs are necessary for the compression; therefore, a square-shaped pulse was used.[6] Preliminary 1-D simulations indicated that a 2.5-ns pulse was ideal for the compression; therefore, we used this pulse duration. These simulations did not take into account, however, the rapid fall in energy on target above 1 ns, resulting from the fall in frequency-conversion efficiency with power. When the measured maximum energies were used in the simulations,[6] the ideal pulse duration was found to be 1.5 ns. The longer pulse used in these experiments is not a significant factor because it still provides the information we need for a 1.5-ns pulse of the same power since we have time-resolved diagnostics.

MagLIF on Z uses a prepulse to explode the window, which minimizes the energy absorbed by the window and the density of the window plasma seen by the main pulse. On the other hand, it gives the window plasma more time to propagate into the target.

Figure 154.39 shows the measured pulse shapes for all of the shots taken. The laser power on target takes into account initial laser energy, frequency-conversion efficiency, and the transmission of the phase plate and blast window assembly. The measurements should be accurate to better than ±5%. With the exception of the first shot, where the power increases near the end, the pulse shapes are very similar, so the only significant variation between shots is the total energy, as intended.

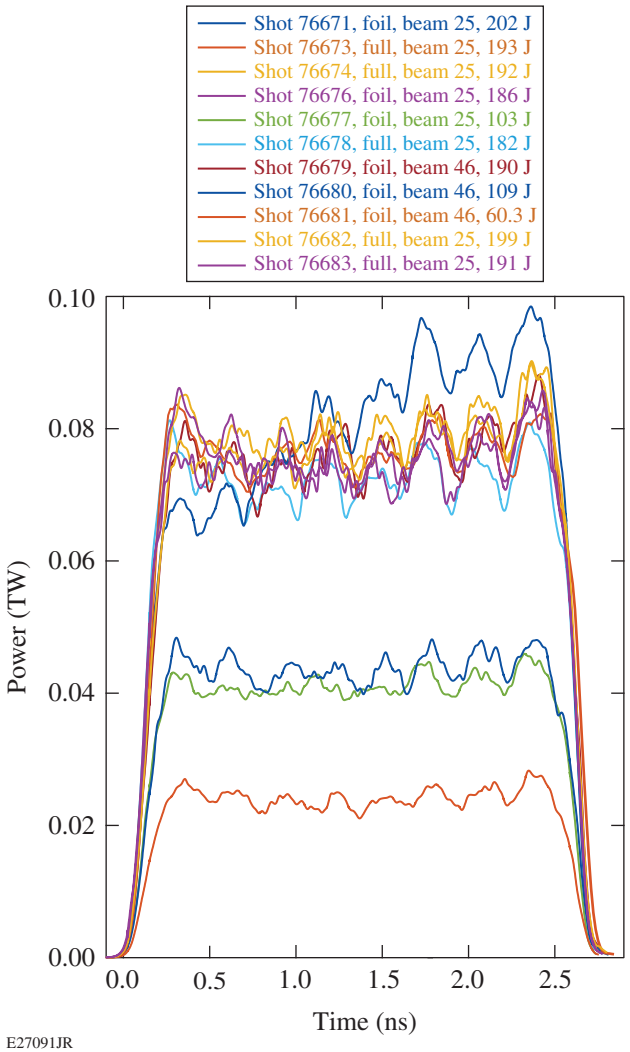

Figure 154.39
Measured pulse shapes for all of the shots taken, indicating the target type, beam number, and total energy on target.

Smoothing by spectral dispersion (SSD), a distributed polarization rotator (DPR), and a distributed phase plate (DPP) were used to give the best-possible laser uniformity available on OMEGA. The smallest phase plate available on OMEGA that gives an almost round, smooth laser spot was used; a smaller phase plate exists but it gives an almost square spot with considerable intensity modulations. An equivalent-target-plane image of the chosen phase plate is shown in Fig. 154.40, including a DPR and SSD, taken after the initial design work and experiments were completed. A Gaussian

$$I = I_0 \exp\left(-\frac{r^2}{R^2}\right) \tag{1}$$

was found to give an adequate fit, with $R = 108.8 \pm 0.1$ μm (95% confidence bounds), using a 2-D fitting routine, which is shown in Fig. 154.40. The peak intensity for a total energy E J in 2.5 ns is

$$I_0 = 1.08 \times 10^{12}\, E \text{ W/cm}^2. \tag{2}$$

A super-Gaussian fit to an older image (original data no longer available) gave

$$I = 7.60 \times 10^{11}\, E \exp\left\{-\left[\left(\frac{r}{126.8\ \mu\text{m}}\right)^2\right]^{1.195}\right\} \text{W/cm}^2, \tag{3}$$

which was used to simulate the initial preheat.[6]

Preliminary 2-D simulations for a deuterium fill pressure of 10 atm indicated that a total energy of 200 J in 2.5 ns would be sufficient to achieve a mean temperature of 200 eV over a 1-mm-long region of the gas ahead of the window plasma, which was the preheat temperature chosen for the point design. A preheat scan in the 1-D simulations for the point design[6] showed a threshold preheat of 100 eV, for which 2-D simulations indicated a total energy of 60 J in 2.5 ns would be sufficient. As an intermediate value, we chose 100 J, so the requested energies on target were 200, 100, and 60 J, corresponding to mean laser powers of 80, 40, and 24 GW, and time-averaged peak intensities of 2.2, 1.1, and 0.65×10^{14} W/cm^2 [from Eq. (2)]. The actual on-target energies are reported in Fig. 154.39. Z experiments, and associated experiments studying only the preheating, have used laser powers from 0.2 to 1 TW and intensities from 0.5 to 5×10^{14} W/cm^2.

3. Diagnostics

The diagnostics considered here are laser calorimeters and time-resolved spectra. OMEGA has two full-aperture backscatter stations (FABS) on Beamlines 25 and 30 that are at 24.6° to one another. These systems collect light coming back through the laser lens and separate it into two wavelength bands: one that includes 351 nm (the laser wavelength), intended for stimulated Brillouin scatter (SBS); and one at longer wavelengths, intended for stimulated Raman scatter (SRS) and two-plasmon decay (TPD), each of which is split between a calorimeter and a streaked spectrometer. The laser lenses are 30 cm in diameter and 180 cm from the target chamber center, so ports 25 and 30 cover ±4.77°. A similar system is also implemented on two

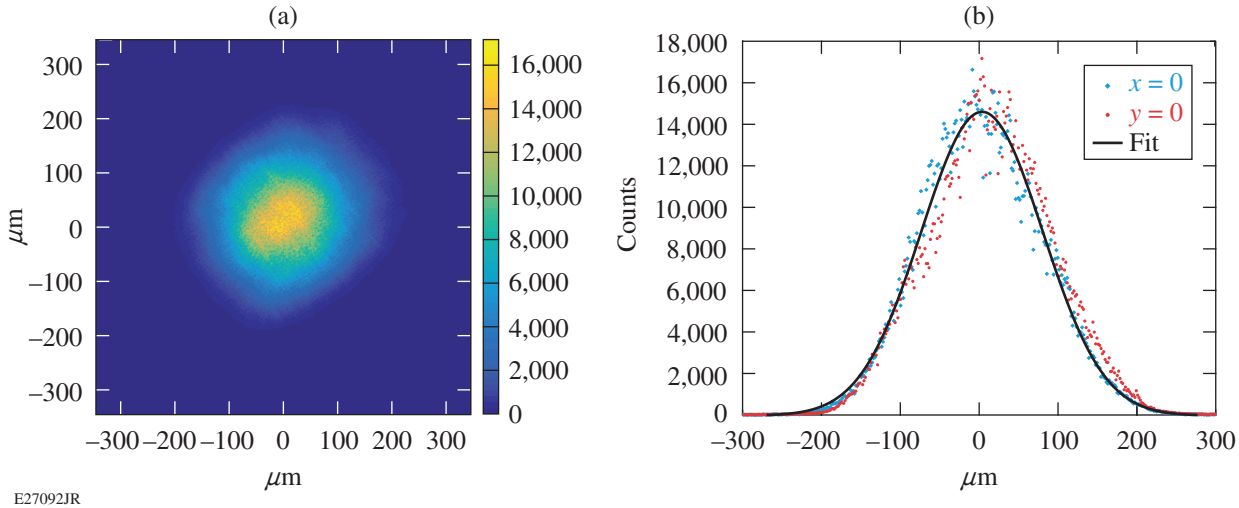

Figure 154.40
(a) Equivalent-target-plane image obtained with the distributed phase plate used in the experiments, including a distributed polarization rotator, and with smoothing by spectral dispersion on; (b) horizontal and vertical lineouts through the center of the image with the Gaussian fit.

smaller diagnostic ports; of interest here is port H17C that uses a 2.2225-cm-diam lens and is situated at 16.6° to Beamline 25, so it covers ±0.35°. A calorimeter, known as the Rover, can be used to collect the light coming through any one of OMEGA's beam ports.

We used Beamline 25 on foil and full targets to measure time-resolved backscatter at $\theta = 0°$, 16.6°, and 24.6°; for the foil targets, we used the Rover calorimeter on opposing port 46 to measure total transmission along the original beam path. We then used Beamline 46 on foil targets to measure time-resolved transmission at $\theta = 0°$, 16.6°, and 24.6°, using the measurement of the total transmitted energy to determine the filtering that would be required to avoid damaging the system. The diagnostic setup is illustrated in Fig. 154.37.

All of the measurements taken using the FABS and H17C are traditionally referred to as backscatter. Here we will refer to the measurements taken using Beamline 46 as transmission and the measurements taken using Beamline 25 as reflection. We will refer to the transmission and reflection measurements taken using 25 as direct since this corresponds to energy within the original beam cone, and to the transmission and reflection measurements taken using H17C and 30 as sidescatter since they correspond to energy outside the original beam cone.

For all except the direct transmission measurements, the signals on the calorimeters were too low to give the total energy, but the streaked spectrometers are more sensitive and did have a usable signal. To determine the total energies, the ratio between the energy registered by the calorimeters and the total signal on the streaked spectrometers was taken from four spherical implosion shots from the immediately preceding shot day, taking into account the differences in filtering. The standard errors from these energy calibrations are ±7% for 25, ±16% for H17C, and ±14% for 30; we assume that this is the dominant source of error. The uncertainty in the calibration of the Rover calorimeter is estimated to be ±5%.

Some uncertainty exists in the relative timings of the signals in 25, H17C, 30, and the laser pulse. The OMEGA timing fiducial should be accurate to within ±10 ps, but the sampling interval of the time-resolved spectrometers is ~15 ps, so the relative timing cannot be more accurate than this. It is possible that there is a greater systematic error in the determination of the relative values of $t = 0$ in the diagnostics.

Two soft x-ray imaging systems, a time-resolved soft x-ray spectrometer, and streaked optical pyrometry of the outer surface of the cylinders were also fielded but will not be considered here.

Simulation Methods

The shots were simulated using the Eulerian version of the 2-D radiation–hydrodynamic code *DRACO*, which uses 3-D ray tracing with inverse bremsstrahlung energy deposition,[8] which is the standard for these types of simulations.

Several simplifications were made to the targets: The foil was taken to be 1.8 μm thick rather than the measured value of 1.84 μm. The glue was not considered. For the foil shots, the washer was not considered since its inner diameter was significantly greater than the laser spot. For the full targets, the washer was considered to be part of the cylinder, the curvature and possible stretching of the foil were not considered, and the cylinders were truncated after ~1.8 mm at an open boundary. Foil curvature is difficult to simulate on a rectangular Eulerian grid, and the exact shape is not known. The code cannot deal with vacuum, so, instead, hydrogen with a density of 1 μg/cm^3 was used. The "vacuum" density was increased by a factor of 10 and found not to affect the results.

The 15-T axial magnetic field, applied on full-target shots 76673 and 76674, was not considered and is expected to have a negligible effect on the laser–foil interaction since the Hall parameter remains less than 1 and the magnetic pressure is negligible.

An axial grid spacing of 0.2 μm was used in the foil and was increased by 10% for each cell moving away from the foil. For the full targets, the axial grid spacing inside the cylinder was capped at 2.5 μm. The radial grid spacing was 2.5 μm up to the edge of the cylinder and was increased by 10% per cell beyond. To test that the grid spacing was adequate, the axial grid spacing around the foil was reduced to 0.1 μm, the radial grid spacing was reduced to 1 μm, and the regions of uniform grid spacing were extended; it was found that these changes did not modify the results.

Defining $z = 0$ to be the center of the foil and the laser to enter from the positive z direction, the simulation box for the foil runs extended from approximately $z = -1.51$ mm to $z = 1.66$ mm and for full target runs from approximately $z = -1.82$ mm to $z = 4.3$ mm. Defining $r = 0$ to be the axis of rotational symmetry, the simulation box for the foil runs extended up to approximately $r = 0.581$ mm and for full target runs up to $r = 0.51$ mm. The boundary conditions were reflective at $r = 0$ and open for all other boundaries.

SESAME equations of state were used: for polyimide a table for mylar ($C_{10}H_8O_4$) was chosen, being the closest material available; for parylene-AF4, a table for polystyrene (CH) was chosen; and the neon-doped deuterium was treated as deuterium. To test the sensitivity to the equation of state, the polystyrene equation of state was also used for the polyimide and found to have no noticeable effect. Twelve-group radiation transport was used with opacities, emissivities, and mean ionization levels calculated by the *PrismSPECT* collisional-radiative-equilibrium model for the materials used. For the hydrogen "vacuum," the ideal gas equation of state was applied and treated as fully ionized.

The standard Spitzer–Härm thermal conduction model was used with a flux limiter of 0.06. For one run (shot 76676), no flux limiter was also considered, which marginally increased the laser energy absorbed by the foil, increasing the difference between simulation and measurement.

The measured laser powers shown in Fig. 154.39 and the laser intensity profile given by Eq. (3) were used in the ray tracing. In one run (shot 76676), Eq. (1) was also used for the intensity profile. The 42% increase in peak intensity led to an upturn in transmission, explained in the next section, occurring about 0.05 ns earlier, and to a 2.35% increase in directly transmitted energy. The uncertainty in the actual laser parameters can be treated as an uncertainty in the simulation results, which is clearly less than the uncertainty in the measurements with which they are being compared. The simulations were started at –0.1 ns because there is laser power before the facility-defined $t = 0$, and a signal was detected in the time-resolved spectrometers before $t = 0$. Laser imprinting, which calculates the random intensity fluctuations expected for a beam with SSD, DPR, and DPP, was tested in some runs and found to make no noticeable difference in the results of interest. The boundary through which the rays enter and leave if reflected is set by the largest value of z for which electron density $n_e \geq 0.01\, n_c$, where n_c is the critical density or the boundary of the simulation box, whichever is smaller. The ray-tracing routine simulates the FABS diagnostic by collecting rays at user-specified "ports," assuming straight-line propagation outside the ray-tracing grid, and by calculating the frequency shift using the electron density and fluid velocity at the time step at which the ray tracing is carried out. When the actual diameter of the H17C port was used, no rays were collected, so it was increased by a factor of 10 and the energy was divided by a factor of 100 for comparison with the experimental results. In the code it is possible to make all six measurements simultaneously, so only foil shots 76676 (185.6 J), 76677 (102.6 J), and 76681 (60.3 J) were simulated since these cover the full range of laser energies. For the full targets, only shots 76678 (181.8 J, 10.9 atm of fill pressure) and 76682 (198.6 J, 5.2 atm of fill pressure) were simulated since the energies on target were very similar for all full target shots and these represent the extremes in fill pressure. For comparison with the experimental results for other shots, the energies collected by the diagnostic ports in the code were scaled linearly with laser energy from the run with the closest energy. The results presented here used 1000 rays per radial cell. Runs with only 100 rays per cell gave very similar results but had too few rays in all but the direct transmission diagnostic.

Results

1. Foil Targets

The energies collected by the Rover calorimeter in port 46 and in the SBS (laser) channel of the time-resolved spectrometers in ports 25, H17C, and 30 are given in Table 154.IV with the simulated values underneath. No detectable signal was obtained in the SRS channel on any of our shots. No reflected energies were measured on the first shot because the initial filtering was too strong; the reflected energies turned out to be close to the detection threshold.

The most-significant results from Table 154.IV for the laser-driven MagLIF project are (1) direct transmission exceeds the simulated values by ~10% of the laser energy, so simulations would be expected to slightly underestimate gas heating; and (2) sidescatter of transmitted light is negligible, so direct laser heating of the wall should not be an issue. Sidescatter of transmitted light is a factor of roughly 100× higher than simulated, but the simulations show that thermal conduction dominates wall heating;[6] even increasing the laser energy incident on the wall by a factor of 100 would still make it a small contribution.

It is worth noting that thermal conduction into the wall during preheat is only an issue for the smaller targets used on OMEGA, not for those used on Z, because thermal diffusion time scales as r^2, so it is not scale invariant. On Z, the shock generated by the preheating will reach the wall before thermal diffusion heats it to any significant extent. If there is sidescattered transmission on Z, it would dominate wall heating at early times, and the longer time scales on Z compared to OMEGA could lead to a significant direct laser contribution to wall blow-in.

To estimate the total sidescattered energies, we extrapolated from the energy per unit area in ports H17C and 30 using a Gaussian $\exp(-r^2/R^2)$ and a circular diffraction profile $J_1(r/R)/(r/R)$, where J is a Bessel function of the first kind, in $r \approx L\theta$, where L is the distance from target chamber center to

Table 154.IV: Results for foils, giving laser beam number, laser energy (E), and laser energy collected by the diagnostics in ports 46, 25, H17C, and 30, with simulated results underneath. The percentage in parentheses is with respect to the incoming energy per unit area at the laser port. Transmitted energies are shown in bold. The calibration errors are estimated at ±5% for the calorimeter used in 46, ±7% for 25, ±16% for H17C, and ±14% for 30, as explained in the text.

Beam	E (J)	46 (%) Simulation	25 (%) Simulation	H17C (%) Simulation	30 (%) Simulation
25	202	**131 J (64)** **113 J (56)**	– –	– –	– –
25	186	**116 J (62)** **104 J (56)**	85.3 mJ (0.046) 3.23 J (1.7)	0.161 mJ (0.016) 0.946 μJ (<0.001)	14.6 mJ (0.008) 27.3 μJ (<0.001)
25	103	**60.3 J (59)** **48.8 J (48)**	51.2 mJ (0.050) 2.35 J (2.3)	0.101 mJ (0.018) 35.1 nJ (<0.001)	8.63 mJ (0.008) 1.55 μJ (<0.001)
46	190	– –	**126 J (66)** **106 J (56)**	**0.210 mJ (0.20)** **13.3 μJ (0.01)**	**3.94 mJ (0.002)** **0.319 mJ (<0.001)**
46	109	– –	**65.2 J (60)** **51.8 J (48)**	**67.3 μJ (0.011)** **13.8 μJ (0.002)**	**2.94 mJ (0.003)** **0.306 mJ (<0.001)**
46	60.3	– –	**31.7 J (53)** **23.6 J (39)**	**0.178 mJ (0.054)** **7.56 μJ (0.002)**	**2.02 mJ (0.003)** **0.196 mJ (<0.001)**

the ports (1.8 m), to find the total energy outside port 25. These profiles were chosen because they represent, approximately, the initial laser profile and the profile of a plane wave passing through a circular hole, potentially a small hole initially made in the foil by the laser. The ratio of the energies per unit area in H17C and 30 determines R, and the magnitude of either signal determines the peak energy per unit area. We could not adequately fit the three measurements together with either a Gaussian or a variety of Bessel-based functions; any function with three free parameters could of course be used to extrapolate from the three measurements.

For transmission, the Gaussian extrapolation gave the fraction of sidescattered laser energy to be 0.82%, 0.33%, and 0.85%, and the circular diffraction extrapolation gave 0.72%, 0.82%, and 1.14%, for laser energies of 190, 109, and 60.3 J, respectively, which are not significant. The extrapolated energy in port 25 was always much less than the measured value. Circular diffraction gives a consistent trend with laser energy and less variation than the Gaussian, so it would appear to be a better assumption for sidescattered transmission.

For reflection, the circular diffraction extrapolation put too much energy into port 25 for two of the three foil shots. The Gaussian extrapolation put the *total* reflected energy at 0.6% of the laser energy for both of the foil shots that measured reflection, confirming that the total is negligible. According to this extrapolation, most of the energy is reflected outside of the incoming beam cone.

Using the equations for circular diffraction, or a Gaussian beam, it is possible to extrapolate back from the radius R at the detectors to a radius R_f at the foil of $L\lambda/2\pi R$, where L is distance from port to target (1.8 m) and λ is laser wavelength (351 nm). The circular diffraction extrapolation for transmission gave radii of 1.27, 1.25, and 0.77λ, for laser energies of 190, 109, and 60.3 J, respectively (the Gaussian extrapolation gave 0.84, 0.64, and 0.77λ). Treating the reflected signals in H17C and 30 as a Gaussian beam originating at the foil gave unphysically small values of R_f; a diffuse reflection is probably a better description for these measurements.

The direct transmitted power as a function of time for the three laser energies used is shown in Fig. 154.41. The measurements show a rapid transition to total transmission, which occurs later for lower laser energies. The simulations adequately capture the initial increase in transmission, which occurs as the foil becomes underdense, as shown by the critical density contour in Fig. 154.42 at 0.45 ns, but the subsequent rise in transmission as the foil expands is slower and never quite reaches total transmission, which leads to an underestimate of the total transmitted energy.

The falling edges of the direct transmission and laser pulse measurements shown in Fig. 154.41 match to within one point of the transmission measurements (~15 ps), indicating that the relative timings between 25 and the laser pulse are accurate. We do not have as clear a reference to determine the accuracy of the relative timings of H17C and 30. The agreement between

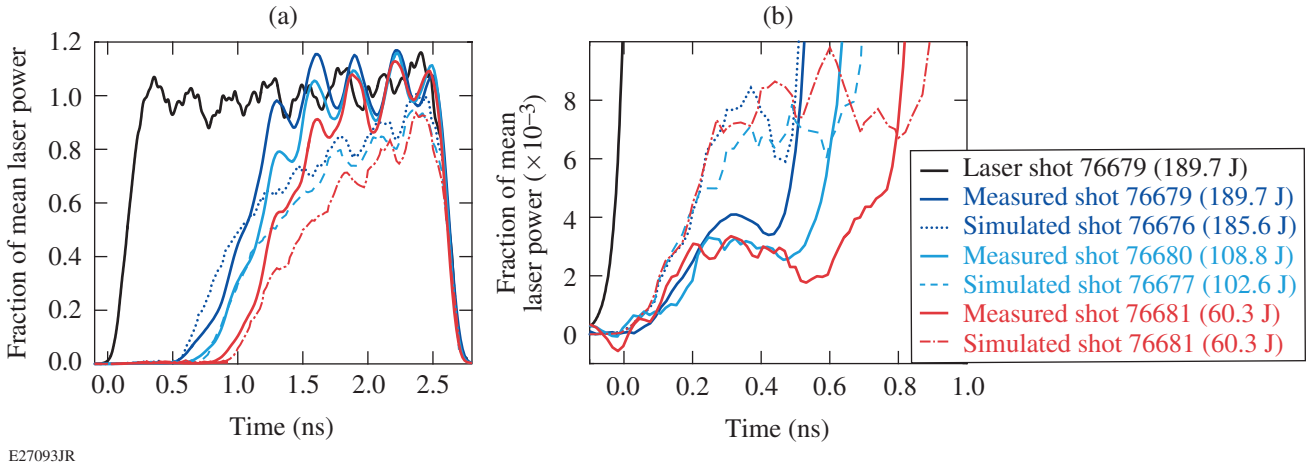

Figure 154.41
Direct transmitted laser power as a fraction of the mean laser power versus time for the three foil shots taken with Beamline 46, with the simulated results, and the laser power on target for one shot.

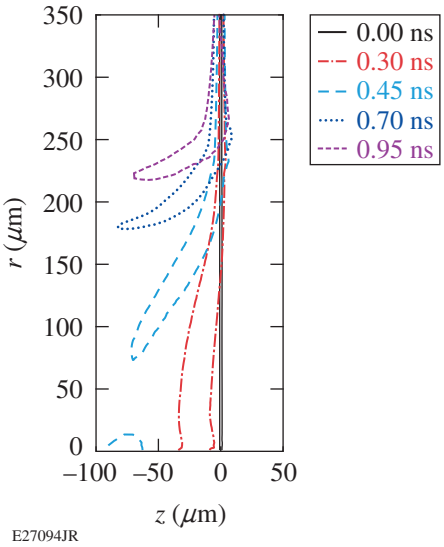

Figure 154.42
Critical-density contours at a sequence of times from the simulation of shot 76676 (foil, 186 J).

the direct transmitted laser power and the measured laser power indicates that the absolute energy calibration is accurate. The direct transmission does not show all of the structure seen in the laser pulse measurements because it has ~200 points versus ~1000 points for the laser pulse measurement.

There is a small peak in direct transmitted power during the rising edge of the laser pulse, just before the sudden increase in transmission, which is captured in the simulations, although it is overestimated. The cold polyimide foil would transmit a fraction of the laser light, and this fraction would fall as it is ionized by the laser. The instantaneous transmission cannot be accurately determined because of the noise in the measurements of both the laser power and the transmitted power and the uncertainty in their relative timings, which lead to large error bars, but it is clear from the rise in the laser power that transmission is falling during this phase. In the simulations, a minimum ionization level $Z = 0.11$ is imposed on the polyimide so it is initially at critical density to avoid high transmission and start inverse bremsstrahlung absorption. The optical depth of an overdense cell ($n_e \geq n_c$) is fixed an at arbitrary upper limit, which results in some transmission. The initial transmission in the simulation is therefore somewhat arbitrary. The transmission falls because the ionization level increases and the foil expands, increasing the width of the overdense region, as seen in Fig. 154.42, from 0 to 0.3 ns. Therefore, coincidentally, the simulations are comparable to the measurements on the rising edge of the pulse because the code has no accurate physical model for solids. Strictly speaking, the laser model is accurate for only ideal underdense ($n_e < n_c$) plasma. The agreement of the simulations with the measurements in this phase could be improved by modifying the minimum ionization level of polyimide and the optical depth of an overdense cell, but this would not be a physically meaningful agreement and might work only for the specific set of parameters considered.

The final choice of pulse duration for laser-driven MagLIF was 1.5 ns, not the 2.5 ns used here, as discussed in the **Introduction** (p. 91). The time-resolved measurements show that the direct transmitted energy at 1.5 ns was 36.1, 15.1, and 5.43 J for laser powers of 75.9, 43.5, and 24.1 GW, respectively. In

the simulations, 24.1 GW was sufficient to achieve the objective of a mean gas temperature of 100 eV over the region to be compressed, and the transmitted energy was 23.6 J. Therefore, a power of 75.9 GW with a pulse duration of 1.5 ns, giving a total laser energy of 114 J and a transmitted energy of 36.1 J, should exceed 100 eV but fall short of 200 eV, which was achieved in the simulations with ~100 J of transmitted energy at 75.9 GW.

The transmitted intensities as a function of time at all three angles for shot 76679 are shown in Fig. 154.43; the results for the other two shots differ only significantly in their timing, as seen in the direct transmission. Intensity is used here so that the smaller H17C can be compared to 25 and 30. Sidescatter is measured only for a brief period during the transition to total transmission. The simulations roughly match the timing and duration of the sidescatter, but at a much lower level. Sidescatter of transmitted light occurs in the simulations because of refraction around the lip of the remaining overdense foil plasma, seen in Fig. 154.42 from 0.45 ns onward, and because of focusing by the electron density profile of the underdense foil plasma. A better illustration of these features in the simulations is given by Fig. 154.44, which gives the deposited power density with electron density contours overlaid for shot 76676 at 0.7 ns, the time of the peak in sidescattered transmission. The measurements imply either that the hole in the foil is much smaller and the focusing of the transmitted beam is much greater than seen in the simulations, or that just the focusing in the underdense plasma is much greater.

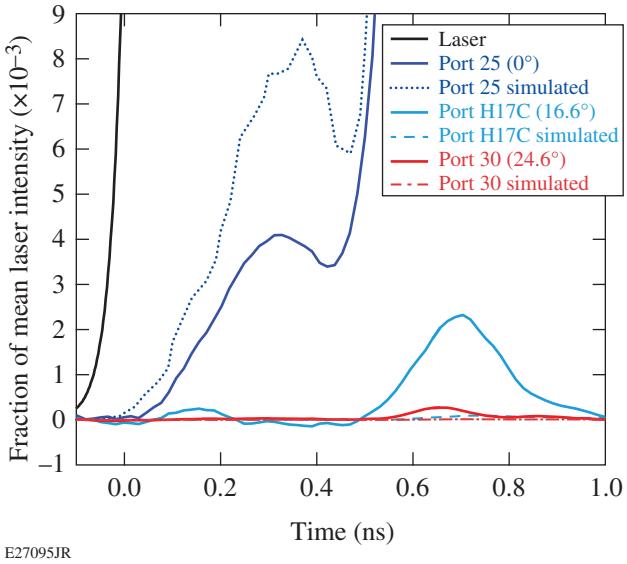

Figure 154.43
Transmitted laser intensities at ports 25, H17C, and 30 as a fraction of the mean laser intensity at the laser port versus time for shot 76679 (foil, 190 J), with the simulated results, and the incoming laser intensity.

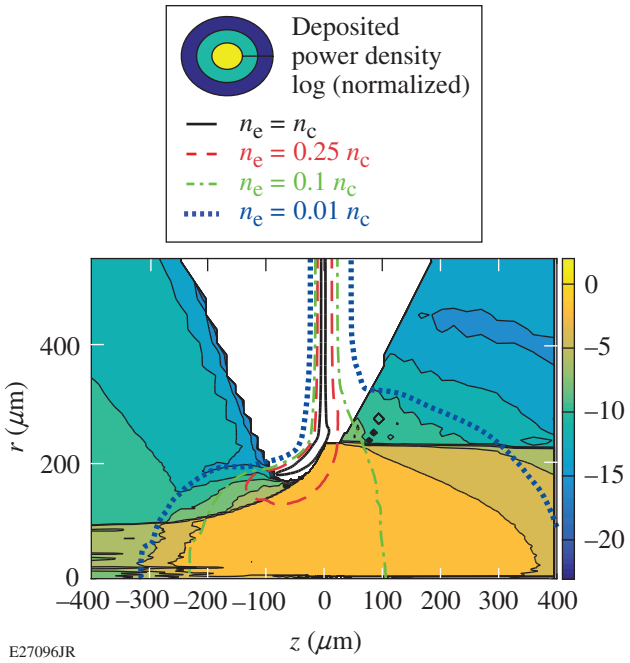

Figure 154.44
Deposited power density, normalized to a maximum value of 1, and electron density contours from the simulation for shot 76676 (foil, 186 J) at 0.7 ns, when sidescattered transmission peaks.

The reflected intensities at all three angles for shot 76676 (186 J) are shown in Fig. 154.45; they are shown again in Fig. 154.46 combined with the transmitted intensities for shot 76679 (190 J). The reflected intensities measured for shot 76677 (103 J), as a fraction of the laser intensity, are practically identical. Reflection is measured only prior to the rapid increase in transmission. Initially, only direct (specular) reflection is measured, with the sidescattered signals rising later on; in other words, the reflected light is spread over an increasing angle until it ceases. The falling edges of all three signals match quite closely and coincide with the initial fall in direct transmission. The magnitude of the simulated reflections differs by so much that they are difficult to fit on the same graph as the measurements; the simulated signal in 25 is much higher and lasts throughout the laser pulse, which is not surprising given that the simulations never show total transmission, and the H17C and 30 signals have been multiplied by a factor of 100 to be visible. The simulations also show a higher reflectivity for the lower energy shot 76679, whereas the measurements show no change in percentage reflectivity. The simulated timings for all three signals do match the measurements reasonably well, considering just the initial rise for 25. The sidescattered

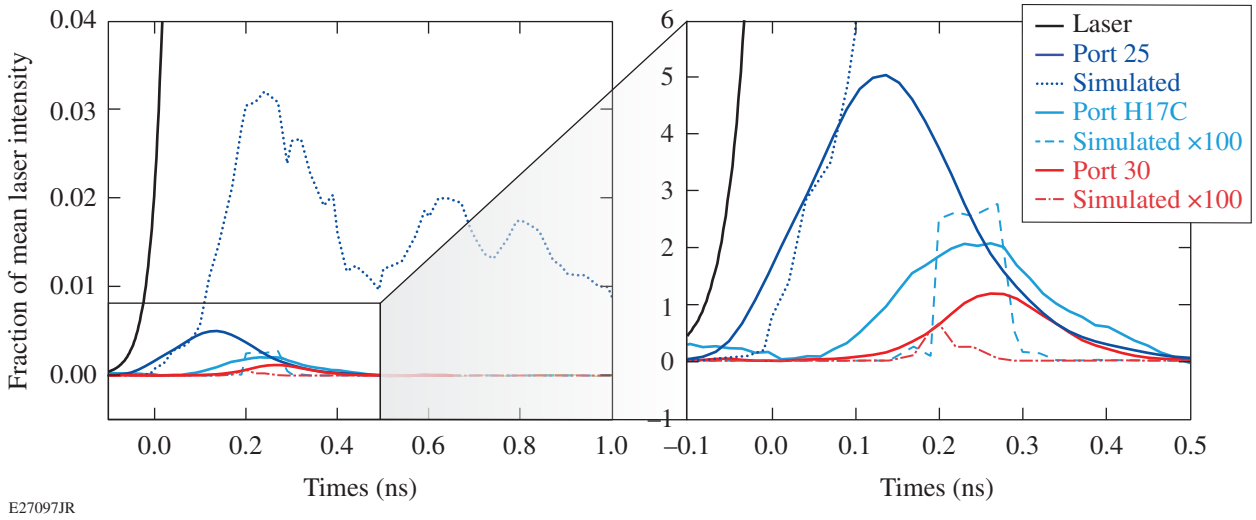

Figure 154.45
Reflected laser intensities at ports 25, H17C, and 30 as a fraction of the mean laser intensity at the laser port versus time for shot 76676 (foil, 186 J) with the simulated results and the incoming laser intensity.

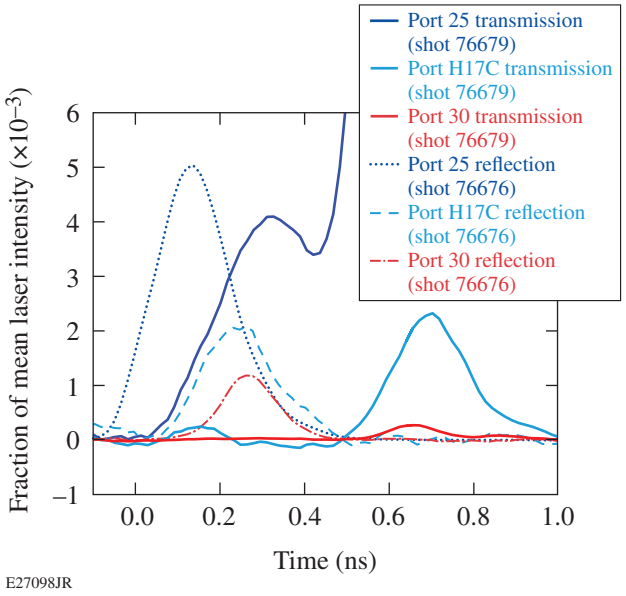

Figure 154.46
Transmitted laser intensities from shot 76679 (foil, 190 J) and reflected laser intensities from shot 76676 (foil, 186 J) as fractions of the mean laser intensity at the laser port versus time.

reflection occurs in the simulations because of curvature of the overdense plasma, seen in Fig. 154.42 at 0.3 ns. It is possible that the simulations underestimate this curvature. However, since reflection occurs before the foil becomes underdense, the simulations could also be in error because they have no accurate physical model for solids and overdense plasma. Overall, this initial phase of reflection, and transmission, is not energetically significant.

Streaked spectra of the transmitted light measured for shot 76679 in ports 25 and H17C are given in Fig. 154.47; port 30 looks similar to H17C, and the spectra from the other shots differ principally in timing. There is a lot of structure in the direct transmitted spectrum, which is a result of SSD. The simulations do not include SSD, using a delta function wavelength distribution at 351 nm, so they are not directly comparable. There is a red shift in all of the transmitted light signals during the transition to total transmission, which is the only time signal seen in H17C and 30.

All of the spectra for shot 76679—integrated over 0.6 to 0.8 ns, the duration of the emission in H17C and 30—are shown in Fig. 154.48. The red shift is seen to increase with angle, from 25 to H17C to 30. The simulated results are significantly narrower because they do not include the initial bandwidth and the instrument broadening, but they clearly show a smaller blue shift that is larger in 25 than in H17C and 30, the complete opposite of the measurements. The blue shift is caused by the axial velocity of the plasma expanding behind the foil. The red shift seen in the measurements could be caused by a rapid drop in plasma density or by plasma motion away from the detector, at a speed much greater than those achieved in the simulations. There is certainly a rapid drop in plasma density between 0.6 and 0.8 ns because the transmitted powers show that there is practically nothing in the path of the laser shortly

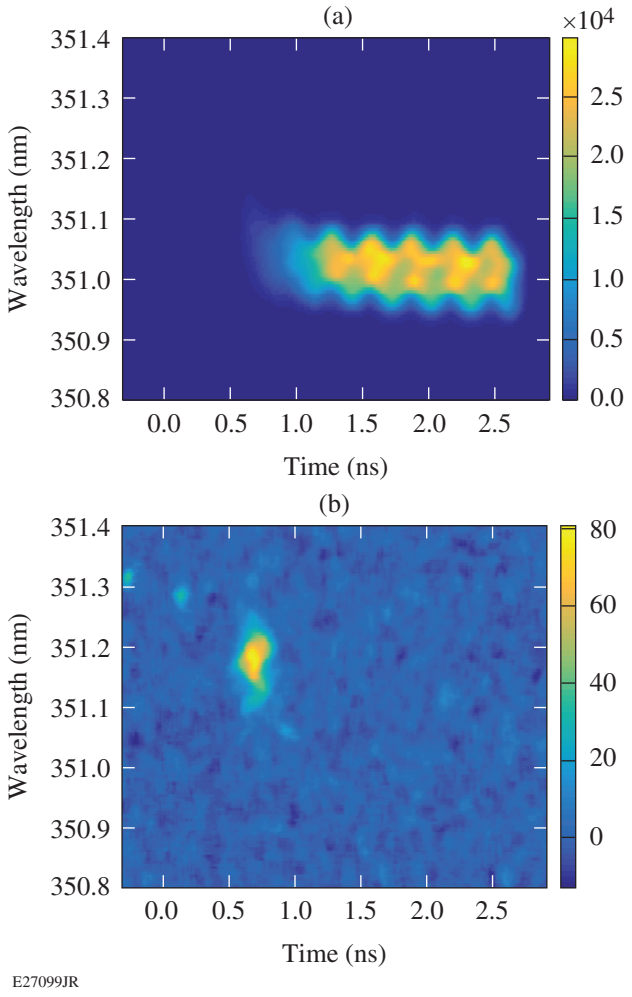

Figure 154.47
Transmission data from the streaked spectrometers in (a) 25 and (b) H17C for shot 76679 (foil, 190 J). A mean background level has been subtracted.

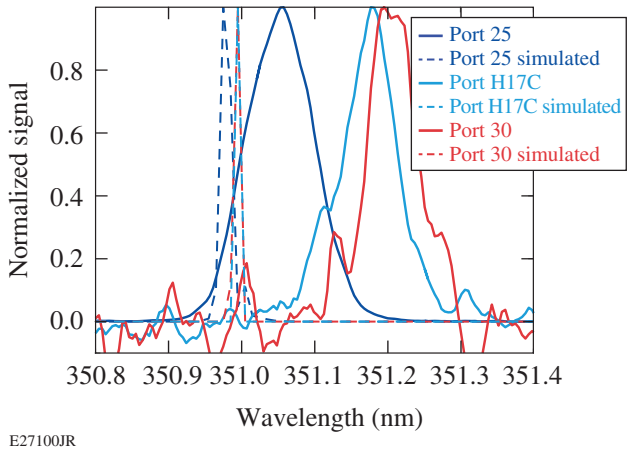

Figure 154.48
Spectra of transmitted light for shot 76679 (foil, 190 J) integrated over the duration of the measured, sidescattered signals, normalized to a peak value of 1, with the results from the simulation for shot 76676 (foil, 186 J).

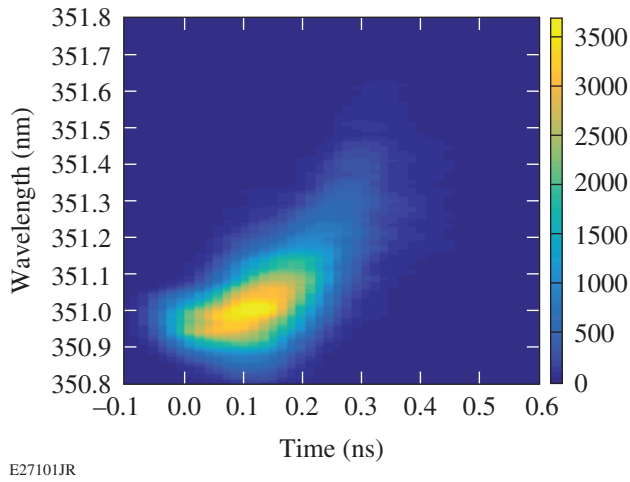

Figure 154.49
Reflection data from the streaked spectrometer in 25 for shot 76676 (foil, 186 J). A mean background level has been subtracted.

after 0.8 ns. The axial plasma expansion cannot be significantly faster than in the simulations because that would require higher absorption. The only way to achieve rapid evacuation of the plasma from the beam path is radial motion. If the plasma is being pushed out rapidly in the radial direction, the red shift could also be caused by reflection from the radially expanding plasma, which would give a greater shift at larger angles, as observed.

The streaked spectrum of reflected light measured for shot 76676 in port 25 is given in Fig. 154.49; H17C and 30 show similar signals, but they are too close to the background level to readily distinguish features; the results for shot 76677 look very similar. The initial blue shift, seen up to ~0.2 ns, can be caused by plasma expansion from the foil surface and by ionization of the foil. The red shift, which increases throughout the duration of the signal, is almost certainly caused by the overdense portion of the foil being accelerated in the direction of the laser beam, which can be seen in the simulations in Fig. 154.42.

All of the spectra for shot 76676 integrated over 0 to 0.5 ns, the duration of the measured signal, are shown in Fig. 154.50. It is difficult to compare the measured and simulated values because the simulations do not include the initial bandwidth and instrument broadening, and the measured values for H17C and 30 have a low signal-to-noise ratio. The simulation does show a combination of blue and red shifts, with the exception of 30, which shows only a blue shift, but the magnitude of the red shift

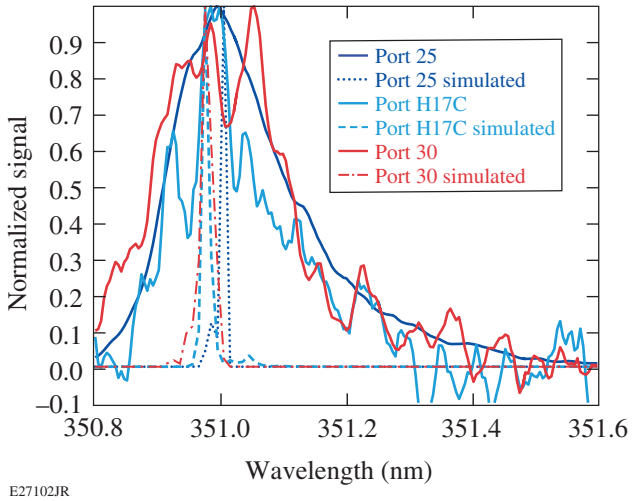

Figure 154.50
Spectra of reflected light for shot 76676 (foil, 186 J) integrated over the duration of the measured signals, normalized to a peak value of 1, with the results from the simulation.

is clearly lower than measured, indicating that the simulations underestimate the inward acceleration of the overdense plasma.

2. Full Targets

The energies collected in the SBS (laser) channel of the time-resolved spectrometers in ports 25, H17C, and 30 are given in Table 154.V, with the simulated values underneath. The values from the two foil shots that measured reflection are included for ease of comparison.

The most significant results from Table 154.V for the laser-driven MagLIF project show that reflection from full targets is small and comparable to the foil shots, indicating that the transmission of the foils in the full targets should also be comparable to the transmission measured for foils alone. There is no sign of SBS, or SRS, from the gas. Therefore, we expect the simulations to be adequate for the gas heating, giving a slight underestimate because of the underestimate of the energy transmitted by the foil.

The mean direct reflectivity for the two foils is 0.048±0.004% (standard error plus uncertainty from the calibration) and for the five full targets is 0.038±0.014%, so they can be considered to be in agreement within the uncertainties. The simulations give 1.6% for the nominally 200-J shots on foils and full target and 2.3% for the nominally 100-J shot on a foil; the measurements do not indicate a variation in reflectivity over this energy range, but there is only one shot at 100 J. Using a Gaussian to extrapolate the energy outside port 25 from the energy per area measured in H17C and 30 gives total reflectivities of 0.61±0.10% and 0.59±0.22% for foils and full targets, respectively, which are in good agreement. The total reflectivity in the simulations

Table 154.V: Results for full targets, giving fill pressure (P), laser energy (E), and reflected laser energy collected by the diagnostics in ports 25 (the laser port), H17C, and 30, with simulated results underneath, and the reflection measurements made with foils for ease of comparison. The percentage in parentheses is with respect to the energy per unit area at the laser port. The calibration errors are estimated at ±7% for 25, ±16% for H17C, and ±14% for 30, as explained in the text.

P (atm)	E (J)	25 (%) Simulation	H17C (%) Simulation	30 (%) Simulation
10.9	193	65.1 mJ (0.034) 3.12 J (1.6)	0.159 mJ (0.015) 1.03 μJ (<0.001)	19.7 mJ (0.01) 25.7 μJ (<0.001)
10.8	192	53.1 mJ (0.028) 3.10 J (1.6)	0.172 mJ (0.016) 1.02 μJ (<0.001)	21.2 mJ (0.011) 25.5 μJ (<0.001)
10.9	182	45.9 mJ (0.025) 3.03 J (1.7)	96.9 mJ (0.010) 1.14 μJ (<0.001)	9.18 mJ (0.005) 44.5 μJ (<0.001)
5.2	199	118 mJ (0.059) 3.21 J (1.6)	0.177 mJ (0.016) 1.05 μJ (<0.001)	14.6 mJ (0.007) 26.4 μJ (<0.001)
8.0	191	118 mJ (0.062) 3.09 J (1.6)	0.108 mJ (0.010) 1.02 μJ (<0.001)	10.6 mJ (0.016) 25.5 μJ (<0.001)
Foil	186	85.0 mJ (0.046) 3.23 J (1.7)	0.161 mJ (0.016) 0.946 μJ (<0.001)	14.6 mJ (0.008) 27.3 μJ (<0.001)
Foil	103	51.0 mJ (0.050) 2.35 J (2.3)	0.101 mJ (0.016) 35.1 nJ (<0.001)	8.63 mJ (0.008) 1.55 μJ (<0.001)

is practically the same as the direct reflectivity, given above, because the simulations have negligible sidescatter.

The reflected intensities as a function of time measured in ports 25 and 30 are given in Fig. 154.51. The results for H17C give a similar picture to 30 but with a higher noise level. The direct reflection in all of the full target shots rises later and more sharply than for the foils and in some shots shows a slower decay. The sidescattered reflections from full targets vary in timing and last slightly longer than the sidescattered reflections from foils. These observations are consistent with the foils on the full targets curving outward, as seen in Fig. 154.38, which would lead to an initial specular reflection being spread over a greater angle and to the overdense foil initially flattening out as it is driven inward. Curvature could also explain why the direct reflected energy varied significantly but not the total reflected energy, as inferred from the Gaussian extrapolation. The variations seen in the full targets could be because of variations in the curvature, in the position of the beam relative to the center of the foil (positioning accuracy is at best ±10 μm), and in the angle of the target. Fixing the cylinders at the correct angle to the target mount was found to be an issue with the early targets, and the angle varied by ±2°; since the OMEGA Target Positioning System has no tip–tilt adjustment, we could not compensate for this issue. The angles are now carefully measured and all targets fielded are off by less than 1°.

The direct reflected spectra are given in Fig. 154.52; the sidescattered spectra are too noisy to distinguish any details. The full targets all show a greater red shift than the foils alone, indicating a greater inward acceleration. The greater acceleration of the foils on full targets could be caused by the thinning caused by the gas pressure exceeding their elastic limit, resulting in less mass to be accelerated. It is also possible that the walls of the cylinder lead to a slower radial expulsion of the foil plasma, which appears to be the only explanation for the rapid transition to total transmission seen with the foils alone. With the foil

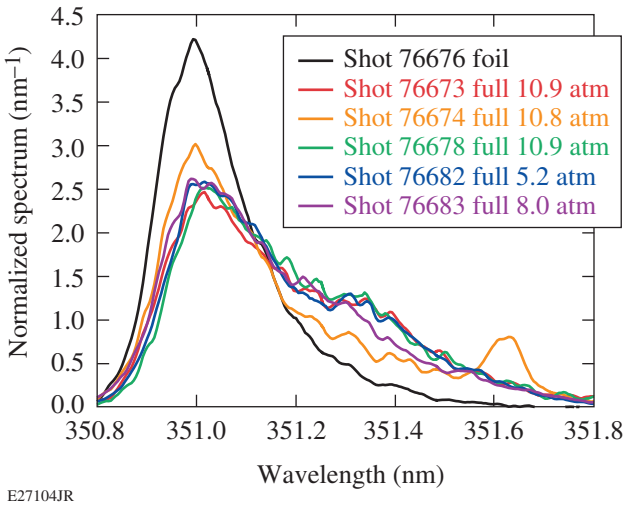

Figure 154.52
Direct reflected spectra, normalized so that the area under the curve is 1, for all shots except shot 76677 (foil, 103 J), which is very similar to that for shot 76676.

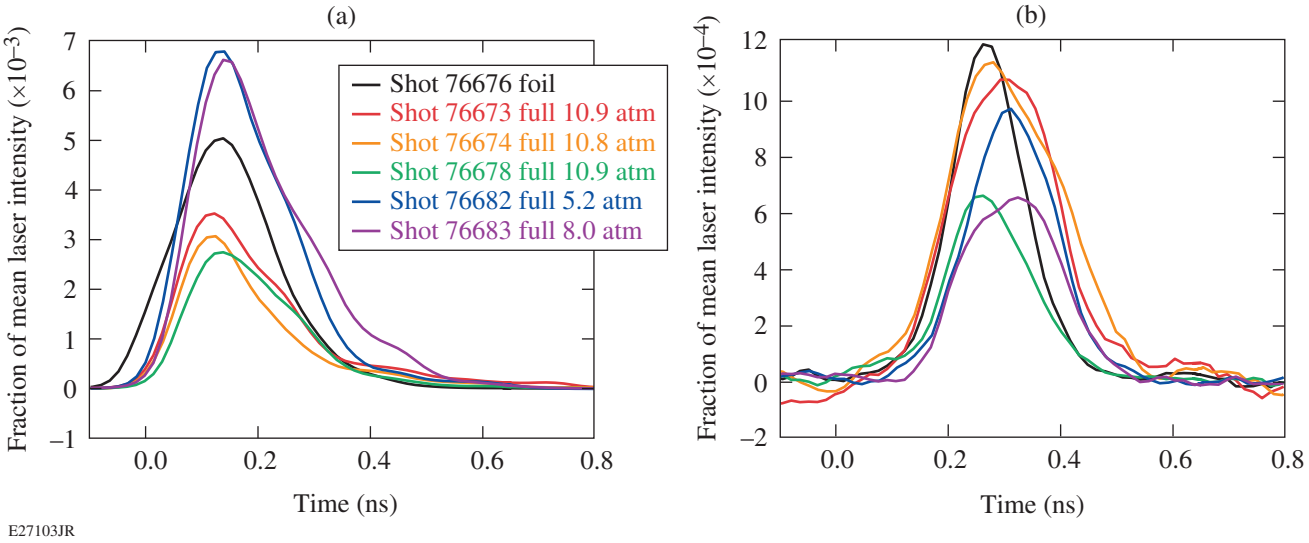

Figure 154.51
Reflected intensities in (a) 25 and (b) 30 for all shots except shot 76677 (foil, 103 J), which is very similar to that for shot 76676.

plasma remaining longer in the path of the beam, reflection will last longer and the overdense plasma could be accelerated for a longer time, which is consistent with the observations.

One unique feature was seen in the reflections from two of the full targets (shots 76673 and 76674): a brief red-shifted reflection at some time after the main signal and at different angles in each shot, shown in Fig. 154.53. This feature is responsible for the peak near 351.6 nm seen in Fig. 154.52 for shot 76674, but it cannot be seen in the reflected intensity given in Fig. 154.51 because the time axis does not extend far enough. It is possible that a similar signal coinciding with the main signal is present in other shots, contributing to the variation in the signals. We believe that this is a reflection from the back of the target, which would be determined by the bend in the fill tube, as seen in Fig. 154.38(c), which varied from shot to shot. It is also possible that the glue used to fix the cylinder and the fill tube into the target mount partially occluded the hole, causing a reflection.

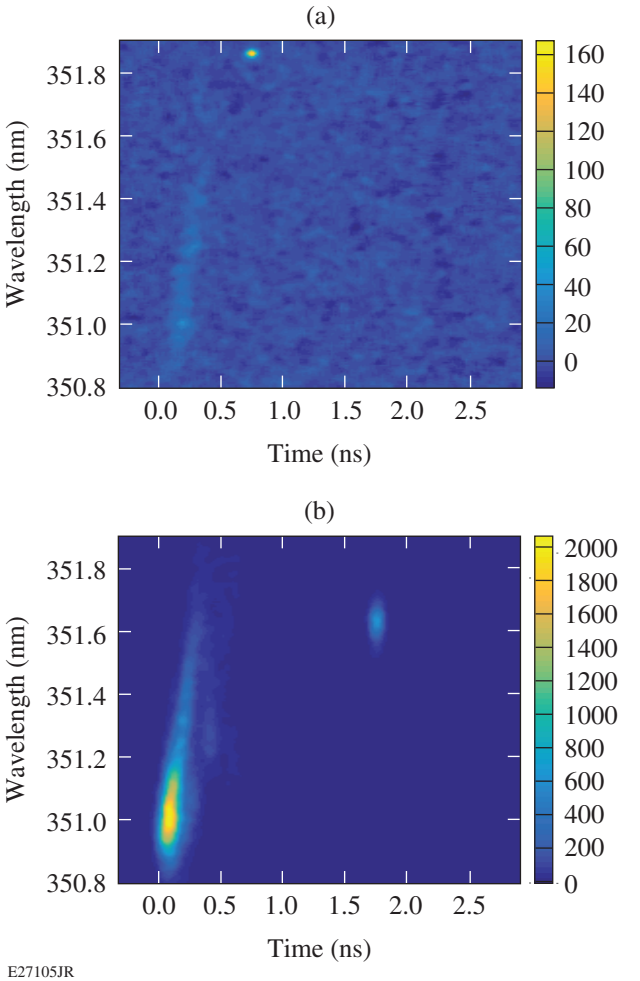

Figure 154.53
Reflection data from streaked spectrometers for shots (a) 76673 (full, 193 J) and (b) 76674 (full, 192 J) that show an additional signal at later times and longer wavelengths, not seen in other shots.

Conclusions

We have demonstrated that (1) the transmission of the 1.84-μm-thick polyimide foils selected for the preheat laser entrance windows of OMEGA MagLIF targets is sufficient for the gas to heat to >100 eV, (2) sidescatter of the transmitted light is at an acceptable level, and (3) there is no measurable SBS or SRS backscatter from the gas.

Based on the foil transmission measurements and simulations of the gas heating, for the 1.5-ns square-shaped pulses used in current OMEGA MagLIF experiments, a preheat laser energy of 100 J should be sufficient to preheat the gas to a mean temperature of 100 eV. Currently, experiments use 180 J, which according to simulations[6] is the highest energy that will not lead to significant wall blow-in before compression, and achieve a mean temperature of about 200 eV, the preheat temperature initially chosen for the point design.[6]

Simulations of the experiments using a 2-D radiation–hydrodynamic code with 3-D ray tracing and inverse bremsstrahlung energy deposition underestimated direct laser transmission, by ~10% of the laser energy, because the underdense foil plasma continued to absorb laser energy throughout the pulse, whereas the measurements show a rapid transition to total transmission. The simulations also significantly overestimated the direct reflection because this also continued throughout the pulse, significantly underestimated sidescattering of transmitted and reflected light, and significantly underestimated the red shift of transmitted and reflected light.

We believe that the disagreement between the measurements and simulations is caused by relativistic self-focusing of the laser, enhanced by self-focusing resulting from the electron density profile, followed by ponderomotive blowout of the foil plasma. The simulations do not include relativistic self-focusing or the ponderomotive force.

The minimum laser power required for relativistic self-focusing is[11]

$$P = 16.6 \frac{n_c}{n_e} \text{ GW}; \tag{4}$$

therefore, the lowest laser power used can self-focus at an electron density of 0.69 $n_c \le n_e < n_c$, and the highest laser power at

$0.21\,n_c \le n_e < n_c$. The simulations show that the electron density profile formed also acts to focus the laser, so the two mechanisms could enhance one another. The ponderomotive potential will become significant if it exceeds the electron temperature. The highest electron temperature reached in the simulations was ~1 keV, which is exceeded by the ponderomotive potential[12] at the lowest laser power used if it is focused to $R < 3.0\ \mu$m (8.5λ); at the highest laser power, this increases to 5.5 μm (16λ). The minimum value of R for which the theory of Gaussian beams is valid is $\lambda/\sqrt{2}\,\pi$, which would give a ponderomotive potential in excess of 1 MeV. It is interesting to note that a beam with sufficient power for relativistic self-focusing does have a relativistic intensity ($I\lambda^2 > 10^{18}$ W/cm^2 μm^2 or 10 GW) when focused to a spot width ~λ, and its ponderomotive force is then sufficient to separate the electrons from the ions.[13] Expulsion of electrons by the ponderomotive force provides an additional mechanism for self-focusing, prior to the expulsion of the ions, so we potentially have three synergistic focusing mechanisms. Therefore, self-focusing can occur and can lead to the ponderomotive force of the focused laser expelling the plasma radially.

Self-focusing followed by ponderomotive blowout provides a qualitative explanation for all of the observations not accounted for by the simulations. The rapid transition to total transmission can be explained by the ponderomotive force of the focused beam expelling the plasma radially until the beam path is clear. The observation of total transmission indicates that there is practically no plasma in the path of the beam, and the only way to achieve this is radial expulsion of the plasma because an expansion similar to that observed in the simulations, but at a significantly higher velocity, would require a higher absorption. The higher sidescattered transmission, seen during the transition to total transmission, can be explained by the small focal spot achieved prior to the blowout of the plasma; the circular diffraction extrapolation applied to the energy per area collected in H17C and 30 implied a time-averaged source radius of 0.8 to 1.27λ for laser energies of 60 to 190 J, which is consistent with the degree of focusing required to achieve ponderomotive blowout. The higher red shift of the transmitted light, which increased with angle, can be explained by the rapid drop in plasma density and reflection from the edges of the expanding plasma channel formed. The higher sidescattered reflection and the greater red shift of the reflected light could be explained by initial self-focusing in the blowoff plasma, before the foil becomes underdense, leading to greater curvature and acceleration of the overdense foil.

Another implication of this mechanism is that the propagation of foil into the gas will not be accurately simulated; radial expulsion of the foil should reduce the quantity of foil pushed into the gas, but the increase in laser intensity could push any remaining foil material farther inward.

Relativistic self-focusing and ponderomotive blowout can lead to the formation of N separate filaments if the laser power exceeds NP, and the spot size is large enough.[13] Given that the lowest power used appears to be capable of reaching this regime, the highest power should be able to produce three filaments. Our diagnostics cannot determine whether or not this occurred. In any case, the eventual expulsion of the plasma leads to this being only a brief phase, as seen in the transmission measurements.

The gas density used in these experiments ($0.067\,n_c$) is too low for relativistic self-focusing to occur, even at the highest laser power used. Therefore, once the laser has expelled the foil plasma, laser propagation and heating should be adequately described by the simulations, which are currently our best means of determining the gas temperature.

Experiments with a laser power less than 16 GW would provide a means of verifying that relativistic self-focusing is the mechanism responsible for the observations, but this power is too low for laser preheating in MagLIF, so it was not considered.

Currently, we do not have the capability to simulate the effect of relativistic self-focusing and the ponderomotive force in these experiments. Including the ponderomotive force in a hydrocode would lead to a complex interaction between the ray tracing and the hydrodynamics, and the code would have technical problems with holes appearing in the fluid. Furthermore, the ponderomotive force can lead to significant charge separation,[13] which would require at least a two-fluid model to be dealt with adequately. Three-dimensional PIC (particle-in-cell) code simulations, which would capture relativistic self-focusing, the ponderomotive force, and charge separation in a fully self-consistent manner, are not practical for the time and space scales of interest, particularly if collisions are to be included.

Z experiments use higher laser powers than used here, typically 0.5 TW, so relativistic self-focusing and ponderomotive blowout could also be occurring. However, the power and duration of the prepulse used can be too low for relativistic self-focusing and ponderomotive blowout to occur, and the prepulse lowers the plasma density seen by the main pulse. On the other hand, the higher power and longer wavelength (527 nm)

of the Z Beamlet laser means that relativistic self-focusing of the main pulse could occur in the gas. The typical deuterium density used in Z experiments[4] is 0.7 mg/cm^3, giving a power threshold of 0.28 TW at 527 nm.

At a wavelength of 351 nm and with pulse shaping available for the preheating beam, it would be possible to avoid relativistic self-focusing in MagLIF preheating, at all scales, if this turns out to be desirable. For the OMEGA MagLIF experiments, where the pulse shape of the preheating beam must be the same as the compression beams, it would appear to be beneficial because it increases transmission and potentially reduces the amount of foil material driven into the target. On the other hand, there is an advantage in remaining in a regime where our simulation tools are known to be valid in order to have a predictive capability.

ACKNOWLEDGMENT

The information, data, or work presented herein was funded in part by the Advanced Research Projects Agency-Energy (ARPA-E), U.S. Department of Energy, under Award Number DE-AR0000568, the Department of Energy National Nuclear Security Administration under Award Number DE-NA0001944, the University of Rochester, and the New York State Research and Development Authority. The support of the DOE does not constitute an endorsement by the DOE of the views expressed in this paper.

REFERENCES

1. S. A. Slutz, M. C. Herrmann, R. A. Vesey, A. B. Sefkow, D. B. Sinars, D. C. Rovang, K. J. Peterson, and M. E. Cuneo, Phys. Plasmas **17**, 056303 (2010).

2. A. B. Sefkow, S. A. Slutz, J. M. Koning, M. M. Marinak, K. J. Peterson, D. B. Sinars, and R. A. Vesey, Phys. Plasmas **21**, 072711 (2014).

3. M. M. Basko, A. J. Kemp, and J. Meyer-ter-Vehn, Nucl. Fusion **40**, 59 (2000).

4. M. R. Gomez, S. A. Slutz, A. B. Sefkow, D. B. Sinars, K. D. Hahn, S. B. Hansen, E. C. Harding, P. F. Knapp, P. F. Schmit, C. A. Jennings, T. J. Awe, M. Geissel, D. C. Rovang, G. A. Chandler, G. W. Cooper, M. E. Cuneo, A. J. Harvey-Thompson, M. C. Herrmann, M. H. Hess, O. Johns, D. C. Lamppa, M. R. Martin, R. D. McBride, K. J. Peterson, J. L. Porter, G. K. Robertson, G. A. Rochau, C. L. Ruiz, M. E. Savage, I. C. Smith, W. A. Stygar, and R. A. Vesey, Phys. Rev. Lett. **113**, 155003 (2014); P. F. Schmit, P. F. Knapp, S. B. Hansen, M. R. Gomez, K. D. Hahn, D. B. Sinars, K. J. Peterson, S. A. Slutz, A. B. Sefkow, T. J. Awe, E. Harding, C. A. Jennings, G. A. Chandler, G. W. Cooper, M. E. Cuneo, M. Geissel, A. J. Harvey-Thompson, M. C. Herrmann, M. H. Hess, O. Johns, D. C. Lamppa, M. R. Martin, R. D. McBride, J. L. Porter, G. K. Robertson, G. A. Rochau, D. C. Rovang, C. L. Ruiz, M. E. Savage, I. C. Smith, W. A. Stygar, and R. A. Vesey, Phys. Rev. Lett. **113**, 155004 (2014).

5. D. H. Barnak, J. R. Davies, R. Betti, M. J. Bonino, E. M. Campbell, V. Yu. Glebov, D. R. Harding, J. P. Knauer, S. P. Regan, A. B. Sefkow, A. J. Harvey-Thompson, K. J. Peterson, D. B. Sinars, S. A. Slutz, M. R. Weis, and P.-Y. Chang, Phys. Plasmas **24**, 056310 (2017).

6. J. R. Davies, D. H. Barnak, R. Betti, E. M. Campbell, P.-Y. Chang, A. B. Sefkow, K. J. Peterson, D. B. Sinars, and M. R. Weis, Phys. Plasmas **24**, 062701 (2017).

7. E. C. Hansen, D. H. Barnak, R. Betti, E. M. Campbell, P.-Y. Chang, J. R. Davies, V. Yu. Glebov, J. P. Knauer, J. Peebles, S. P. Regan, and A. B. Sefkow, Plasma Phys. Control. Fusion **60**, 054014 (20118).

8. S. P. Regan, R. Epstein, B. A. Hammel, L. J. Suter, J. Ralph, H. Scott, M. A. Barrios, D. K. Bradley, D. A. Callahan, C. Cerjan, G. W. Collins, S. N. Dixit, T. Doeppner, M. J. Edwards, D. R. Farley, S. Glenn, S. H. Glenzer, I. E. Golovkin, S. W. Haan, A. Hamza, D. G. Hicks, N. Izumi, J. D. Kilkenny, J. L. Kline, G. A. Kyrala, O. L. Landen, T. Ma, J. J. MacFarlane, R. C. Mancini, R. L. McCrory, N. B. Meezan, D. D. Meyerhofer, A. Nikroo, K. J. Peterson, T. C. Sangster, P. Springer, and R. P. J. Town, Phys. Plasmas **19**, 056307 (2012).

9. M. Geissel *et al*., Phys. Plasmas **25**, 022706 (2018).

10. A. J. Harvey-Thompson, A. B. Sefkow, T. N. Nagayama, M. S. Wei, E. M. Campbell, G. Fiksel, P.-Y. Chang, J. R. Davies, D. H. Barnak, V. Y. Glebov, P. Fitzsimmons, J. Fooks, and B. E. Blue, Phys. Plasmas **22**, 122708 (2015); A. J. Harvey-Thompson, A. B. Sefkow, M. S. Wei, T. Nagayama, E. M. Campbell, B. E. Blue, R. F. Heeter, J. M. Koning, K. J. Peterson, and A. Schmitt, Phys. Rev. E **94**, 051201 (2016).

11. P. L. Kelley, Phys. Rev. Lett. **15**, 1005 (1965); **16**, 384(E) (1966).

12. P. Mora and T. M. Antonsen, Jr., Phys. Rev. E **53**, R2068 (1996); P. Mora and T. M. Antonsen, Jr., Phys. Plasmas **4**, 217 (1997).

13. F. Cattani *et al*., Phys. Rev. E **64**, 016412 (2001); A. Kim *et al*., Phys. Rev. E **65**, 036416 (2002).

Implementation of a Wollaston Interferometry Diagnostic on OMEGA EP

Introduction

The characterization of electron density in laser-plasma experiments is an area of great interest in the field of inertial confinement fusion,[1] as well as in many other fields of high-energy-density (HED) physics.[2] Modeling and quantifying the coronal plasma density profile of a laser-ablated target can serve to account for and mitigate hydrodynamic instabilities that reduce the efficiency of laser-driven fuel compression.[3] Quantitative characterization of HED plasma densities using interferometry is well documented.[4–6] Relatively high plasma densities of the order of 10^{20} cm^{-3} or above often require diagnostics that measure the gradient of phase (through refraction angle[7]) rather than phase itself. Measuring phase directly provides results with significantly less uncertainty at lower densities (<10^{20} cm^{-3}).

The most-common configurations for interferometry are typically whole-beam interferometers such as the Michelson or Mach–Zehnder.[4,5] However, as a result of the complexity and size of the OMEGA EP Laser System and target chamber, it is not possible to split the probe beam before the laser–target interaction and recombine after. Therefore, a single split-beam configuration is required. Here, the laser–plasma interaction to be probed is situated in one half of the probe beam, while the other half is used as a reference for phase. After the interaction, an optical system interferes the two halves of the probe beam to obtain phase information. A Wollaston prism configuration was chosen for this role principally because this configuration lacks significant alignment and stability problems, and allows the user significant freedoms in experimental design.[6]

The Wollaston prism configuration and similar Nomarski configurations are a common means of single-beam interferometry,[8,9] particularly for the characterization of electron density in short-pulse, laser-driven plasmas.[5,6] The design described here is unique in that it decouples fringe spacing from the field of view (FOV), magnification, and imaging resolution. As a result, these three quantities are held constant—as determined by the diagnostic's design—while fringe spacing and the beam-splitting angle may be freely chosen by the user. This freedom is advantageous for large-scale user facilities, such as OMEGA EP, wherein robust diagnostics with as few moving parts as possible are preferred.

Background

The Wollaston interferometer functions principally by use of a birefringent crystal—in this case quartz—out of which two wedged prisms are cut at a wedge angle α, rotated by 90° with respect to each other, and cemented together, as shown in Fig. 154.54. A beam incident into this prism is decomposed into its *s* and *p* polarizations as a result of the differing refrac-

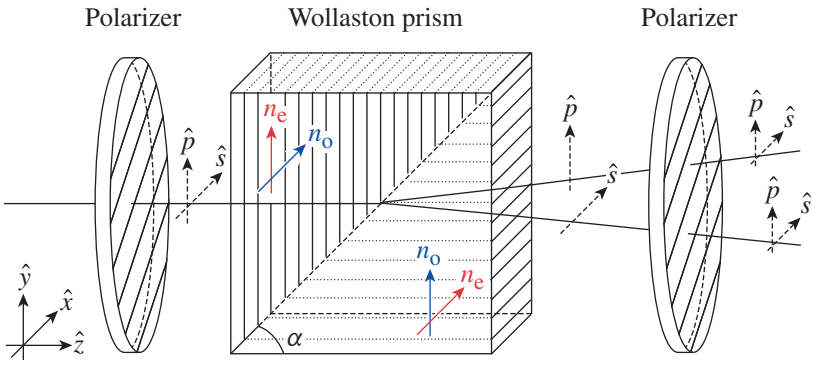

E27257JR

Figure 154.54
A schematic of the three main components in a Wollaston interferometer and their respective effects on an input beam of randomly polarized light. In the first prism, the n_o and n_e axes are oriented along the *x* and *y* directions, respectively. The opposite is true for the second prism. Both polarizers are oriented for polarization transmission along the axis 45° between *x* and *y*.

tive indices experienced by light along the x and y directions as drawn in Fig. 154.54. At the back surface of the prism, two distinct beams will emerge orthogonally polarized and angularly separated. To ensure all input beams have equal components s and p when entering the prism, a polarizer is placed before the prism at 45° with respect to the optical axis. An additional polarizer, parallel to the first, is placed after the prism to select the polarization component of each output beam again at 45°, allowing the two beams to interfere.

Figure 154.55 shows a schematic of the optical system used on OMEGA EP to implement the Wollaston interferometer. Although the presence of the first polarizer ensures that only beams with equal parts s and p will reach the prism, an input beam that is not already polarized along the 45° axis will be partially absorbed by this polarizer. To avoid this unnecessary beam attenuation, a half-wave plate (HWP) is placed directly before the first polarizer angled at

$$\theta_{\mathrm{HWP}} = \frac{\theta_{\mathrm{in}} + \theta_{\mathrm{pol}}}{2}, \tag{1}$$

where θ_{in} is the angle of the input beam's polarization and θ_{pol} is the angle of the first polarizer (all angles measured counterclockwise with respect to the x axis). Assuming the input beam is linearly polarized, a HWP oriented at this angle will rotate the input polarization to match that of the first polarizer. After rotation, any remaining ellipticity in the beam will be eliminated by the first polarizer, ensuring equal beam irradiances, resulting in high fringe contrast.

Considering now an input probe beam of appreciable width originating from infinity, a collection lens and a focusing lens may be used in conjunction to form two distinct images of the beam. The separation of these images is a function of the deviation angle between the two polarizations as they exit the prism. The deviation angle is itself a function of the birefringence of the crystal and the wedge angle of the prism. Therefore, the crystal and wedge angle may be chosen such that the two beams only partially overlap. If Region A represents the half of the beam above the optical axis and Region B represents the half below, the design parameters of the prism may be chosen such that Region A of one image overlaps onto Region B of the other, thereby creating a split-beam interferometer.

Use of this type of interferometer requires the plasma under study to be completely confined to one half (Region A or B) of the probe beam. To change the angle at which the probe beam is split, the Wollaston prism may be rotated about the z axis from 0° to 90°, allowing for flexibility in the design of the laser-plasma experiment. The two polarizers should be rotated by the same amount to provide the Wollaston with equal parts s and p and to select the output polarization of the greatest magnitude. For this reason, the two polarizers are mounted on the same rotation stage as the prism. To maintain the condition of minimal beam attenuation at the first polarizer, the HWP should be rotated accordingly [see Eq. (1)]—at half the angle of the rotation of the Wollaston—to accommodate the new angle of the polarizer.

The key attribute of this design is the ability to easily vary fringe spacing without affecting beam overlap, magnification, or imaging resolution. As can be seen in Fig. 154.55, a collimated probe beam creates two point sources that are situated just to the left of the final focus lens. These point sources interfere to provide the fringes observed in the region of image overlap at the image plane. When two point sources interfere, fringes form at discrete angles, and the fringe separation observed is inversely proportional to the spacing between the two sources. When a lens is used to focus the fringes, these discrete angles

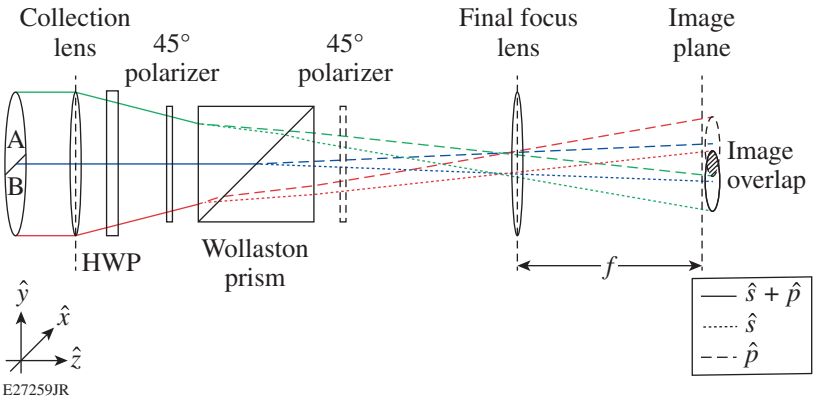

Figure 154.55
Schematic demonstrating how spatially separated Regions A and B may be overlaid and may interfere with one another. It should be noted that in this sketch the beam polarizations are drawn as if the second polarizer were inactive in order to better demonstrate how each polarization propagates through to the image plane. Each ray is colored according to the region of space from which it originates: green represents Region A, red represents Region B, and blue represents the midpoint between the two regions.

are converted to discrete positions in space. Since the angles presented to the lens do not depend on the distance between the point sources and the lens, the fringe density is independent of where the point sources fall along the z axis (referring to Fig. 154.55). Applying the small angle approximation for two-point-source interference,[10] the fringe separation s is

$$s = \frac{\lambda f}{d}, \tag{2}$$

where λ is the wavelength of the probe beam, f is the focal length of the final focus lens, and d is the distance between the two point sources. In this system, the Wollaston prism is responsible for the point-source separation. The prism imparts an angle between the gently converging rays of s- and p-polarized light, and these now deviated rays are allowed to propagate over some distance in the z direction, creating a separation between the rays in the y direction (as seen in Fig. 154.55) when they reach the focus of the collection lens. Altering the z distance over which these rays propagate—by moving the prism along the z axis—will linearly affect the separation between the sources. Knowing now that z is proportional to d, where z is the distance over which the deviated rays are allowed to propagate before reaching a focus, Eq. (2) dictates that s is *inversely proportional* to z. Therefore, fringe spacing is variable and may be changed simply by adjusting the position of the prism with respect to the final focus lens.

The final image overlap, by contrast, is purely a function of the angle of deviation between the two beams exiting the prism. As the prism imparts the same angle regardless of its position, moving the prism along the z axis alters the fringe spacing without affecting the image overlap. Magnification is also independent of the fringe spacing because it is simply the ratio of the f number of the final focus lens over that of the collection lens. Moving the prism does not change either f number and therefore does not affect magnification. Finally, it should also be noted that the fringe density is independent of resolution; this optical system is diffraction limited, so the resolution is limited only by the f number of the collection lens.

It may also be noted that this design is free of the aberrations (spherical, astigmatism, etc.) introduced in past designs[5,6,8,9] by focusing and forming an image through the prism. Looking to Fig. 154.55, an image is formed only by the final focus lens and notably not by the collection lens. For an object placed at the front focus of the collection lens, each point will convey a bundle of rays (not drawn in Fig. 154.55) that travel *collimated* through the prism, avoiding the typical aberrative effects of imaging through a thick prism.

Experimental Setup

In the OMEGA EP Laser System, the 1054-nm output of an Nd:glass laser is sent through an IR transport system and frequency quadrupled[11] to yield a 5-mm-diam 4ω probe beam expanding at $f/25$. This beam is then passed through the target chamber center (TCC), where the laser–plasma interaction takes place. The beam is collected at $f/4$, and imaged downstream using a catadioptric telescope and transport system[11] to the 4ω diagnostic table, where it encounters the system shown in Fig. 154.55 before finally reaching a charge-coupled device (CCD). Figure 154.56 demonstrates how the field of view (FOV) of this system is defined by the intersection between Regions A and B of the two overlapping images, where fringes are clearly visible. This region is approximately 1.2×1.6 mm at TCC.

The magnification of this system was measured with the alignment grid shown in Fig. 154.56 and found to be 13.5, yielding a pixel pitch at the CCD of 1 μm/pixel. At this magnification, an imaging resolution of 5 μm is attained.

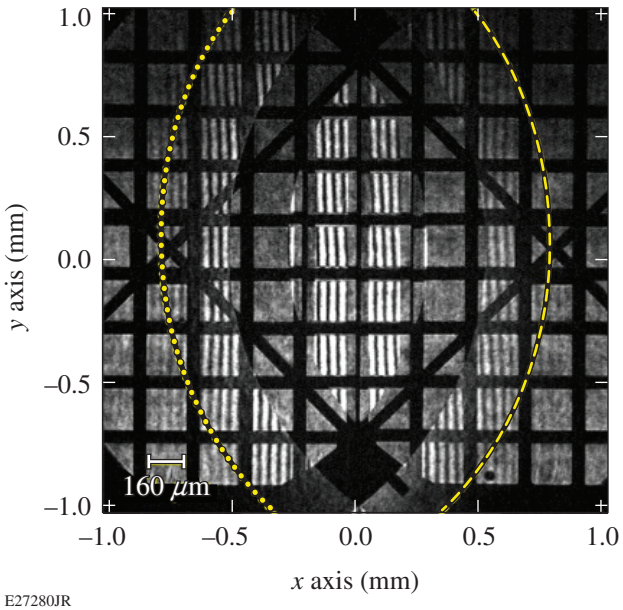

Figure 154.56
Interferogram produced by a 4ω alignment grid placed at target chamber center (TCC). The dashed and dotted yellow lines represent the edges of the two overlaid images produced by the interferometer. The features on this grid are of a known size (160×160 μm) and were used to calibrate the axes and define the field of view at TCC.

Since the fringe spacing is a function of the Wollaston prism's position, it may be altered over a definite range. This range was tested with the Wollaston prism mounted on an optical rail. Figure 154.57 shows two cases [(a) and (b)] in which the position of the Wollaston prism along the rail differs significantly to produce relatively broad (76 μm/fringe) and fine (17 μm/fringe) fringe spacings. In Fig. 154.57(c), six experimental images of differing fringe spacings were analyzed and plotted against their corresponding prism positions. From Eq. (3), it is clear that fringe spacing is inversely proportional to the z distance over which the deviated s and p beams propagate, which is consistent with an inverse trend between measurements of prism position and fringe spacing. By this relation, fringe spacing may be varied from ~17 μm/fringe to 76 μm/fringe.

Data Retrieval and Analysis

In general, the analysis of interferometry for the purpose of yielding plasma density information occurs in two steps: phase retrieval and density extraction. In the first step, the variations in fringe spacing of an interferogram are converted to repeating variations in phase. These phase variations, each occurring over an interval of $-\pi$ to π, are "unwrapped" to form a continuous map of phase. The phase from a reference interferogram, with no phase object present, is subtracted to account for any offsets or aberrations in the optical system. After retrieving phase information, a relation is made between the phase accrued when light passes through a plasma and that plasma's electron density distribution. With this relation, an axisymmetric 3-D plasma density can be recovered.

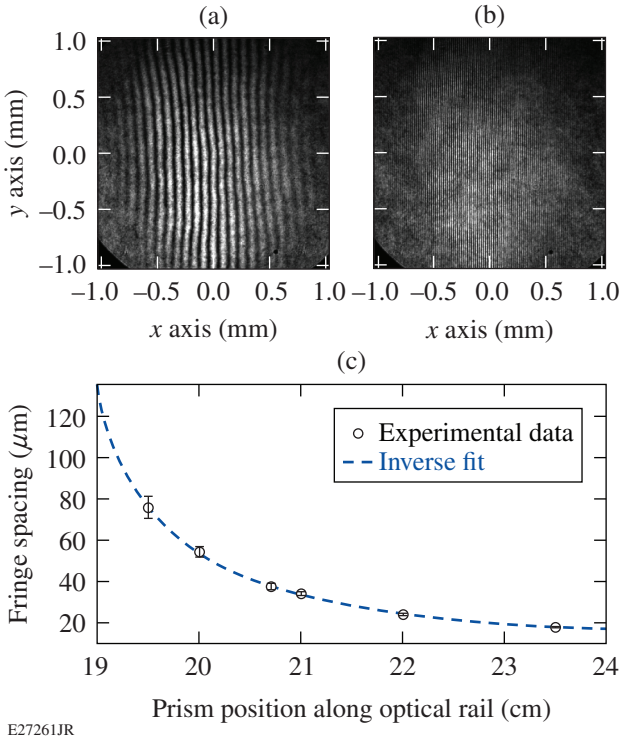

Figure 154.57
(a) Interferogram produced when the Wollaston prism is at a position of 19.5 cm along the optical rail; fringe spacing: 76±5 μm. (b) Interferogram produced when the prism is at position 23.5 cm; fringe spacing: 17.4±0.2 μm. (c) Plot of fringe spacing as a function of prism position. Data, drawn as black circles with vertical error bars, were taken from six experimental images with fringe spacings found programmatically to yield a standard deviation. The dashed trend curve, shown in blue, represents an inverse fit of the data.

To investigate experimental error, the phase variations in a reference interferogram with relatively moderate fringe spacing (34 μm/fringe) were analyzed, as displayed in Fig. 154.58. To retrieve the phase from this interferogram, a fast Fourier transform method[12] was used. A region of interest (ROI) was selected where valuable phase information could be retrieved [as seen in Fig. 154.58(a)], and a discrete 2-D Fourier transform of the interferogram was computed, producing a 2-D spatial frequency map $F(k_x,k_y)$. Because these fringes occur only in the x direction, all relevant phase information is contained in k_x and the frequency map $F(k_x,k_y)$ was summed in the y direction to yield $F(k)$. This now 1-D spatial frequency distribution $F(k)$ contains a dc term centered at $k = 0$, representing the slowly varying background features of the image, and two ac terms offset from $k = 0$ symmetrically, representing the sinusoidal variation of the fringes. One of these two ac terms was selected through spectral filtration and inverse Fourier transformed to create a new interferogram containing only the fringes and phase perturbations present in the original image [see Fig. 154.58(b)]. The 2-D phase angle of this new interferogram was calculated and unwrapped using a phase-unwrapping algorithm. Another reference interferogram with identical fringe spacing and image overlap was analyzed, and its 2-D phase subtracted from the 2-D phase yielded by the first. Figure 154.58(c) shows the resultant phase variations in the ROI.

As expected, the phase difference $\Delta\varphi$ retrieved from an interferogram with no phase object present looks like experimental noise centered around $\Delta\varphi = 0$. The standard deviation of this phase noise was found to be ±0.4 rad.

Using the geometrical optics approximation for slowly varying media,[13] the measured phase difference in the interferogram can be expressed as a function of density integrated along a chord through the plasma:

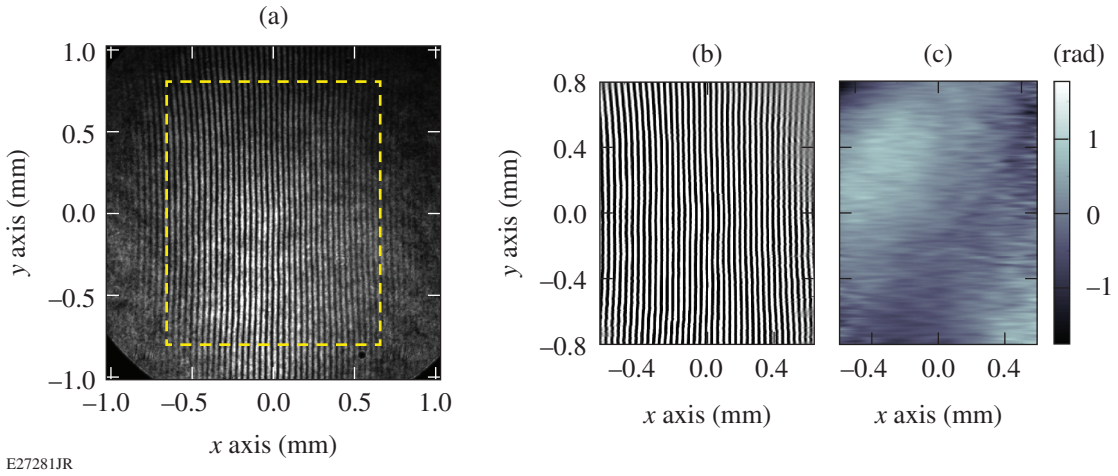

Figure 154.58
(a) The region of interest (ROI), denoted by dashed yellow lines, shown within the full interferogram as seen by the charge-coupled device. This interferogram was produced at rail position 21.0 cm, with approximate fringe spacing 34 μm/fringe. (b) The ROI, after having its dc term filtered. (c) The phase retrieved from the ROI, subtracted by the phase of another identically treated interferogram.

$$\Delta\varphi = \frac{-\pi}{\lambda n_c}\int n_e \mathrm{d}l, \tag{3}$$

where n_c is the critical plasma density for the probe beam $\left(n_c \equiv 4\pi^2 c^2 m\epsilon_0 / \lambda^2 e^2\right)$, λ is the wavelength of the probe beam, n_e is the electron (plasma) density, dl is the differential unit length through the plasma, m is the mass of an electron, and e is the electron charge. Assuming that the plasma under study is axisymmetric, Eq. (3) is Abel inverted[14] to extract the plasma density profile from the phase.

To gauge the range over which plasma density may be accurately measured using this diagnostic, a "synthetic" axisymmetric plasma density profile was used. By analyzing a phase map with a *known* density profile, it is possible to quantify the propagation of phase error through Abel inversion and to characterize an uncertainty in density. Figure 154.59(a) shows a model plasma density profile typical of coronal plasmas from a flat target.[15] The profile was integrated to yield phase by using Eq. (3). This phase was then directly Abel inverted and compared to the original density distribution to ensure agreement and confirm the validity of the method. The average percent error across the ROI caused by Abel inversion alone was found to be ~4%. The phase noise found previously [see Fig. 154.58(c)] was then added to the synthetic phase map [Fig. 154.59(b)] and Abel inverted to yield a plasma density distribution with quantifiable error resulting from noise [Fig. 154.59(c)]. The average error in density over this region was calculated to be $\pm 7 \times 10^{17}$ cm^{-3}. As can be seen in Fig. 154.59(d), the added phase noise does not significantly impact densities of the order of 10^{19} cm^{-3} and above but quickly deteriorates data where density reaches below 3×10^{18} cm^{-3}.

Conclusion

A Wollaston interferometer was built and implemented onto the 4ω diagnostic table of OMEGA EP. The interferometer uses a Wollaston prism to overlap two regions of a single probe beam, resulting in fringes in an FOV of 1.2 × 1.6 mm at TCC. The design of the diagnostic allows for unique flexibility in experimental design at large-scale fusion facilities, permitting each user to freely vary the fringe spacing (17 to 76 μm/fringe) and beam-splitting angle (0° to 90°) with no effect on FOV, magnification, or imaging resolution. Preliminary analysis has indicated that the interferometer allows the characterization of plasma density over a range of 3×10^{18} to 1×10^{20} cm^{-3} with a phase noise of approximately ±0.4 rad. Looking forward, this diagnostic will be used in conjunction with other existing diagnostics on OMEGA EP—namely angular filter refractometry (AFR)[5]—to greatly reduce experimental uncertainty in the low-density regions (~10^{19} to ~10^{20} cm^{-3}), where the data sets of both diagnostics overlap and to supplement data at densities below the current lower limit of AFR at ~10^{19} cm^{-3}.

ACKNOWLEDGMENT

This work is supported by the Department of Energy National Nuclear Security Administration under Award Number DE-NA0001944. The support of DOE does not constitute an endorsement by DOE of the views expressed in this article.

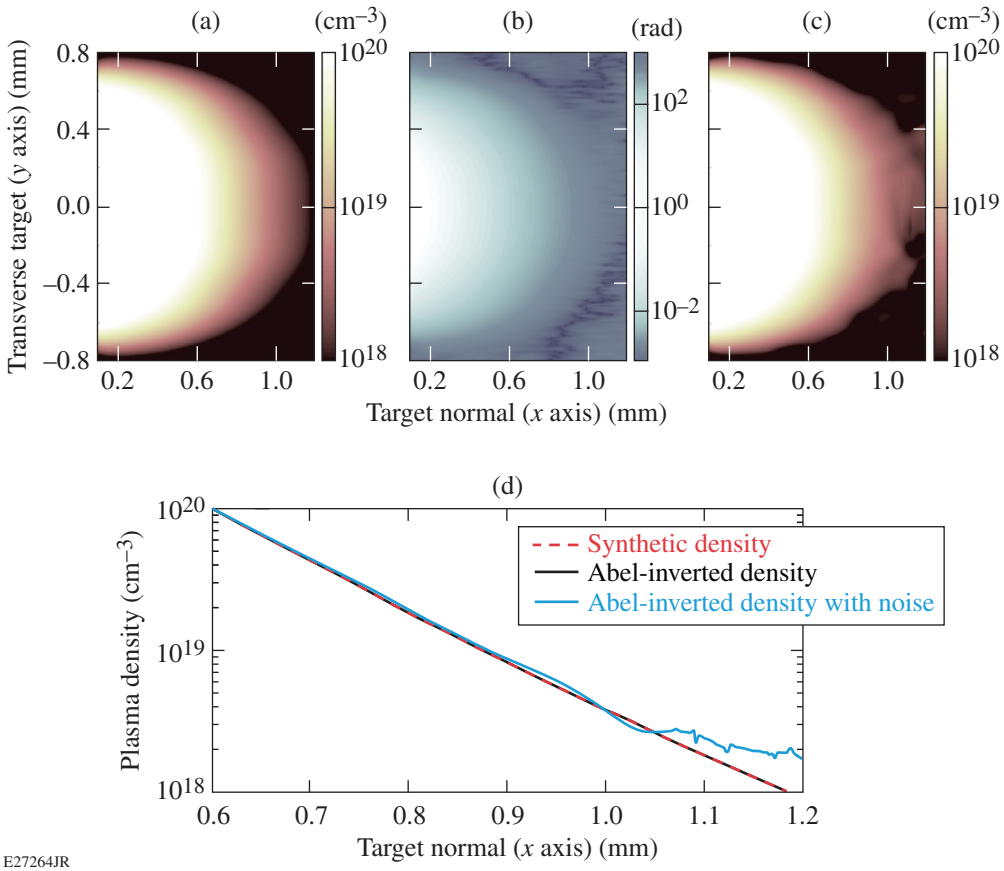

Figure 154.59

(a) An axisymmetric "synthetic" plasma density used as the phase object to be analyzed. (b) The phase yielded by integrating over the synthetic density in Fig. 154.59(a) using Eq. (3), plus the phase noise as seen in Fig. 154.58(c). (c) The density profile yielded by Abel inverting the phase in Fig. 154.59(b). (d) A series of logarithmic plasma density profiles along the target normal centered at $y = 0$ mm. The synthetic plasma density is drawn as a dashed red line, the Abel-inverted density (without noise) as a solid black line, and the Abel-inverted density with noise as a solid blue line.

REFERENCES

1. R. Betti and O. A. Hurricane, Nat. Phys. **12**, 435 (2016).
2. National Research Council (U.S.) Committee on High Energy Density Plasma Physics, *Frontiers in High Energy Density Physics: The X-Games of Contemporary Science* (The National Academies Press, Washington, DC, 2003).
3. D. T. Michel, A. V. Maximov, R. W. Short, J. A. Delettrez, D. Edgell, S. X. Hu, I. V. Igumenshchev, J. F. Myatt, A. A. Solodov, C. Stoeckl, B. Yaakobi, and D. H. Froula, Phys. Plasmas **20**, 055703 (2013).
4. I. H. Hutchinson, *Principles of Plasma Diagnostics*, 2nd ed. (Cambridge University Press, Cambridge, England, 2002), pp. 104–117.
5. S. S. Harilal and M. S. Tillack, Fusion Division, Center for Energy Research (University of California, San Diego, La Jolla, CA, 2004).
6. R. Benattar, C. Popovics, and R. Sigel, Rev. Sci. Instrum. **50**, 1583 (1979).
7. D. Haberberger, S. Ivancic, S. X. Hu, R. Boni, M. Barczys, R. S. Craxton, and D. H. Froula, Phys. Plasma **21**, 056304 (2014).
8. R. D. Small, V. A. Sernas, and R. H. Page, Appl. Opt. **11**, 858 (1972).
9. U. Kogelschatz, Appl. Opt. **13**, 1749 (1974).
10. J. Walker, D. Halliday, and R. Resnick, *Fundamentals of Physics*, 9th ed. (Wiley, Hoboken, NJ, 2011).
11. D. H. Froula, R. Boni, M. Bedzyk, R. S. Craxton, F. Ehrne, S. Ivancic, R. Jungquist, M. J. Shoup, W. Theobald, D. Weiner, N. L. Kugland, and M. C. Rushford, Rev. Sci. Instrum. **83**, 10E523 (2012).
12. M. Takeda, H. Ina, and S. Kobayashi, J. Opt. Soc. Am. **72**, 156 (1982).
13. I. H. Hutchinson, *Principles of Plasma Diagnostics*, 2nd ed. (Cambridge University Press, Cambridge, England, 2002), p. 111.
14. M. Kalal and K. A. Nugent, Appl. Opt. **27**, 1956 (1988).
15. P. Angland, D. Haberberger, S. T. Ivancic, and D. H. Froula, Rev. Sci. Instrum. **88**, 103510 (2017).

Characterization of Shaped Bragg Crystal Assemblies for Narrowband X-Ray Imaging

Introduction

The unique capabilities of a shaped crystal imaging (SCI) system using Bragg crystals are the narrow spectral width ($\lambda/\Delta\lambda > 1000$) (Ref. 1), the up-to-100-fold improvement in throughput over pinhole imaging, and potentially a high spatial resolution (<2 μm) (Refs. 2 and 3). Additionally a crystal imaging setup used in backlighting mode is insensitive to spatial nonuniformities in the backlighter intensity distribution because of its limited depth of field.[4,5] Crystal imaging has been used on both small- to medium-scale facilities[1,2,6–9] and on larger-scale facilities.[4,5,10–13] Experimental data from crystal imaging systems have been reported for a variety of spectral lines and crystal materials ranging from ~1.5 to 20 keV (Ref. 14).

The major challenges of crystal imaging are the complexity of the alignment and the achievable spatial resolution. Early experiments with SCI systems experienced significant offsets between the surface of the crystal and the diffracting crystal planes. These offsets had to be compensated for by the alignment procedure.[4] Additionally, even though early experiments showed a very high spatial resolution of ~2 μm (Ref. 2), this level of performance could only be repeated in dedicated resolution test setups,[3] and most experiments using crystal imaging as a diagnostic reported spatial resolutions of the order of 10 μm or worse.[4,5,9,13,15] Even with the use of aspherically shaped substrates to correct the astigmatism of the off-axis, some illumination at Bragg angles of up to ~6° from normal and the higher-order optical aberrations like coma did not substantially improve the observed spatial resolution.[5]

This article describes the study of the imaging performance of a selection of six different crystals using the same cut and mounted on substrates of the same radius of curvature on the Multi-Terawatt (MTW) Laser System[16] at the University of Rochester's Laboratory for Laser Energetics (LLE). Both the offset between the crystal surface and the diffraction planes and the spatial resolution were measured for six crystals from two vendors. Two of the crystals were mounted on aspherical substrates. Additionally, the extent of the reflecting region on the crystal was inferred and compared with calculations of the rocking curve and the inferred angular acceptance of the crystal, given the width of the spectral line used and the diffraction properties of the crystal.

Experimental Setup

The shaped Bragg crystals studied here are designed to reflect the x rays from the Si He_α line at ~1.865 keV (0.664 nm). The crystals are cut along the $10\underline{1}1$ plane with a $2d$ spacing of 0.6687 nm. The spherically shaped crystals are 25 mm in diameter with a 0.1-mm thickness. The crystals mounted on the aspheric substrates are the same thickness but are rectangular (25×10 mm^2), with the longer side perpendicular to the diffraction direction. All substrates had a principal radius of curvature of ~500 mm. Since the deviation of the aspheric substrate from a sphere is very small,[5] at most a few micrometers, the focal shift from the asphericity of the substrate can be neglected compared to the typical manufacturing errors, which are of the order of 0.1% on the principal radius of curvature. Three crystals on spherical substrates, acquired from ECOPULSE,[17] are labeled ECO1-3. The three remaining crystal assemblies were purchased by LLE from a different vendor (INRAD[18]) and are labeled LLE3 for the spherical substrate and LLEA1-2 for the aspherical substrates.

For the experiments, the crystal assemblies are set up so that the x rays are incident on the crystal at 83.9° from the surface, the Bragg angle for the Si He_α line. This angle corresponds to an angle of incidence of 6.1° (see Fig. 154.60).

The crystals are placed ~287 mm from the target (object), and the image is recorded on a Spectral Instruments[19] x-ray CCD (charge-coupled–device) camera placed at a distance of ~1918 mm for a magnification of ~6.7.

The CCD chip is back-thinned and has 2048×2048 pixels of 13.5×13.5-μm^2 size. With a magnification of ~6.7, this translates into a resolution limit of ~2 μm. The quantum efficiency at ~1.865 keV is very high, typically >80% (Ref. 20) because this energy is directly above the Si K edge.

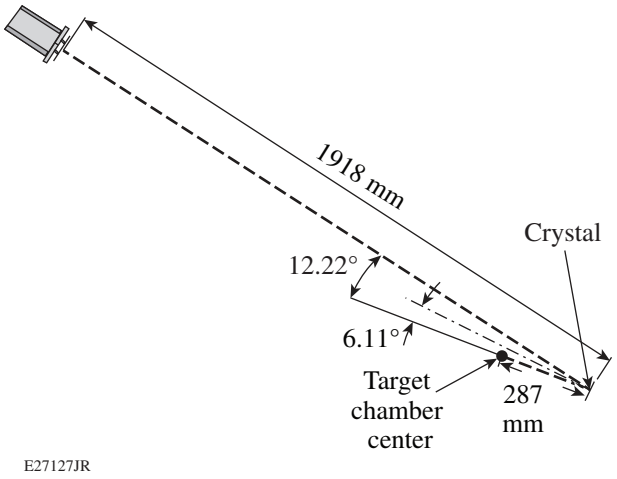

Figure 154.60
Schematic of the shaped crystal imager setup.

The primary targets, which are illuminated by the laser, are 500-μm-sq × 10-μm-thick silicon wafers. In "backlit mode" [see Fig. 154.61(a)], the laser is defocused to an ~50-μm-diam spot and a "knife-edge" absorbing target, made of a strip of ~12.5-μm-thick aluminum, is placed in the line of sight of the imager covering ~50% of the laser spot size. The absorption of this Al strip is >99.9% for the Si He_α line.[21] In "self-emission mode" [see Fig. 154.61(b)], the laser is used at best focus with a spot size of ~5-μm full width at half maximum (FWHM); this spot is directly viewed by the imager. The target is set at an angle of 45° to the incoming laser, and the imager views the target again at 45° to the target normal for a total angle of 90°. In this geometry the effects of the angle of incidence and the view angle cancel, and a round laser spot will appear round on the imager. For some experiments the angle of incidence of the laser was changed to ~3°, so that the imager views the target almost edge on to check if the size and shape of the primary x-ray spot affect the x-ray image from the SCI.

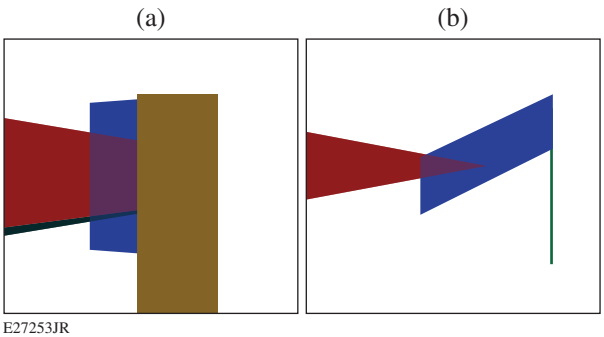

Figure 154.61
Views of the target from the crystal assembly (a) in backlit mode and (b) self-emission mode.

For these experiments the MTW laser is operated in two different modes: (1) using a pulse duration of ~10 ps at energies of up to 15 J defocused to an ~50-μm FWHM spot size for the backlit setup; (2) with a pulse duration of <1 ps, energies of up to 3 J at best focus (~5-μm FWHM) for the self-emission setup.

For the experiments with laser-produced plasmas, a 25-μm-thick CH blast shield is mounted on a 30-mm-diam frame placed ~60 μm in front of the crystal to protect it from target debris. For some experiments, additional Al foils are fixed to this frame to reduce the aperture and consequently limit the illuminated area on the crystal. Additionally, a 25-μm-thick black polyimide light shield is mounted in front of the CCD to protect it from scattered light from the high-energy laser pulse.

The crystal imager was aligned using a single-mode optical fiber illuminated by a laser at 635-nm wavelength, which was placed at the center of the target chamber, projecting a cone of light toward the crystal. The CH blast shield and the polyimide light shield were not installed for this alignment procedure.

Images of the optical focus of the tip of the single-mode fibers as recorded by the x-ray CCD are shown in Fig. 154.62 for both (a) a spherical and (b) an aspheric crystal assembly. These images are recorded after optimizing the focal-spot quality for the smallest FWHM. The significant astigmatism with the spherical crystal resulting from the 6.1° angle of incidence is clearly visible in the elongated vertical focus of ~1.8-mm length on the CCD chip. In the horizontal direction, the focus is much narrower and its FWHM corresponds to a width of ~6 μm in the object plane, when the magnification of 6.7 is taken into account. This optical resolution is of the order of the diffraction limit, which is approximately f number × λ = 7 μm, with the f number defined as the object distance (287 mm)/aperture diameter (25 mm). The aspherical crystal shows the expected improvement in the optical focus with the astigmatism almost eliminated and a round central focal-spot shape with an equivalent FWHM in the object plane of ~7 μm.

Experimental Data

1. Spatial Resolution

Figure 154.63(a) shows an x-ray image from a spherical crystal (LLE3) in the backlighter configuration. The scale of the image is identical to the image of the optical focus shown in Fig. 154.62. The horizontal width is clearly larger in the

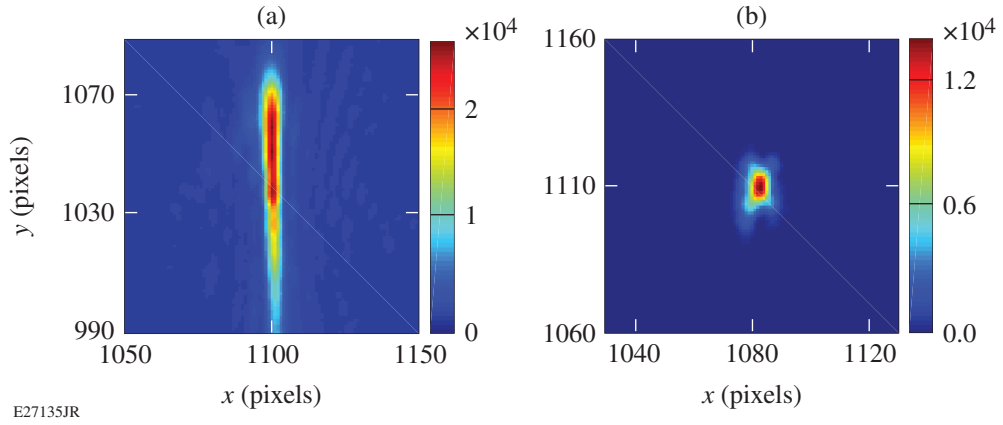

Figure 154.62
Image of the optical focus from the single-mode fiber recorded on the x-ray CCD (charge-coupled device) for (a) a spherical crystal and (b) an astigmatism-corrected asphere.

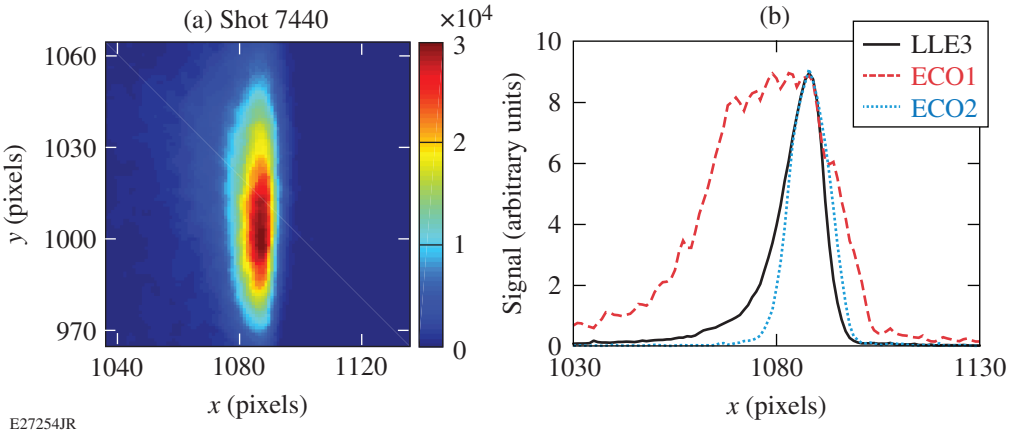

Figure 154.63
(a) X-ray image from a spherical crystal (LLE3) in the backlighting setup. The shadow of the edge is on the right side of the bright feature. (b) Horizontal lineouts through images of three different crystals. [The black solid line is the lineout through the image shown in (a).]

x-ray image compared to the optical focus. The shadow of the absorbing foil [see Fig. 154.61(a)] in front of the emitting laser-heated area is barely visible through the difference in the slope of the falloff on the left and right sides of the peak.

Figure 154.63(b) shows horizontal lineouts through x-ray images for three different crystals, averaged over 11 rows to improve the signal to noise, recorded in backlit mode [the solid black curve corresponds to a lineout of Fig. 154.63(a)]. The shadow of the knife edge can be seen more clearly in the lineouts at the right side. The width of the signal is determined mostly by the alignment tolerances and is not correlated with the resolution. The slope on the right side of the lineout is evaluated for the distance between 90% and 10% of the peak signal (90–10 distance) as a measure of the spatial resolution of the crystal. Three lineouts are taken for each image, one in the center of the astigmatic feature and one on the top and bottom, respectively. The inferred resolution does not vary significantly across the astigmatic feature, and the changes are of the order of ~1 μm. The four spherical crystals evaluated by this method show resolutions ranging from ~14 to 22 μm. Up to three images are recorded for each crystal. The analysis of these images shows variations in the measured resolution of the order of ~1 μm.

X-ray images from a spherical and an aspherical crystal in self-emission mode at a 45° angle of incidence are shown in Figs. 154.64(a) and 154.64(b), respectively. Again the astigma-

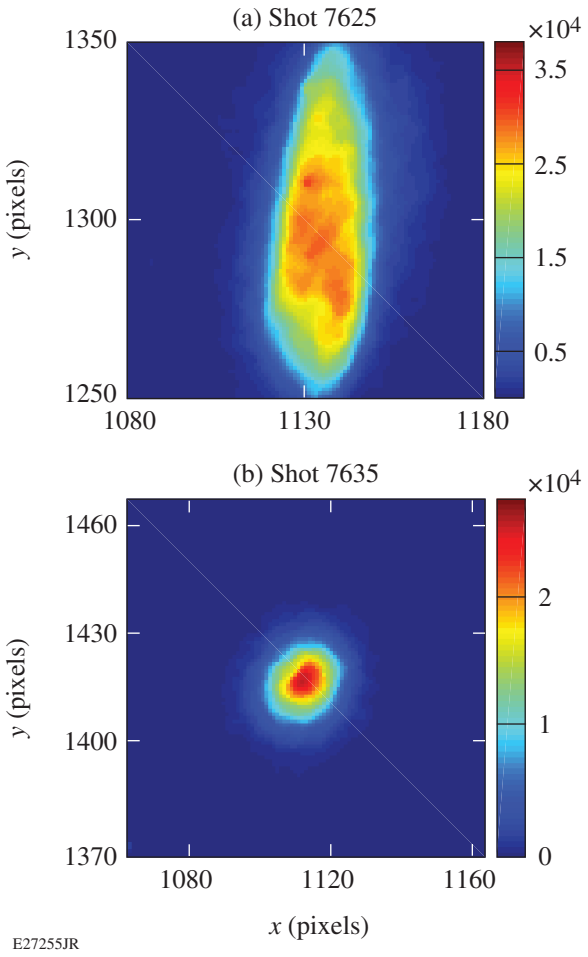

Figure 154.64
X-ray images for a spherical crystal in the self-emission setup for (a) a spherical crystal (ECO1) and (b) an astigmatism-corrected aspherical crystal (LLE-A2).

tism is clearly visible in the image from the spherical crystal and absent from the asphere. Similar to the backlit data, the resolution of the self-emission images was evaluated using the 90–10 distance on a horizontal lineout averaged over 11 rows through the image. Three spherical and two aspherical crystals were evaluated in self-emission mode with measured resolutions ranging from 11 to 44 μm. For the spherical crystals, three lineouts were taken through the astigmatic feature, with the same procedure as used in the backlit mode. Only one crystal (ECO1) showed large differences in resolution of up to ~10 μm between the lineouts taken in the center and at the edges of the crystal; all others were within ~1 μm. Since the image from the aspherical crystals is not elongated, only one lineout was taken for them.

Again, up to three images were recorded for each crystal. The variations of the measured resolution were also of the order of ~1 μm. Images from 3° angle of incidence shots (not shown here) show only a slight asymmetry, which indicates that the effects from the finite x-ray spot size are minimal. The evaluated spatial resolutions for the two crystals checked under these conditions are consistent with the 45° data within the errors.

Figure 154.65 summarizes the resolution data of the six evaluated crystals in both backlit and self-emission modes. The errors shown in the figure are the quadrature sum of the variations from the three lineouts and the shot-to-shot variations for the spherical and aspheric crystals. Within errors, the backlighting and self-emission configurations gave consistent results; nevertheless, a large spread of up to a factor of 4 in the measured spatial resolution is observed. For the ECOPULSE crystals, some of the variations in resolution were correlated with the post-polishing etch process, which differed between the three crystal assemblies, so that the effectiveness of the etching could be evaluated. The 2× difference in the resolution for the aspheric assemblies was unexpected because both assemblies were procured at the same time and were presumably prepared the same way. Unfortunately the vendor has not yet disclosed any details of their proprietary manufacturing process.

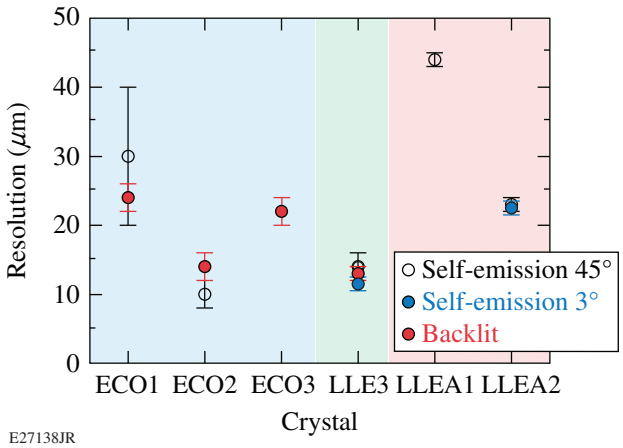

Figure 154.65
Spatial resolution measured for the six individual crystals in both backlit and self-emission geometries.

2. Angle of Surface to the Lattice Plane

Since both the alignment images and the x-ray images are recorded on the same CCD camera and the installation of the CH blast shield and polyimide light shield after the alignment does not significantly affect the alignment of the SCI system, the offset angle ω between the lattice planes and the crystal surface can be determined with high accuracy from the distance d_x between the optical spot and the x-ray spot on the CCD chip (see Fig. 154.66). In a reflecting geometry the offset angle is simply $\omega \sim d_x / (2 * d_i)$, with $d_i \sim 1918$ mm being the distance

from the crystal to the CCD. The errors on the offset angle are caused by the uncertainties in measuring the center of the optical and x-ray spots, respectively. These errors are much smaller for the aspherical crystals than the spherical because of the smaller spot sizes of the aspheres. The measured offsets are all in the diffraction direction (vertical). The horizontal (perpendicular to the diffraction direction) offsets are all well within the error bars, which supports the assumption that the alignment shifts between alignment and x-ray modes are minor and the shifts are dominated by the offset between the lattice planes and the crystal surface. Most of the measured offsets are quite small (<1 mrad); only one crystal shows an untypically large offset angle of ~1.5 mrad. This result indicates that the crystal vendors have largely solved the offset issue. With the typically observed values of <0.5 mrad, the image moves less than 1 mm per 1-m image distance, which is not an issue even on a relatively small CCD chip of 10- to 30-mm size.

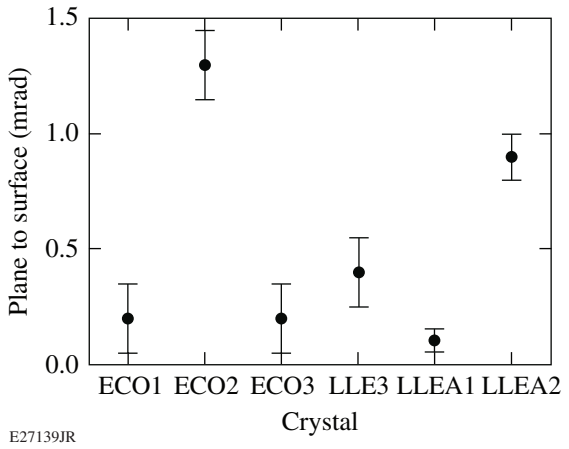

Figure 154.66
Angle of the surface to the lattice plane for the six studied crystals.

3. Illuminated Area on the Crystal

The optical and x-ray images from the spherical crystals can also be used to infer the size of the region on the crystal that actually reflects x rays from the source. A simple 1-D ray trace was set up to calculate the local angle of incidence on the crystal and to correlate the height of the astigmatic feature with the size of the illuminated area on the crystal. This ray trace showed that the 30-mm aperture in front of the crystal, where the blast shield is mounted, limits the vertical aperture to ~16 mm. Figure 154.67 shows the correlation between the distance from the center of the crystal in the vertical direction and the change in angle of incidence from the 6.1° required to fulfill the Bragg condition at the nominal x-ray energy of 1.865 keV of the Si He_α line.

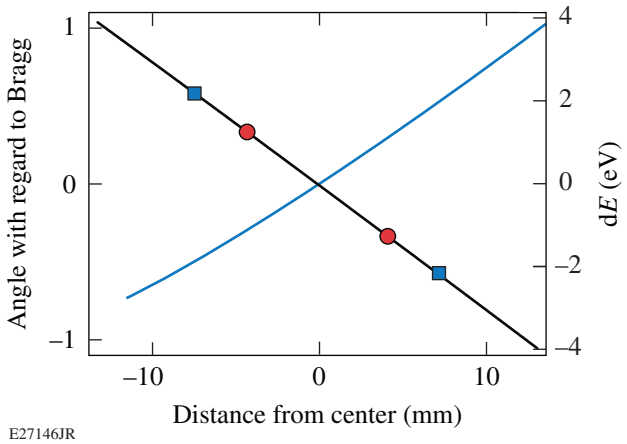

Figure 154.67
With the MTW geometry, the Bragg angle changes by ~ ±1° over the crystal surface (left axis). The height of the astigmatic focus of 1.8 mm in the optical corresponds to an illuminated height of ~14 mm on the crystal (squares). The 1-mm height of the focus in the x rays corresponds to 8 mm (circles), which translates into a spectral acceptance of ~5 eV, using the Bragg condition, which translates angle into photon energy (right axis).

The ray trace showed that the 1.8-mm measured height of the optical astigmatic feature corresponds to an ~14-mm illuminated height on the crystals, which is in reasonable agreement with the 16-mm vertical limit calculated from the geometry of the setup. The astigmatic features in the x-ray images from the spherical crystals are significantly shorter than the optical features with a length of typically 1 mm, which translates into an illuminated area of ~8 mm on the crystal. With the Bragg condition $\lambda = 2d \sin(\theta)$, the angular variation can be translated into a change in photon energy (right axis of Fig. 154.67). Using the data shown in Fig 154.67, the inferred spectral acceptance for the spherical crystals is ~5 eV. This is considerably larger than the natural line width of the Si He_α line, which is well below 1 eV, as calculated from the transition probability.[22] The actual width of the spectral line was not measured in these experiments, but data from experiments with Al targets under similar conditions[23] indicate that density, temperature, or flow effects can broaden the spectral lines to widths of the order of 5 to 10 eV.

Summary and Outlook

Six shaped crystal imaging assemblies were evaluated for their imaging quality. None of these assemblies exhibited a similarly large offset angle like the ones reported in early experiments.[4] The angular offsets were typically below 0.5 mrad, with one crystal assembly at 1.5 mrad. Both values are small enough that these images can be easily used even with small x-ray CCD detectors. The spatial resolution showed a large variation of up to 4× between the best and the worst crystals.

So far, one step in the quite-involved manufacturing procedures could be correlated with an improvement in the spatial resolution. For the ECOPULSE crystals, an additional post-polish etch of the crystal surface improves the spatial resolution twofold. This result suggests that subsurface damage from the polishing step might affect the spatial resolution, similar to the effects on the crystal rocking curve reported in the literature.[24] According to dynamic diffraction simulations (XOP[25] Stepanov x-ray server[26]), the x-ray extinction length in the crystal is of the order of 2 μm, which makes it plausible that a less-than-perfect crystal structure close to the surface can cause the spatial resolution to degrade. Additionally the height of the reflecting area on the crystal surface could be inferred from the height of the astigmatic focus for the spherical crystals. The ~8-mm measured height corresponds to a range in the Bragg angle of ~12 mrad, which is considerably larger than the rocking curve calculated by XOP of ~1 mrad. The spectral bandwidth of the reflected x rays of ~5 eV inferred from the range in Bragg angles indicates that the spectral line is significantly broadened from its natural line width. Consequently, this setup cannot be used to measure the rocking curve of the crystals.

In experiments planned for the near future, the spectrum of the x-ray source will be measured with a high-resolution spectrometer so that the linewidth can be directly compared with the inferred values from the imager. Additional experiments will explore changes in magnification and their impact on the spatial resolution.

ACKNOWLEDGMENT

The authors thank E. Baronova from ECOPULSE for the loan of two crystal assemblies.

This material is based upon work supported by the Department of Energy National Nuclear Security Administration under Award Number DE-NA0001944, the University of Rochester, and the New York State Energy Research and Development Authority.

REFERENCES

1. T. A. Pikuz *et al*., Proc. SPIE **3767**, 67 (1999).
2. Y. Aglitskiy *et al*., Appl. Opt. **37**, 5253 (1998).
3. E. O. Baronova *et al*., Instrum. Exp. Tech. **47**, 260 (2004).
4. J. A. Koch *et al*., Rev. Sci. Instrum. **74**, 2130 (2003).
5. C. Stoeckl, M. Bedzyk, G. Brent, R. Epstein, G. Fiksel, D. Guy, V. N. Goncharov, S. X. Hu, S. Ingraham, D. W. Jacobs-Perkins, R. K. Jungquist, F. J. Marshall, C. Mileham, P. M. Nilson, T. C. Sangster, M. J. Shoup III, and W. Theobald, Rev. Sci. Instrum. **85**, 11E501 (2014).
6. T. Missalla *et al*., Rev. Sci. Instrum. **70**, 1288 (1999).
7. Ch. Reich *et al*., Phys. Rev. E **68**, 056408 (2003).
8. S. Le Pape *et al*., Rev. Sci. Instrum. **79**, 106104 (2008).
9. J. A. King, K. Akli, R. A. Snavely, B. Zhang, M. H. Key, C. D. Chen, M. Chen, S. P. Hatchett, J. A. Koch, A. J. MacKinnon, P. K. Patel, T. Phillips, R. P. J. Town, R. R. Freeman, M. Borghesi, L. Romagnani, M. Zepf, T. Cowan, R. Stephens, K. L. Lancaster, C. D. Murphy, P. Norreys, and C. Stoeckl, Rev. Sci. Instrum. **76**, 076102 (2005).
10. K. Fujita *et al*., Rev. Sci. Instrum. **72**, 744 (2001).
11. C. Stoeckl, J. A. Delettrez, R. Epstein, G. Fiksel, D. Guy, M. Hohenberger, R. K. Jungquist, C. Mileham, P. M. Nilson, T. C. Sangster, M. J. Shoup III, and W. Theobald, Rev. Sci. Instrum. **83**, 10E501 (2012).
12. C. Stoeckl, G. Fiksel, D. Guy, C. Mileham, P. M. Nilson, T. C. Sangster, M. J. Shoup III, and W. Theobald, Rev. Sci. Instrum. **83**, 033107 (2012).
13. G. Hall *et al*., Bull. Am. Phys. Soc. **62**, BAPS.2017.DPP.GO7.3 (2018).
14. M. S. Schollmeier and G. P. Loisel, Rev. Sci. Instrum. **87**, 123511 (2016).
15. D. B. Sinars *et al*., Appl. Opt. **42**, 4059 (2003).
16. V. Bagnoud, in *Frontiers in Optics 2004* (Optical Society of America, Rochester, NY, 2004), Paper FMM2.
17. EcoPulse Inc., Springfield, VA 22152, http://www.ecopulse.com/ (12 April 2018).
18. Inrad Optics, Northvale, NJ 07647.
19. Spectral Instruments Inc., Tucson, AZ 85745.
20. S. Hubert and V. Prévot, Appl. Opt. **53**, 8078 (2014).
21. CXRO X-Ray Interactions with Matter, http://henke.lbl.gov/optical_constants/ (12 April 2018).
22. NIST Atomic Spectra Database, NIST Standard Reference Database #78, Ver. 5, November 2017, http://www.nist.gov/pml/data/asd.cfm (1 June 2016).
23. W. Theobald, C. Stoeckl, P. A. Jaanimagi, P. M. Nilson, M. Storm, D. D. Meyerhofer, T. C. Sangster, D. Hey, A. J. MacKinnon, H.-S. Park, P. K. Patel, R. Shephard, R. A. Snavely, M. H. Key, J. A. King, B. Zhang, R. B. Stephens, K. U. Akli, K. Highbarger, R. L. Daskalova, L. Van Woerkom, R. R. Freeman, J. S. Green, G. Gregori, K. Lancaster, and P. A. Norreys, Rev. Sci. Instrum. **80**, 083501 (2009).
24. E. J. Armstrong, Bell. Syst. Tech. J. **25**, 136 (1946).
25. M. Sánchez del Río and R. J. Dejus, Proc. SPIE **8141**, 814115 (2011).
26. GID_SL on the Web, 19 September 2016, http://x-server.gmca.aps.anl.gov/GID_sl.html (12 April 2018).

Measurements of Bulk Fluid Motion in Direct-Drive Implosions

Introduction

In inertial confinement fusion (ICF) experiments performed on OMEGA, a spherical shell of deuterium–tritium (DT) ice or CH plastic is filled with DT gas. A laser illuminates the shell, applying an ablative pressure that accelerates the shell radially inward. As the shell converges, it compresses the DT gas, converting its kinetic energy into thermal energy of the gas. This spherical compression produces a hot spot at temperatures and densities that allow fusion reactions to occur.

To achieve maximum conversion of a shell's kinetic energy to hot-spot thermal energy, a spherically symmetric implosion is desired. In reality, implosions suffer from both low-mode[1] and high-mode[2] asymmetries, which degrade implosion performance. Understanding and measuring the degradation in performance caused by real world asymmetries are vital to optimize direct-drive implosions and constrain theoretical models.

Bulk collective motion of the hot spot is characteristic of implosions with low-mode asymmetries.[3,4] Measurements of bulk collective motion in ICF experiments would confirm the existence of low-mode asymmetries and give indications of the perturbation strength. This work describes a method to measure bulk collective motion of the hot spot in ICF experiments by measuring the primary DT fusion neutron energy spectrum.

The neutron energy spectrum produced by a stationary fusing fluid element was studied non-relativistically by Brysk[5] and semi-relativistically by Ballabio.[6] The neutron energy spectrum produced by a moving fusing fluid element was studied fully relativistically by Appelbe[7,8] and Munro.[9,10] These results showed that the shape of the neutron energy spectrum is approximately Gaussian with moments that depend not only on the plasma ion temperature but also on the fluid element velocity. In particular, if the fluid element is moving with a bulk collective motion, the first moment of the neutron energy spectrum is shifted depending on the magnitude of the projection of the fluid velocity along the measurement axis.

The relationship between the fluid element velocity and the corresponding neutron energy shift has been derived non-relativistically by Murphy[11] and relativistically by Zylstra.[12] Assuming all bulk collective motion is along the line of sight (LOS) of the measurement, the relativistic relationship can be written as

$$v_f = \frac{v - v_0}{1 - v v_0}, \tag{1}$$

where v_f is the fluid element bulk flow velocity in the lab frame, v is the measured neutron velocity in the lab frame, and v_0 is the neutron velocity in the fluid element frame. The neutron velocity is related to the mass normalized neutron energy $\chi = E/m_{\mathrm{n}}$ by

$$v = \frac{\sqrt{\chi^2 + 2\chi}}{\chi + 1}. \tag{2}$$

By using Eqs. (1) and (2), shifts in the neutron energy spectrum can be interpreted as bulk collective motion of the fusing fluid element.

In ICF experiments there is not just a single fusing fluid element; instead there is a collection of fusing fluid elements within the hot spot that are distributed in space and time. Since measurements of the neutron energy spectrum are both spatially and temporally integrated, we interpret shifts in the first moment of the neutron energy spectrum as the neutron-averaged hot-spot bulk collective fluid velocity.

Simulations of cryogenic OMEGA implosions with low-mode asymmetries caused by real world effects such as laser illumination nonuniformity, target offset, and ice roughness showed neutron-averaged hot-spot bulk collective motion as large as 100 km/s along particular measurement axes.[4] Previous measurements of shifts in the first moment of the neutron

energy spectrum by nuclear recoil spectroscopy inferred bulk collective motion as large as 210±30 km/s in polar-direct-drive (PDD) experiments at the National Ignition Facility (NIF),[13] while measurements by a similar method in direct-drive experiments on OMEGA lacked the energy resolution required to measure fluid velocities relevant on OMEGA.[12]

In this article we present measurements of shifts in the first moment of the neutron energy spectrum using the neutron time-of-flight (nTOF) technique.[14] The following sections (1) describe a new nTOF detector fielded on OMEGA that measures bulk collective motion of the hot spot; (2) describe the detector calibration including measurements of the detector instrument response function (IRF) and the absolute timing calibration; (3) report measurements of bulk collective motion in cryogenic implosions; and (4) present conclusions and discuss an extension of this method to four lines of sight.

Detector Design

The neutron energy spectrum produced in OMEGA implosions is measured using a series of nTOF spectrometers.[15] Recent increases in neutron yields greater than 10^{14} on OMEGA have provided high neutron statistics for the nTOF detectors.[16]

A new nTOF detector has been built to take advantage of the increased neutron yield. By decreasing the scintillator volume, the new detector provides a fast IRF of 1.7-ns full width at half maximum (FWHM) while maintaining a large signal-to-noise ratio for neutron yields between 10^{10} to 10^{14}. A fast instrument response minimizes the distortion of the incoming primary DT neutron signal, which has a FWHM between 2 to 4 ns, by the detector IRF and therefore makes it possible to accurately measure the primary DT neutron energy spectrum.

The new detector consists of a 50-mm × 50-mm × 5-mm quenched plastic scintillator [EJ-232Q-1% (BC-422Q)] (Ref. 17), attached to a 15-cm acrylic light guide, which is coupled to a Photek 140 photomultiplier tube (PMT).[18] The PMT is operated at a constant bias of –4.7 kV to ensure a stable PMT response and sufficient gain. The PMT signal is transported to a four-channel 10-GSamples/s Tektronix oscilloscope by a 5-m LMR-400 coaxial cable. To maximize light collection efficiency, the entire scintillator and light-guide connection is covered in a light-tight wrapping. The detector design is shown in Fig. 154.68.

The detector is located in a well collimated LOS 13.0 m from target chamber center (TCC) in the southern hemisphere of the OMEGA target chamber along the P7 port. This is the only shielded LOS on OMEGA and allows for all relevant electronics, including the PMT, to be out of the LOS of the primary neutron beam while also minimizing the signal from scattered neutrons. The combination of these two features results in an extremely high-quality signal.

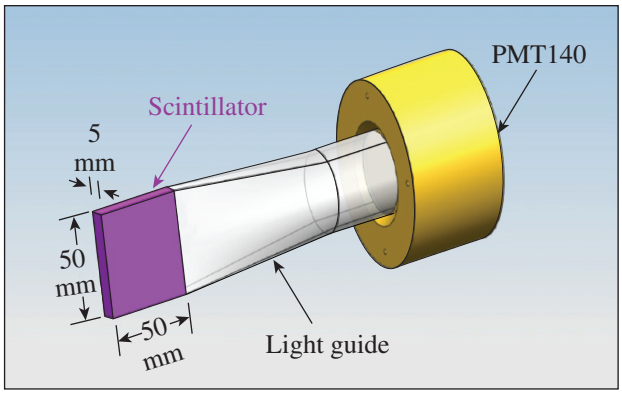

Figure 154.68
The detector design consists of a small quenched plastic scintillator (purple) connected to a light guide, which is connected to a photomultiplier tube (PMT140) (yellow).

Detector Calibration

1. Instrument Response Function

The IRF can be constructed by considering the detector's neutron and photon responses. The neutron response measures the neutron transit time through the detector, while the photon response measures the recorded electronic signal as a function of time for an impulse photon signal. The actual IRF is a convolution of these two components.[19]

Due to the thin scintillator design, the transit time of a 14-MeV neutron through the scintillator is ~100 ps. This results in the average number of neutron interactions within the scintillator being 1 and the neutron response being well approximated by a delta function in time. For this reason the IRF for this detector is simply the photon response.

The detector photon response, and therefore the detector IRF, has been measured *in situ* by recording the detector response to x-ray impulse signals created by illuminating a Au sphere or Au foil with a 20- or 100-ps-long Gaussian laser pulse. The x-ray signal produced in these experiments had a temporal width between 70 and 100 ps as measured by the neutron temporal diagnostic (NTD).[20] The x-ray signals produced in these experiments, therefore, approximate a delta function in time incident on our detector so the recorded signal is a direct measurement of the IRF.

The detector IRF was measured over a six-month period with ten x-ray calibration shots of varying x-ray intensities. The IRF was found to be extremely stable over this period with no deviations observed. An average IRF was constructed by normalizing and aligning the measured signals to their peak and is shown in Fig. 154.69 along with the ten measured signals.

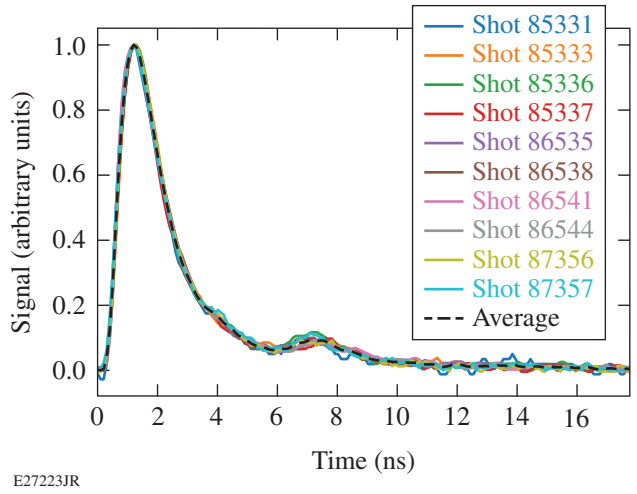

Figure 154.69
The measured x-ray signals from a series of calibration experiments along with the averaged shape. All signal peaks have been aligned in time and normalized. The FWHM of this detector instrument response function is 1.7 ns with a rise time of 0.6 ns. The bump ~5 ns after the main peak is attributed to an ion after pulse unique to the PMT140 used in the detector.

The exponentially modified Gaussian shape of the IRF is characteristic of scintillator detectors, which have a finite excitation lifetime. The average detector IRF has a measured FWHM of 1.7 ns with a rise time of 0.6 ns. The after pulse ~5 ns after the main peak is a unique feature of this detector and is attributed to an ion after pulse,[21] when the applied bias voltage is above 4.6 kV. Decreasing the bias voltage to below 4.6 kV would eliminate the ion after pulse observed but would decrease the PMT gain and the signal-to-noise ratio.

2. Absolute Timing Calibration

To measure the absolute time of flight (TOF) of a signal, the recorded time axis must be calibrated and aligned such that the origin is the moment the signal is produced at TCC. Additionally a calibration is required to eliminate any inherent delay and mistiming in the detector with respect to the OMEGA Hardware Timing System.

To properly time the recorded neutron or x-ray signal to the experiment, measurements of the laser pulse and neutron/x-ray bang times are required. Timing of the laser pulse at TCC is achieved with the p510 streak camera, which measures the laser pulse as it enters the target chamber.[22] The neutron/x-ray bang times are recorded with the NTD.[20] Each of these times is measured relative to the OMEGA timing fiducial. By injecting the same timing fiducial into the recorded neutron or x-ray signal, these measured quantities can be used to properly align the recorded signal with the experiment.

The transformation from a recorded signal time τ, which has an arbitrary timing origin, to the true TOF of the signal t, which is timed to the experiment, is given by

$$t = \tau - \left(\tau_0 + \Delta t_{\text{laser}} + \Delta t_{\text{bang}}\right) - \Delta t_{\text{cal}} - \Delta t_{\text{att}}, \qquad (3)$$

where τ_0 is the time of the measured fiducial on the recorded signal; Δt_{laser} is the delay between the start of the laser pulse (defined as 2% of the maximum laser power) and the fiducial as reported by the p510 streak camera; Δt_{bang} is the delay between the neutron/x-ray bang time and the beginning of the laser pulse as reported by the NTD; Δt_{cal} is a calibration constant accounting for any inherent delays and mistiming in our detector device; and Δt_{att} accounts for additional delays in the signal timing if a signal attenuator is used.

To determine Δt_{cal}, a particle i with a known TOF t_i is recorded and the measured TOF τ_i is determined. Asserting that the known TOF is t_i, Eq. (3) can be solved for Δt_{cal} by using the measured laser pulse and bang time. X-ray signals are ideal for timing-calibration experiments because the TOF is uniquely determined by the detector distance. The x-ray signals used to construct the IRF are used for this timing calibration.

The most accurate method to measure τ_x, the uncalibrated x-ray TOF, is a template-fitting algorithm.[23,24] This method relies on fitting a scaled and translated version of a template signal to the measured data. The main advantage of this technique is that there is no ambiguity in the starting time of the signal and all timing delays are included in the template function used for the fit.

In our application the template signal $m(t)$ is the averaged IRF shown in Fig. 154.69. The actual fitting function is given by

$$g\left(\tau; A, \tau_x\right) = A\, m\left(\tau - \tau_x\right). \qquad (4)$$

In practice, $m(t)$ is a cubic spline interpolation of the template function. Once this function is constructed, a least squares fit can be performed on a measured x-ray pulse to determine A and τ_x. An example of this fit is shown for shot 87356 in Fig. 154.70.

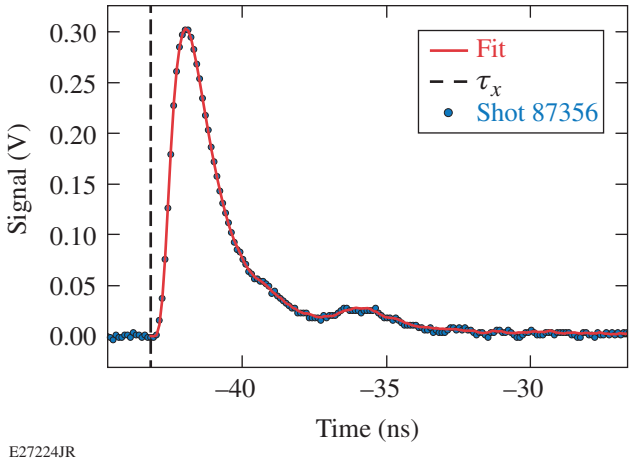

Figure 154.70
Template fit for x-ray shot 87356 to determine τ_x. The best-fit values are A = 0.303±0.001 V and τ_x = –43.162±0.002 ns. Note that the fit is preformed in the uncalibrated time axis of the oscilloscope, so the absolute value of the time holds no significance.

The template-fitting algorithm has been applied to determine τ_x and therefore Δt_{cal} for the eight x-ray calibration shots in **Instrument Response Function** (p. 120), which had a timing fiducial. Figure 154.71 shows the inferred calibration constant for each shot. The average calibration constant from these shots was determined to be Δt_{cal} = 18.840±0.067 ns.

The uncertainty in each measurement of Δt_{cal} was determined by considering the statistical and systematic uncertainties in the measurement. The systematic timing uncertainty

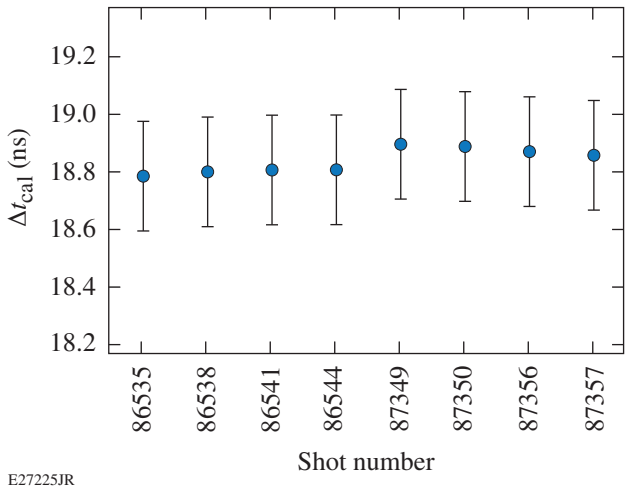

Figure 154.71
The measured calibration constant for the eight x-ray calibration shots with a timing fiducial, each with an uncertainty of ~190 ps. The average calibration constant was measured to be Δt_{cal} = 18.840±0.067 ns.

in t_x is determined by the detector volume. Assuming photon interactions are equally probable throughout the scintillator volume results in a time spread of ~183 ps. There is a statistical uncertainty associated with any fit in the recorded signal time τ, including τ_x, of ~2 ps as well as in the fiducial signal time τ_0 of ~1 ps. The total uncertainty for the terms Δt_{laser} and Δt_{bang} are ~5 ps and ~50 ps, respectively. The uncertainty in the term Δt_{att} has been measured to be ~1 ps. Adding each term in quadrature results in a total timing uncertainty of ~190 ps. The total uncertainty in the average Δt_{cal} has been reduced to ~67 ps by averaging all eight measurements.

The uncertainties in the nTOF are identical as above but include the systematic uncertainty in Δt_{cal} of ~67 ps. Adding the uncertainty of each term in Eq. (3) in quadrature, the total nTOF uncertainty is ~84 ps. This timing uncertainty corresponds to a total neutron energy uncertainty of ~10 keV and a bulk collective velocity uncertainty of ~17 km/s.

If the inferred ion temperature from the neutron energy spectrum is inflated because of nonthermal components to the second central moment associated with fluid motion,[7,11] the thermal component to the first moment[6] will also be inflated. Since the inferred ion temperature is always greater than or equal to the thermal temperature,[11] and the thermal component to the first moment is a monotonically increasing function of ion temperature,[6] a larger thermal component to the first moment is always predicted. To compensate for this, a bulk collective motion away from the detector will be inferred. This effect has been estimated with Monte Carlo calculations, and it was found that a 0.75-keV overprediction of the thermal temperature would lead to a systematic error of, at most, –6 km/s.

Measurements

The nTOF signal for a series of nominal cryogenic and room-temperature experiments has been measured, and the time axes have been calibrated using Eq. (3). To determine the moments of the neutron energy spectrum, the forward-fit method[19] was applied using the averaged IRF measured in **Instrument Response Function** (p. 120). Shifts in the mean neutron energy were then interpreted as bulk collective fluid motion with the use of Eqs. (1) and (2).

Example nTOF traces for two consecutive cryogenic targets are shown in Fig. 154.72. The large difference in the first moment of these signals corresponds to a difference in the mean neutron energy of ~68 keV and a difference in fluid velocity of ~125 km/s. The measured neutron yield and minimum measured DT ion temperature were 1.01×10^{14} and 3.9 keV for shot

86181 and 1.06×10^{14} and 4.5 keV for shot 86184, respectively. The target offset for shot 86181 was –32 μm along the OMEGA P7 direction, which can explain the observed large flow away from the detector.

Figure 154.73 shows inferred hot-spot fluid velocity for each experiment. Large variations in the inferred flow velocities are observed in cryogenic experiments but not in room-temperature implosions, indicating residual motion of the hot spot at peak neutron production may exist for cryogenic implosions. Additionally, cryogenic experiments show a systematic flow toward the detector, suggesting a systematic flow of 42 km/s along the OMEGA P7 axis while the average flow for room-temperature experiments is –6 km/s.

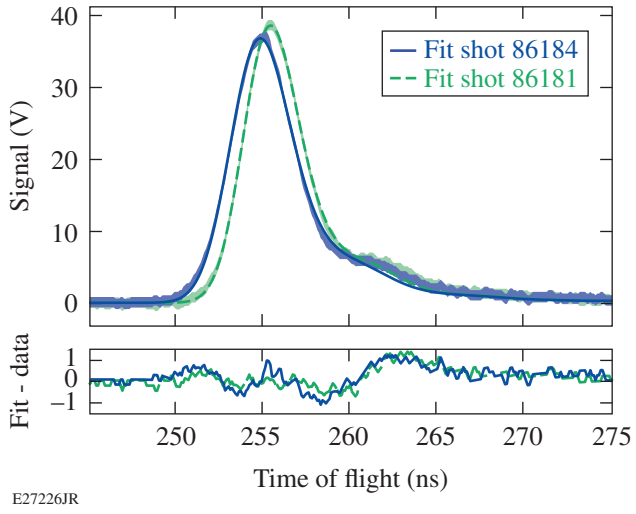

Figure 154.72
The measured nTOF signal bounded by signal noise ±1σ (blue-shaded area) with the corresponding forward fit (solid blue curve) for two consecutive cryogenic shots 86181 and 86184. The TOF shift corresponds to a difference in fluid velocity of ~125 km/s, indicating residual motion of the hot spot in each shot.

Conclusion

A new nTOF detector capable of measuring the absolute neutron energy spectrum has been fielded on the OMEGA laser. The detector IRF has been measured *in situ* and has been calibrated with x-ray timing experiments. A method has been described to infer bulk fluid velocity of the neutron-producing region in ICF experiments; measurements of this motion in cryogenic targets show velocities as large as 103±17 km/s.

Future work will extend this analysis to multiple lines of sight to determine the complete bulk fluid velocity vector. Extending this measurements to three LOS would allow for the determination of the three components of the bulk fluid velocity vector. With four measurements of the neutron mean energy, each component of the bulk collective velocity could be determined in addition to the thermal temperature, without relying on measurements of the second moment. This would eliminate the systematic uncertainty associated with the nonthermal component of the second moment discussed in **Absolute Timing Calibration** (p. 121), which leads to a decrease in the inferred flows.

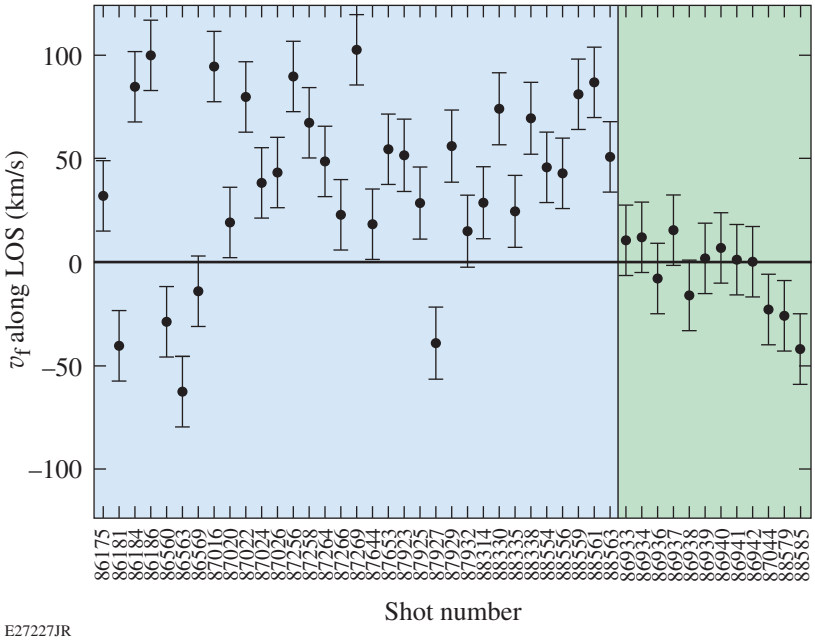

Figure 154.73
The inferred bulk collective velocity for a series of cryogenic implosions (blue-shaded area) and room-temperature implosions (green-shaded area). There are significant variations in the inferred flows in cryogenic targets, indicating residual motion of the hot spot. Additionally a systematic flow toward the P7 port is observed for cryogenic experiments.

ACKNOWLEDGEMENT

This material is based upon work supported by the Department of Energy National Nuclear Security Administration under Award Number DE-NA0001944, the University of Rochester, and the New York State Energy Research and Development Authority.

REFERENCES

1. R. C. Shah, B. M. Haines, F. J. Wysocki, J. F. Benage, J. A. Fooks, V. Glebov, P. Hakel, M. Hoppe, I. V. Igumenshchev, G. Kagan, R. C. Mancini, F. J. Marshall, D. T. Michel, T. J. Murphy, M. E. Schoff, K. Silverstein, C. Stoeckl, and B. Yaakobi, Phys. Rev. Lett. **118**, 135001 (2017).

2. P. B. Radha, T. J. B. Collins, J. A. Delettrez, Y. Elbaz, R. Epstein, V. Yu. Glebov, V. N. Goncharov, R. L. Keck, J. P. Knauer, J. A. Marozas, F. J. Marshall, R. L. McCrory, P. W. McKenty, D. D. Meyerhofer, S. P. Regan, T. C. Sangster, W. Seka, D. Shvarts, S. Skupsky, Y. Srebro, and C. Stoeckl, Phys. Plasmas **12**, 056307 (2005).

3. B. K. Spears, M. J. Edwards, S. Hatchett, J. Kilkenny, J. Knauer, A. Kritcher, J. Lindl, D. Munro, P. Patel, H. F. Robey, and R. P. J. Town, Phys. Plasmas **21**, 042702 (2014).

4. I. V. Igumenshchev, D. T. Michel, R. C. Shah, E. M. Campbell, R. Epstein, C. J. Forrest, V. Yu. Glebov, V. N. Goncharov, J. P. Knauer, F. J. Marshall, R. L. McCrory, S. P. Regan, T. C. Sangster, C. Stoeckl, A. J. Schmitt, and S. Obenschain, Phys. Plasmas **24**, 056307 (2017).

5. H. Brysk, Plasma Phys. **15**, 611 (1973).

6. L. Ballabio, J. Källne, and G. Gorini, Nucl. Fusion **38**, 1723 (1998).

7. B. Appelbe and J. Chittenden, Plasma Phys. Control. Fusion **53**, 045002 (2011).

8. B. Appelbe and J. Chittenden, High Energy Density Phys. **11**, 30 (2014).

9. D. H. Munro, Nucl. Fusion **56**, 036001 (2016).

10. D. H. Munro *et al*., Phys. Plasmas **24**, 056301 (2017).

11. T. J. Murphy, Phys. Plasmas **21**, 072701 (2014).

12. A. B. Zylstra, M. Gatu Johnson, J. A. Frenje, F. H. Séguin, H. G. Rinderknecht, M. J. Rosenberg, H. W. Sio, C. K. Li, R. D. Petrasso, M. McCluskey, D. Mastrosimone, V. Yu. Glebov, C. Forrest, C. Stoeckl, and T. C. Sangster, Rev. Sci. Instrum. **85**, 063502 (2014).

13. M. Gatu Johnson, D. T. Casey, J. A. Frenje, C.-K. Li, F. H. Séguin, R. D. Petrasso, R. Ashabranner, R. Bionta, S. LePape, M. McKernan, A. Mackinnon, J. D. Kilkenny, J. Knauer, and T. C. Sangster, Phys. Plasmas **20**, 042707 (2013).

14. R. A. Lerche *et al*., Appl. Phys. Lett. **31**, 645 (1977).

15. V. Yu. Glebov, presented at the nTOF Diagnostic Workshop at Lawrence Livermore National Laboratory, Livermore, CA, 18 July 2017.

16. V. Gopalaswamy, R. Betti,J. P. Knauer, A. Bose, N. Luciani, I. V. Igumenshchev, K. S. Anderson, K. A. Bauer, M. J. Bonino, E. M. Campbell, D. Cao, A. R. Christopherson, G. W. Collins, T. J. B. Collins, J. R. Davies, J. A. Delettrez, D. H. Edgell, R. Epstein, C. J. Forrest, D. H. Froula, V. Yu. Glebov, V. N. Goncharov, D. R. Harding, S. X. Hu, D. W. Jacobs-Perkins, R. T. Janezic, J. H. Kelly, O. M. Mannion, F. J. Marshall, D. T. Michel, S. Miller, S. F. B. Morse, D. Patel, P. B. Radha, S. P. Regan, S. Sampat, T. C. Sangster, A. B. Sefkow, W. Seka, R. C. Shah, W. T. Shmyada, A. Shvydky, C. Stoeckl, W. Theobald, K. M. Woo, J. D. Zuegel, M. Gatu Johnson, R. D. Petrasso, C. K. Li, and J. A. Frenje "Tripling the Fusion Yield in Direct-Drive Laser Fusion Through Predictive Statistical Modeling," to be submitted to Nature.

17. Eljen Technology, Sweetwater, TX 79556.

18. Photek Ltd., St. Leonards on Sea, East Sussex, TN38 9NS, United Kingdom.

19. R. Hatarik, D. B. Sayre, J. A. Caggiano, T. Phillips, M. J. Eckart, E. J. Bond, C. Cerjan, G. P. Grim, E. P. Hartouni, J. P. Knauer, J. M. Mcnaney, and D. H. Munro, J. Appl. Phys. **118**, 184502 (2015).

20. C. Stoeckl, R. Boni, F. Ehrne, C. J. Forrest, V. Yu. Glebov, J. Katz, D. J. Lonobile, J. Magoon, S. P. Regan, M. J. Shoup III, A. Sorce, C. Sorce, T. C. Sangster, and D. Weiner, Rev. Sci. Instrum. **87**, 053501 (2016).

21. N. Kishimoto *et al*., Nucl. Instrum. Methods Phys. Res. A **564**, 204 (2006).

22. W. R. Donaldson, R. Boni, R. L. Keck, and P. A. Jaanimagi, Rev. Sci. Instrum. **73**, 2606 (2002)

23. B. W. Adams *et al*., Nucl. Instrum. Methods Phys. Res. A **795**, 1 (2015).

24. W. E. Cleland and E. G. Stern, Nucl. Instrum. Methods Phys. Res. A **338**, 467 (1994).

Publications and Conference Presentations

Publications

D. H. Barnak, J. R. Davies, G. Fiksel, P.-Y. Chang, E. Zabir, and R. Betti, "Increasing the Magnetic-Field Capability of the Magneto-Inertial Fusion Electrical Discharge System Using an Inductively Coupled Coil," Rev. Sci. Instrum. **89**, 033501 (2018).

R. Boni, J. Kendrick, and C. Sorce, "An Optically Passive Method that Doubles the Rate of 2-Ghz Timing Fiducials," Proc. SPIE **10390**, 1039003 (2017).

B. P. Chock, D. R. Harding, and T. B. Jones, "Using Digital Microfluidics to Dispense, Combine, and Transport Low-Surface-Energy Fluids," Fusion Sci. Technol. **73**, 237 (2018).

A. R. Christopherson, R. Betti, A. Bose, J. Howard, K. M. Woo, E. M. Campbell, J. Sanz, and B. K. Spears, "A Comprehensive Alpha-Heating Model for Inertial Confinement Fusion," Phys. Plasmas **25**, 012703 (2018).

K. Falk, M. Holec, C. J. Fontes, C. L. Fryer, C. W. Greeff, H. M. Johns, D. S. Montgomery, D. W. Schmidt, and M. Šmíd, "Measurement of Preheat Due to Nonlocal Electron Transport in Warm, Dense Matter," Phys. Rev. Lett. **120**, 025002 (2018).

P. Fiala, Y. Li, and C. Dorrer, "Investigation of Focusing and Correcting Aberrations with Binary Amplitude and Polarization Modulation," Appl. Opt. **57**, 763 (2018).

R. K. Follett, J. G. Shaw, J. F. Myatt, J. P. Palastro, R. W. Short, and D. H. Froula, "Suppressing Two-Plasmon Decay with Laser Frequency Detuning," Phys. Rev. Lett. **120**, 135005 (2018).

S. X. Hu, "Electron-Electron Correlation in Two-Photon Double Ionization of He-Like Ions," Phys. Rev. A **97**, 013414 (2018).

K. R. P. Kafka, B. Hoffman, S. Papernov, M. A. DeMarco, C. Hall, K. L. Marshall, and S. G. Demos, "Methods for Improving the Damage Performance of Fused Silica Polished by Magnetorheological Finishing," Proc. SPIE **10447**, 1044709 (2017).

K. R. P. Kafka, S. Papernov, and S. G. Demos, "Enhanced Laser Conditioning Using Temporally Shaped Pulses," Opt. Lett. **43**, 1239 (2018).

V. V. Karasiev, J. W. Dufty, and S. B. Trickey, "Nonempirical Semilocal Free-Energy Density Functional for Matter Under Extreme Conditions," Phys. Rev. Lett. **120**, 076401 (2018).

R. K. Kirkwood, D. P. Turnbull, T. Chapman, S. C. Wilks, M. D. Rosen, R. A. London, L. A. Pickworth, W. H. Dunlop, J. D. Moody, D. J. Strozzi, P. A. Michel, L. Divol, O. L. Landen, B. J. MacGowan, B. M. Van Wonterghem, K. B. Fournier, and B. E. Blue, "Plasma-Based Beam Combiner for Very High Fluence and Energy," Nat. Phys. **14**, 80 (2018).

T. Z. Kosc, K. L. Marshall, A. A. Kozlov, S. Papernov, and S. G. Demos, "Damage Testing of Nematic Liquid Crystalline Materials for Femtosecond to Nanosecond Pulse Lengths at 1053 nm," Proc. SPIE **10447**, 104471G (2017).

J. A. Marozas, M. Hohenberger, M. J. Rosenberg, D. Turnbull, T. J. B. Collins, P. B. Radha, P. W. McKenty, J. D. Zuegel, F. J. Marshall, S. P. Regan, T. C. Sangster, W. Seka, E. M. Campbell, V. N. Goncharov, M. W. Bowers, J.-M. G. DiNicola, G. Erbert, B. J. MacGowan, L. J. Pelz, and S. T. Yang, "First Observation of Cross-Beam Energy Transfer Mitigation for Direct-Drive Inertial Confinement Fusion Implosions Using Wavelength Detuning at the National Ignition Facility," Phys. Rev. Lett. **120**, 085001 (2018).

D. T. Michel, I. V. Igumenshchev, A. K. Davis, D. H. Edgell, D. H. Froula, D. W. Jacobs-Perkins, V. N. Goncharov, S. P. Regan, A. Shvydky, and E. M. Campbell, "Subpercent-Scale Control of 3-D Low Modes of Targets Imploded in Direct-Drive Configuration on OMEGA," Phys. Rev. Lett **120**, 125001 (2018).

M. Millot, S. Hamel, J. R. Rygg, P. M. Celliers, G. W. Collins, F. Coppari, D. E. Fratanduono, R. Jeanloz, D. C. Swift, and

J. H. Eggert, "Experimental Evidence for Superionic Water Ice Using Shock Compression," Nat. Phys. **14**, 297 (2018).

J. P. Palastro, D. Turnbull, S.-W. Bahk, R. K. Follett, J. L. Shaw, D. Haberberger, J. Bromage, and D. H. Froula, "Ionization Waves of Arbitrary Velocity Driven by a Flying Focus," Phys. Rev. A **97**, 033835 (2018).

B. W. Plansinis, W. R. Donaldson, and G. P. Agrawal, "Cross-Phase-Modulation-Induced Temporal Reflection and Waveguiding of Optical Pulses," J. Opt. Soc. Am. B **35**, 436 (2018).

S. P. Regan, V. N. Goncharov, T. C. Sangster, E. M. Campbell, R. Betti, K. S. Anderson, T. Bernat, A. Bose, T. R. Boehly, M. J. Bonino, D. Cao, R. Chapman, T. J. B. Collins, R. S. Craxton, A. K. Davis, J. A. Delettrez, D. H. Edgell, R. Epstein, M. Farrell, C. J. Forrest, J. A. Frenje, D. H. Froula, M. Gatu Johnson, C. Gibson, V. Yu. Glebov, A. Greenwood, D. R. Harding, M. Hohenberger, S. X. Hu, H. Huang, J. Hund, I. V. Igumenshchev, D. W. Jacobs-Perkins, R. T. Janezic, M. Karasik, R. L. Keck, J. H. Kelly, T. J. Kessler, J. P. Knauer, T. Z. Kosc, S. J. Loucks, J. A. Marozas, F. J. Marshall, R. L. McCrory, P. W. McKenty, D. D. Meyerhofer, D. T. Michel, J. F. Myatt, S. P. Obenschain, R. D. Petrasso, N. Petta, P. B. Radha, M. J. Rosenberg, A. J. Schmitt, M. J. Schmitt, M. Schoff, W. Seka, W. T. Shmayda, M. J. Shoup III, A. Shvydky, A. A. Solodov, C. Stoeckl, W. Sweet, C. Taylor, R. Taylor, W. Theobald, J. Ulreich, M. D. Wittman, K. M. Woo, and J. D. Zuegel, "The National Direct-Drive Program: OMEGA to the National Ignition Facility," Fusion Sci. Technol. **73**, 89 (2018).

H. G. Rinderknecht, H.-S. Park, J. S. Ross, P. A. Amendt, D. P. Higginson, S. C. Wilks, D. Haberberger, J. Katz, D. H. Froula, N. M. Hoffman, G. Kagan, B. D. Keenan, and E. L. Vold, "Highly Resolved Measurements of a Developing Strong Collisional Plasma Shock," Phys. Rev. Lett. **120**, 095001 (2018).

M. J. Rosenberg, A. A. Solodov, J. F. Myatt, W. Seka, P. Michel, M. Hohenberger, R. W. Short, R. Epstein, S. P. Regan, E. M. Campbell, T. Chapman, C. Goyon, J. E. Ralph, M. A. Barrios, J. D. Moody, and J. W. Bates, "Origins and Scaling of Hot-Electron Preheat in Ignition-Scale Direct-Drive Inertial Confinement Fusion Experiments," Phys. Rev. Lett. **120**, 055001 (2018).

S. Sampat, J. H. Kelly, T. Z. Kosc, A. L. Rigatti, J. Kwiatkowski, W. R. Donaldson, M. H. Romanofsky, L. J. Waxer, R. Dean, and R. Moshier, "Power Balance on a Multibeam Laser," Proc. SPIE **10511**, 105110P (2018).

J. L. Shaw, N. Lemos, K. A. Marsh, D. H. Froula, and C. Joshi, "Experimental Signatures of Direct-Laser-Acceleration-Assisted Laser Wakefield Acceleration," Plasma Phys. Control. Fusion **60**, 044012 (2018).

D. Turnbull, S. Bucht, A. Davies, D. Haberberger, T. Kessler, J. L. Shaw, and D. H. Froula, "Raman Amplification with a Flying Focus," Phys. Rev. Lett. **120**, 024801 (2018).

M. P. Valdivia, D. Stutman, C. Stoeckl, C. Mileham, I. A. Begishev, J. Bromage, and S. P. Regan, "Talbot–Lau X-Ray Deflectometry Phase-Retrieval Methods for Electron Density Diagnostics in High-Energy Density Experiments," Appl. Opt. **57**, 138 (2018).

N. D. Viza and D. R. Harding, "Performance of Different 'Lab-on-Chip' Geometries for Making Double Emulsions to Form Polystyrene Shells," Fusion Sci. Technol. **73**, 248 (2018).

J. U. Wallace, A. Shestopalov, T. Kosc, and S. H. Chen, "Scalable Synthesis of Cholesteric Glassy Liquid Crystals," Ind. Eng. Chem. Res. **57**, 4470 (2018).

L. J. Waxer, C. Dorrer, A. Kalb, E. M. Hill, and W. Bittle, "Single-Shot Temporal Characterization of Kilojoule-Level, Picosecond Pulses on OMEGA EP," Proc. SPIE **10522**, 105221E (2018).

M. Yuly, T. Eckert, G. Hartshaw, S. J. Padalino, D. N. Polsin, M. Russ, A. T. Simone, C. R. Brune, T. N. Massey, C. E. Parker, R. Fitzgerald, T. C. Sangster, and S. P. Regan, "^{12}C(n, 2n)11C Cross Section from Threshold to 26.5 MeV," Phys. Rev. C **97**, 024613 (2018).

H. Zhang, R. Betti, V. Gopalaswamy, R. Yan, and H. Aluie, "Nonlinear Excitation of the Ablative Rayleigh–Taylor Instability for All Wave Numbers," Phys. Rev. E **97**, 011203(R) (2018).

Forthcoming Publications

S.-W. Bahk, C. Dorrer, and J. Bromage, "Chromatic Diversity: A New Approach for Characterizing Spatiotemporal Coupling of Ultrashort Pulses," to be published in Optics Express.

I. A. Begishev, J. Bromage, S. T. Yang, P. S. Datte, S. Patankar, and J. D. Zuegel, "Record Fifth-Harmonic–Generation Efficiency Producing 211-nm, Joule-Level Pulses Using Cesium Lithium Borate," to be published in Optics Letters.

A. Bose, R. Betti, D. Mangino, K. M. Woo, D. Patel, A. R. Christopherson, V. Gopalaswamy, S. P. Regan, V. N. Goncharov, C. J. Forrest, J. A. Frenje, M. Gatu Johnson, V. Yu. Glebov, J. P. Knauer, F. J. Marshall, R. Shah, C. Stoeckl, T. C. Sangster, and E. M. Campbell, "Analysis of Trends in Implosion Observables for Direct-Drive Cryogenic Implosions on OMEGA," to be published in Physics of Plasmas.

L. Ceurvorst, A. Savin, N. Ratan, M. F. Kasim, J. Sadler, P. A. Norreys, H. Habara, K. A. Tanaka, S. Zhang, M. S. Wei, S. Ivancic, D. H. Froula, and W. Theobald, "Channel Optimization of High-Intensity Laser Beams in Millimeter-Scale Plasmas," to be published in Physical Review E.

J. A. Fooks, L. C. Carlson, P. Fitzsimmons, E. Giraldez, D. N. Kaczala, M. Wei, N. Alexander, M. P. Farrell, J. Betcher, A. Harvey-Thompson, and T. Nagayama, "Evolution of Magnetized Liner Inertial Fusion (MagLIF) Targets," to be published in Fusion Science and Technology.

C. J. Forrest, J. P. Knauer, W. U. Schroeder, V. Yu. Glebov, P. B. Radha, S. P. Regan, T. C. Sangster, M. Sickles, C. Stoeckl, and J. Szczepanski, "Nuclear Science Experiments with a Bright Neutron Source from Fusion Reactions on the Omega Laser System," to be published in Nuclear Instruments and Methods in Physics Research A.

D. H. Froula, D. Turnbull, A. S. Davies, T. J. Kessler, D. Haberberger, J. P. Palastro, S.-W. Bahk, I. A. Begishev, R. Boni, S. Bucht, J. Katz, and J. L. Shaw, "Spatiotemporal Control of Laser Intensity," to be published in Nature Photonics.

M. Gatu Johnson, D. T. Casey, M. Hohenberger, A. B. Zylstra, A. Bacher, C. R. Brune, R. M. Bionta, R. S. Craxton, C. L. Ellison, M. Farrell, J. A. Frenje, W. Garbett, E. M. Garcia, G. P. Grim, E. Hartouni, R. Hatarik, H. W. Herrmann, M. Hohensee, D. M. Holunga, M. Hoppe, M. Jackson, N. Kabadi, S. F. Khan, J. D. Kilkenny, T. R. Kohut, B. Lahmann, H. P. Le, C. K. Li, L. Masse, P. W. McKenty, D. P. McNabb, A. Nikroo, T. G. Parham, C. E. Parker, R. D. Petrasso, J. Pino, B. Remington, N. G. Rice, H. G. Rinderknecht, M. J. Rosenberg, J. Sanchez, D. B. Sayre, M. E. Schoff, C. M. Shuldberg, F. H. Séguin, H. Sio, Z. B. Walters, and H. D. Whitley, "Optimization of a High-Yield, Low-Areal-Density Fusion Product Source at the National Ignition Facility with Applications in Nucleosynthesis Experiments," to be published in Physics of Plasmas.

E. C. Hansen, D. H. Barnak, R. Betti, E. M. Campbell, P.-Y. Chang, J. R. Davies, V. Yu. Glebov, J. P. Knauer, J. Peebles, S. P. Regan, and A. B. Sefkow, "Measuring Implosion Velocities in Experiments and Simulations of Laser-Driven Cylindrical Implosions on the OMEGA Laser," to be published in Plasma Physics and Controlled Fusion.

D. R. Harding, J. Ulreich, M. D. Wittman, R. Chapman, C. Taylor, R. Taylor, N. P. Redden, J. C. Lambropoulos, R. Q. Gram, M. J. Bonino, and D. W. Turner, "Requirements and Capabilities for Fielding Cryogenic DT-Containing Fill-Tube Targets for Direct-Drive Experiments on OMEGA," to be published in Fusion Science and Technology.

S. X. Hu, L. A. Collins, T. R. Boehly, Y. H. Ding, P. B. Radha, V. N. Goncharov, V. V. Karasiev, G. W. Collins, S. P. Regan, and E. M. Campbell, "A Review of *Ab Initio* Studies of Static, Transport, and Optical Properties of Polystyrene Under Extreme Conditions for Inertial Confinement Fusion Applications," to be published in Physics of Plasmas.

E. V. Ludeña, E. X. Salazar, M. H. Cornejo, D. E. Arroyo, and V. V. Karasiev, "The Liu–Parr Power Series Expansion of the Pauli Kinetic Energy Functional with the Incorporation of the Shell-Inducing Traits: Atoms," to be published in the International Journal of Quantum Chemistry.

J. A. Marozas, M. Hohenberger, M. J. Rosenberg, D. Turnbull, T. J. B. Collins, P. B. Radha, P. W. McKenty, J. D. Zuegel, F. J. Marshall, S. P. Regan, T. C. Sangster, W. Seka, E. M. Campbell, V. N. Goncharov, M. W. Bowers, J.-M. G. Di Nicola, G. Erbert, B. J. MacGowan, L. J. Pelz, J. Moody, and S. T. Yang, "Wavelength-Detuning Cross-Beam Energy Transfer Mitigation Scheme for Direct Drive: Modeling and Evidence from National Ignition Facility Implosions," to be published in Physics of Plasmas (invited).

S. A. Muller, D. N. Kaczala, H. M. Abu-Shawareb, E. L. Alfonso, L. C. Carlson, M. Mauldin, P. Fitzsimmons, D. Lamb, P. Tzeferacos, L. Chen, G. Gregori, A. Rigby, A. Bott, T. G. White, D. Froula, and J. Katz, "Evolution of the Design and Fabrication of Astrophysics Targets for Turbulent Dynamo (TDYNO) Experiments on OMEGA," to be published in Fusion Science and Technology.

S. Papernov, M. D. Brunsman, J. B. Oliver, B. N. Hoffman, A. A. Kozlov, S. G. Demos, A. Shvydky, F. Cavalcante, L. Yang, C. S. Menoni, B. Roshanzadeh, S. T. P. Boyd, L. A. Emmert, and W. Rudolph, "Optical Properties of Oxygen Vacancies in HfO_2 Thin Films Studied by Absorption and Luminescence Spectroscopy," to be published in Optics Express.

M. D. Sharpe, C. Fagan, W. T. Shmayda, and W. U. Schröder, "Partitioning of Tritium Between Surface and Bulk of 316 Stainless Steel at Room Temperature," to be published in Fusion Engineering and Design.

R. F. Smith, D. E. Fratanduono, D. G. Braun, T. S. Duffy, J. K. Wicks, P. M. Celliers, S. J. Ali, A. Fernandez-Pañella, R. G. Kraus, D. C. Swift, G. W. Collins, and J. H. Eggert, "Equation of State of Iron Under Core Conditions of Large Rocky Exoplanets," to be published in Nature Astronomy.

D. Turnbull, A. Colaïtis, R. K. Follett, J. P. Palastro, D. H. Froula, P. Michel, C. Goyon, T. Chapman, L. Divol, G. E. Kemp, D. Mariscal, S. Patankar, B. B. Pollock, J. S. Ross, E. R. Tubman, N. C. Woolsey, and J. D. Moody, "Cross-Beam Energy Transfer: Polarization Effects and Evidence of Saturation," to be published in Plasma Physics and Controlled Fusion.

P. Tzeferacos, A. Rigby, A. F. A. Bott, A. R. Bell, R. Bingham, A. Casner, F. Cattaneo, E. M. Churazov, J. Emig, F. Fiuza, C. B. Forest, J. Foster, C. Graziani, J. Katz, M. Koenig, C.-K. Li, J. Meinecke, R. Petrasso, H.-S. Park, B. A. Remington, J. S. Ross, D. Ryu, D. Ryutov, T. G. White, B. Reville, F. Miniati, A. A. Schekochihin, D. Q. Lamb, D. H. Froula, and G. Gregori, "Laboratory Evidence of Dynamo Amplification of Magnetic Fields in a Turbulent Plasma," to be published in Nature Communications.

F. Weilacher, P. B. Radha, and C. J. Forrest, "Three-Dimensional Modeling of the Neutron Spectrum to Infer Plasma Conditions in Cryogenic Inertial Confinement Fusion Implosions," to be published in Physics of Plasmas.

M. D. Wittman, M. J. Bonino, D. H. Edgell, C. Fella, D. R. Harding, and J. Sanchez, "Effect of Tritium-Induced Damage on Plastic Targets from High-Density DT Permeation," to be published in Fusion Science and Technology.

K. M. Woo, R. Betti, D. Shvarts, A. Bose, D. Patel, R. Yan, P.-Y. Chang, O. M. Mannion, R. Epstein, J. A. Delettrez, M. Charissis, K. S. Anderson, P. B. Radha, A. Shvydky, I. V. Igumenshchev, V. Gopalaswamy, A. R. Christopherson, J. Sanz, and H. Aluie, "Effects of Residual Kinetic Energy on Yield Degradation and Ion Temperature Asymmetries in Inertial Confinement Fusion Implosions," to be published in Physics of Plasmas.

Conference Presentations

C. Z. R. Huang, R. W. Wood, and S. G. Demos, "Microscopy with Ultraviolet Surface Excitation (MUSE) for Enhancing K–12 and Undergraduate Education in Life Sciences," presented at SPIE Photonics West, San Francisco, CA, 27 January–1 February 2018.

The following presentations were made at LASE, San Francisco, CA, 27 January–1 February 2018:

S. Sampat, J. H. Kelly, T. Z. Kosc, A. L. Rigatti, J. Kwiatkowski, W. R. Donaldson, M. H. Romanofsky, L. J. Waxer, R. Dean, and R. Moshier, "Power Balance on a Multibeam Laser."

L. J. Waxer, C. Dorrer, A. Kalb, E. M. Hill, and W. Bittle, "Single-Shot Temporal Characterization of a Kilojoule-Level, Picosecond Pulses on OMEGA EP."

M. J. Rosenberg, A. A. Solodov, W. Seka, R. K. Follett, S. P. Regan, A. V. Maximov, T. J. B. Collins, V. N. Goncharov, R. Epstein, R. W. Short, D. Turnbull, D. H. Froula, P. B. Radha, J. F. Myatt, P. Michel, M. Hohenberger, G. Swadling, J. S. Ross, T. Chapman, L. Masse, C. Goyon, J. E. Ralph, J. D. Moody, J. W. Bates, and A. J. Schmitt, "Planar Laser-Plasma Interaction Experiments at the Direct-Drive Ignition-Relevant Scale Lengths at the National Ignition Facility," presented at the NIF User Group Meeting, Livermore, CA, 5–7 February 2018.

The following presentations were made at the 14th Direct-Drive and Fast-Ignition Workshop, York, United Kingdom, 20–22 March 2018:

I. V. Igumenshchev, "Three-Dimensional Simulations of Direct-Drive Implosions on OMEGA."

R. C. Shah, D. Cao, S. P. Regan, R. Epstein, C. Sorce, W. Theobald, B. Kraus, K. Hill, L. Gao, B. Stratton, P. Efthimion, H. Sio, N. Kabadi, J. A. Frenje, D. Thorn, B. Bachmann, C. Jarrot, P. K. Patel, M. B. Schneider, and J. D. Kilkenny, "Hot-Spot Electron Temperature Inferred from X-Ray Continuum Emission."

J. P. Palastro, D. Turnbull, S.-W. Bahk, R. K. Follett, J. L. Shaw, D. Haberberger, A. Davies, J. Viera, N. Vafaei-Najafabadi, J. Bromage, and D. H. Froula, "Spatiotemporal Control of Laser Intensity for Plasma-Based Applications," presented at the 2018 U.S.-Japan Workshop on Theory and Simulations of High-Field and High Energy Density Physics, Hiroshima, Japan, 27–28 March 2018.


1850
MELIORA
UNIVERSITY of
ROCHESTER